

**The Design of Robust Multi-rate Repetitive Learning  
Controllers with Applications to Practical Systems**

**A Thesis  
Presented to  
The Academic Faculty**

**by  
Courtney D. James**

**In Partial Fulfillment  
of the Requirements for the Degree  
Doctor of Philosophy in Mechanical Engineering**

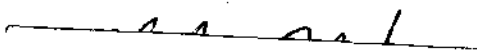
**The Georgia Institute of Technology  
November 1997**

**The Design of Robust Multi-rate Repetitive Learning  
Controllers with Applications to Practical Systems**

by

**Courtney D. James**

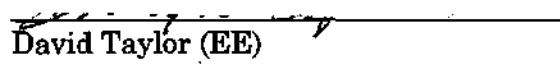
Approved:

  
\_\_\_\_\_  
Nader Sadegh, Chairman (ME)

\_\_\_\_\_  
Stephen Dickerson (ME)

  
\_\_\_\_\_  
Steven Liang (ME)

  
\_\_\_\_\_  
Christopher Atkeson (CoC)

  
\_\_\_\_\_  
David Taylor (EE)

Date Approved: 11-17-97

## DEDICATION

To Dr. Sybil M. James-Lassiter, my beloved mother and friend, for raising and guiding me in the most meaningful of ways . . . by example.

. . . and to my father Vincent and sisters Yasmine and Pat.

## ACKNOWLEDGMENT

This thesis and the associated research were made possible by the generous support of the GEM Fellowship Consortium, Xerox Corporation, and The Georgia Institute of Technology's School of Mechanical Engineering.

## TABLE OF CONTENTS

LIST OF TABLES .....	vi
LIST OF FIGURES .....	vii
SUMMARY .....	xv
CHAPTER I .....	1
INTRODUCTION	
Motivation .....	1
Repetitive Control Fundamentals .....	2
Repetitive Controller Architecture .....	4
Filtered Repetitive Controller .....	8
The Repetitive Learning Cycle, NL .....	11
CHAPTER II .....	12
PERFORMANCE AND STABILITY ISSUES	
General Stability Criteria .....	12
Periodic Disturbances and Tasks .....	15
Non-Harmonic Disturbances .....	16
Finite Attenuation of Periodic Perturbations .....	20
Introduction .....	20
Modeling Periodic System Disturbances .....	20
Classical Disturbance Model .....	21
Modified Disturbance Model .....	22
Cycle Length (NL) Uncertainty and Mismatch .....	28
Potentially Large NL Values .....	31
Robustness to Noise and Unmodeled Dynamics .....	33
CHAPTER III .....	35
ALTERNATIVE RLC FORMULATIONS	
Introduction .....	35
Internal Model Repetitive Control .....	36
External Model Repetitive Control .....	39
Parallel Repetitive Controllers .....	45

Hybrid Repetitive Controllers .....	49
CHAPTER IV.....	51
MULTI-RATE REPETITIVE LEARNING CONTROL	
Introduction.....	51
Down-Sampling .....	53
Up-Sampling.....	54
Equivalent Closed-Loop System Transformation .....	55
Up Sampling Only .....	57
Up and Down Sampling .....	59
Multi-Rate RLC Stability.....	64
CHAPTER V .....	67
EXPERIMENTAL APPARATUS	
Objective .....	67
Design Realization .....	69
Mechanical Subsystems .....	69
Electrical Subsystems .....	74
System Characterization .....	76
Open-Loop Transfer Function.....	76
Disturbance Identification .....	79
CHAPTER VI.....	83
CONTROLLER DESIGN	
Simulation Model.....	83
Closed-Loop Polynomial Control .....	83
Polynomial plus Integral Control .....	87
Q-Filter Design.....	89
Repetitive Controller.....	91
Internal Model RLC .....	93
Single Controller.....	93
Dual Controller.....	95
External Model RLC.....	96
Single Controller.....	96
Dual Controller.....	96
Hybrid RLC .....	96
CHAPTER VII .....	99
RESULTS	
Simulation Results.....	100

Comments..... 110  
Empirical Results..... 111  
Comments..... 119

CHAPTER VIII..... 120  
CONCLUSIONS AND RECOMMENDATIONS

APPENDIX A..... 123  
TEST FIXTURE COMPONENTS

APPENDIX B..... 125  
PERIODIC SIGNAL GENERATION LEMMA

REFERENCES ..... 128

**LIST OF TABLES**

Table 1 - Two empirically derived system models for the open-loop zero-pole-gain transfer function of the test fixture.....	76
Table 2 - Anticipated test fixture disturbance sources.....	79
Table 3 - Summary of test fixture components.....	124

## LIST OF FIGURES

Figure 1 - Relationship between a generic steady-state periodic output and its corresponding discrete-time periodic input. Note that $N_L$ (the cycle length or learning period) is the number of discrete steps in one learning cycle.....	3
Figure 2 - Block-diagram representation of an open-loop plant stabilized with feedforward and feedback compensation to form a closed loop system / plant, $H(z)$ .....	4
Figure 3 - “Plug-in” repetitive learning controller augmenting a closed-loop plant, $H(z)$ . .....	5
Figure 4 - Diagram of a “Bypass” repetitive learning controller augmenting the closed loop system, $H(z)$ . Disturbances are shown entering at the plant output.....	5
Figure 5 - Learning controller block diagram. $K_L$ , $Q^*(z)$ , and $R^*(z)$ represent the learning gain, “realizable” Q-filter, and the companion repetitive controller, respectively.....	6
Figure 6 - Block diagrams showing the general form of repetitive controller, $R^*(z)$ and its equivalent transfer function. Note that the $z^{-s}$ term cancels the delay term in $Q^*(z)$ and the linear phase FIR filter $W(z)$ is for robustness improvement. Setting $W(z)$ to unity removes it and yields the “pure delay” form of RLC.....	7
Figure 7 - Frequency response of a 2 <sup>nd</sup> order Least Squares FIR low-pass filter. The cutoff frequency (-3dB) is at 300 radians per second and the sample time = 5msec. Note the zero phase shift characteristic all the way to the stop band (~480rad/s). .....	9
Figure 8 - Two magnitude vs. frequency plots for the transfer functions of an internal model repetitive controller with and without a least-squares FIR filter. Note the decrease in the high frequency attenuation ability of the filtered controller .....	10
Figure 9 - Bypass repetitive learning control configuration with learning gain $K_L$ , Q-filter $Q(z)$ , repetitive controller $R(z)$ , closed loop system $H(z)$ and disturbances $d_i$ . .....	13

- Figure 10 - Complex plane envelopes for the regions in which a system with the open-loop transfer function  $K_L QH(z)$  is stable in the presence of RLC. The boundaries are based on the stability condition in equation ( 6 ) and are plotted for several values of learning gain,  $K_L$ . No value of  $K_L$  will provide stability if the phase shift of  $QH(z)$  is greater than  $\pm 90^\circ$ . ..... 14
- Figure 11 - Complex plane envelopes for  $K_L = 1.0$ . Shown are the regions inside of which (i)  $QH(z)$  is stable (solid line) and (ii)  $A_d(\omega)$  - the amplification factor for non-harmonic disturbances - is less than some threshold (shaded region). Notice that there is no region in which stability and noise attenuation ( $A_d(\omega) \leq 1$ ) coexist. However, when the amplification threshold is raised to  $A_d(\omega) \leq 1.5$ , the shaded envelop expands and enters the "stable region". ..... 19
- Figure 12 - Bypass repetitive control configuration with plant  $G(z)$ , disturbance  $d(k)$ , feedback error  $e(k)$ , [perturbed] output velocity  $\omega(k)$ , and desired velocity  $\omega_d(k)$ . ..... 23
- Figure 13 - The effect of learning cycle (NL) mismatch on the RLC error attenuation for three different controller sample times ( $T_s$ ). ..... 29
- Figure 14 - Illustration of how 3 distinct sinusoidal signals in the discrete-time domain combine to form a composite signal whose periodic frequency is the "fictitious" fundamental of the three components. .... 32
- Figure 15 - Frequency response magnitude plots for an internal model RLC (12.56 rad/s fundamental frequency) and an equivalent external model RLC with selective frequency bands. For illustrative purposes, only the 1<sup>st</sup>, 2<sup>nd</sup>, 4<sup>th</sup>, 6<sup>th</sup>, 11<sup>th</sup>, 12<sup>th</sup>, & 20<sup>th</sup> harmonic frequencies were activated. .... 36
- Figure 16 - Equivalent T/F representation of a RLC block diagram with a g-step shift. .... 37
- Figure 17 - Schematic illustration of how a single repetitive controller with an prohibitively large learning cycle ( $NL=1099$ ) can be equivalently represented by two (or more) parallel controllers with smaller learning cycles. The learning cycle of each controller is shown, along with its fundamental frequency.  $K_1 + K_2 \leq K_L$ . .... 47
- Figure 18 - Three frequency response magnitude plots for RLC #1, RLC #2, and both controllers in parallel, respectively. The parallel

- configuration has infinite loop gains at the harmonics of both individual controllers..... 48
- Figure 19 - Four views of a signal: (a)continuous, (b) sampled at high-rate with zero order hold (ZOH), (c) sampled at low-rate with ZOH, and (d) sampled at a low-rate with ZOH but reconstructed with linear interpolation (i.e., first order hold). The ratio between the high and low sampling rates as shown is  $m=4$ . The indices for the high and low rates are 'n' and 'K', respectively. .... 52
- Figure 20 - ZOH Down-Sampling: a signal sampled at one rate is resampled at a slower rate. Here, the faster rate is  $m=4$  times greater than the slower. Therefore,  $m-1=3$  points of data are lost at every K-th sampling instant..... 53
- Figure 21 - Linear weighted average curve for the intermediate down-sampling points. The appropriate weight value is applied to the 'm' future and 'm' past fast-rate sample points, as well as the current slow-rate sampling point, K. The  $(2m+1)$  weighted points are summed and the result becomes the 'filtered' signal value at time instant K..... 54
- Figure 22 - FOH Up-Sampling: a signal sampled at one rate is resampled at a higher rate. Linear (FOH) interpolation is used to approximate the missing intermediate data points, rather than a ZOH. The interpolated curve clearly produces a better representation of the original continuous curve than the ZOH curve. Here, the faster rate is  $m=4$  times greater than the slower. Therefore,  $m-1=3$  points of data must be created between slow-rate sampling instants..... 55
- Figure 23 - Illustration of a high-rate system with input  $u(n)$ , output  $y(n)$ , and discrete index 'n' being transformed to an equivalent slow-rate system with index K. The effects of any down-sampling and up-sampling are accounted for in the transformation process. .... 56
- Figure 24 - Linear interpolation of the signal  $u$  at intermediate-sampling instant  $n=mK+i$ ..... 57
- Figure 25 - Linear weighted average curve for the intermediate down-sampling points..... 59
- Figure 26- Two block diagrams of a repetitive control system. In the first diagram (multi-rate case), the plant  $H(z)$  samples at  $T_s$  samples/sec, while the Q-filter and controller,  $R(z)$ , sample at

<p><math>T_c = m \times T_s</math>. The repetitive controller is shown preceded and followed by a weighted average down-sampler and a FOH up-sampler, respectively, as described in the beginning of the chapter. Each of these add 1 delay to the system, which is compensated for by increasing <math>g</math> by 2. In the second diagram, the use of the transformed plant, <math>\tilde{H}(z)</math>, causes the entire system to reduce to a single-rate system. ....</p>	65
Figure 27- Schematic of a generic 4-roller xerographic photo-receptor module .....	68
Figure 28 - Diagram of the research test fixture with all four major sub-system shown. ....	70
Figure 29 - Detailed illustration of subsystems 1 and 2. Note that the front bracket for the cam shaft is omitted for clarity. Also, the tension spring for the cam's pivot-plank is not shown. ....	71
Figure 30 - Detailed illustration of subsystems 3 and 4. Three of the vertical bracket for the output shaft assembly are omitted to show the shaft couplings. ....	72
Figure 31 - Torque profile of a cam assembly as a function of rotation angle. The twin curves are due to the cam's dual lobes. Note the small positive torque offset; this is the torque required to overcome coulomb friction during the cam's dead zones. ....	73
Figure 32 - Signal flow diagram of the test fixture and electrical interfaces. The components within the dashed boundary constitute the open-loop plant, $G(z)$ . Voltage to the plant is a low current signal from the DAQ which is amplified and sent to the motor. The two outputs shown are the logical angular position and a voltage proportional to the instantaneous output shaft velocity. All control and analyses were performed in software on a Pentium computer running Windows NT. ....	75
Figure 33 - Experimental frequency response (Bode) plot using a swept sine routine with a 0.3volt perturbation amplitude and a 3.6volt DC carrier voltage. This allowed the output of the fixture to oscillate about the desired steady-state velocity. ....	77
Figure 34 - Open-loop frequency response of two linear plant models. Both were derived from curve fits of the data from empirical frequency response tests performed on the test fixture. The lower order model (solid) has 3 poles and no zeros, while the higher order model (dashed) has 5 poles and 2 zeros. ....	78

Figure 35 - Steady state time history and power spectral density for the open-loop system. Ten averages and a Hanning window were used in computing the FFT. Ref=2rps.....	82
Figure 36 - Power spectrum of the open-loop plant's steady-state output velocity .....	84
Figure 37 - Alternate arrangement of feedforward and feedback compensators.....	84
Figure 38 - Stable Z-Plane root location plots for the discrete open-loop plant and the discrete closed-loop compensated plant. Note that there are three unstable zeros at -20, +5, and +10 <sup>11</sup> for the closed loop system and one unstable zero at -20 for the open system, which are not visible. The closed-loop plot shows 2 pole-zero "near" cancellations and the relocation of the two poles corresponding to the 28Hz mode. This conjugate pair was moved to a region of increased damping. ....	85
Figure 39 - Frequency response of the digital feedforward plant compensator (Ts = 2.5msec), from 1 rad/s up to the Nyquist frequency (1257rad/s).....	86
Figure 40 - Frequency response plot of the open loop (dashed) and compensated closed loop system, H(z) (solid). Note that the resonance at 28Hz (176rad/s) is attenuated and the system gain is improved overall. No attempt was made to alter the mode at 534 rad/s, because it was not present in the low order model.....	87
Figure 41 - Frequency response of the digital feedforward plant compensator (Ts = 2.5msec), from 1 rad/s up to the Nyquist frequency (1257rad/s).....	88
Figure 42 - Learning controller block diagram. K <sub>L</sub> , Q*(z), and R*(z) represent the learning gain, "realizable" Q-filter, and the companion repetitive controller, respectively. ....	90
Figure 43 - Frequency response plots for the closed-loop plant H(z) (dashed) and the non-causal digital Q-filter (solid), from 1Hz up to the filter's Nyquist frequency (628rad/s). Convolution of the plant and Q-filter results in a system with virtually zero phase shift and low pass characteristics (dash-dot). ....	91
Figure 44 - Steady state time history and power spectral density for the system under closed-loop polynomial control.....	94

- Figure 45 - Hybrid repetitive learning controller composed of one (1) internal model controller and two (2) adaptive external model controllers..... 98
- Figure 46 - Schematic illustration of the output disturbance generator and the injection point of the resulting perturbations..... 100
- Figure 47 - The two disturbance generator models: (a) strictly time dependent and (b) angular position dependent. Seven individual harmonics of the fundamental were assumed: 1x, 2x, 4x, 6x, 10x, 16x, & 20x. Values for the combined disturbance gain  $K_d$  ranged from zero (no disturbances) to  $0.3/7=0.04$  rev/s..... 101
- Figure 48 - Step response curves: open-loop and closed-loop polynomial control. Note that the polynomial appears to amplify the amplitudes of the high-frequency perturbations, while attenuating the low frequency. There appears to be a low frequency oscillatory drift in both cases. Integral action eliminated this. .... 102
- Figure 49 - Transient response, polynomial compensation: Internal and external model RLC assuming periodic disturbances that are strictly functions of time. The high (realistic) disturbance amplitudes were used. Both repetitive controllers worked well. Since the internal model assumes that the disturbances are functions of time, it converges somewhat faster than the external model controller..... 103
- Figure 50 - Transient response, polynomial compensation, unrealistically low disturbance amplitudes (20% of realistic values): Internal and external model RLC assuming periodic disturbances that are functions of angular position. This test serves to verify the presence of a disturbance threshold below which repetitive control is guaranteed to work well. For these low amplitude, state-dependent disturbances, both controller forms converged quickly and completely. However, this did not remain true when the disturbance gain was increased to a more realistic value, as evident in the next diagram..... 104
- Figure 51 - Transient response, polynomial compensation, realistic disturbance amplitudes: Internal and external model RLC assuming periodic disturbances that are functions of angular position. Clearly, the threshold for asymptotic stability has been crossed in the case of the internal model controller. There is both a low-frequency oscillation and a pulsation in output velocity. The external model controller, however, is more robust and effectively attenuates the errors. .... 105

- Figure 52 - Step response curves: open-loop and closed-loop polynomial w/ PID. The integral action is apparent by the improved steady-state tracking. There is also an improvement in the AC error amplitude over polynomial control alone. .... 106
- Figure 53 - Transient response, realistic disturbance amplitudes: Internal and external model RLC assuming periodic disturbances that are strictly functions of time. As in the case of polynomial control alone, both controller forms do a good job of attenuating the errors. .... 107
- Figure 54 - Transient response, PCIA compensation, unrealistically low disturbance amplitudes (20% of realistic values): Internal and external model RLC assuming periodic disturbances that are functions of angular position. .... 108
- Figure 55 - Transient response, PCIA compensation, realistic disturbance amplitudes: Internal and external model RLC assuming periodic disturbances that are functions of angular position. The internal model controller fails to converge, as in the case of polynomial control without integral action. However, integrator does reduce the low frequency oscillations. .... 109
- Figure 56 - Steady state time history and power spectral density for the open-loop system. Ten averages and a Hanning window were used in computing the FFT. Ref=2rps. The 0.5sec overall period is visually apparent in the time trace. .... 111
- Figure 57 - Steady state time history and power spectral density for the system under closed-loop polynomial control. There is a noticeable reduction in the amount of perturbation compared to the open-loop case. .... 112
- Figure 58 - Banded spectral density comparison: Polynomial Control versus Open Loop. Note that polynomial control provides (by design) a significant amount of attenuation in the region surrounding the open-loop's 28 Hz resonance, while adding a relatively small amount of amplification at the lower frequencies. The performance of the polynomial controller would be greatly improved (especially in the lower frequencies) if integral action were present. However, as mentioned previously, integral action was only implemented in simulation. .... 113
- Figure 59 - Banded spectral density comparison: Polynomial Control versus Internal Model RLC. The repetitive controller provides superior attenuation at virtually all harmonic frequencies, with notable

<p>exceptions at 24 and 40 Hz. In fact, the attenuation improvement at the first and second harmonics (i.e., 2 and 4 Hz) is better than a factor of ten. This is due to both the repetitive control action and the mild integral action inherent in RLC. ....</p>	114
Figure 60 - Repetitive controller frequency spectrum comparison. ....	115
<p>Figure 61 - Banded spectral density comparison: <u>Internal and External Model RLC versus Hybrid RLC</u>. The hybrid repetitive controller provides superior overall disturbance attenuation compared to both the internal and external model controllers. At some shaft harmonics (e.g., 4 &amp; 20 Hz), the improvement in attenuation is on the order of 90%. The external model controllers were set to attenuate modes at 2, 4, 8, 12, 18, 20, 32, &amp; 40 Hz. ....</p>	116
<p>Figure 62 - 4-second steady-state response of the open loop system, the closed loop system with polynomial feedback, and the closed loop system with hybrid (i.e., internal and external model) repetitive learning control, respectively. ....</p>	117
<p>Figure 63 - Step response of closed loop system with hybrid (i.e., internal and external model) repetitive learning control. Learning gain is 0.2. RLC was activated 0.5 seconds after startup.....</p>	118

## SUMMARY

Presently, the convergence and asymptotic stability of a single repetitive controller can be readily assessed for a linear closed-loop system in the absence of noise and transients and subject to periodic disturbances that are strictly time dependent. This research extends the current convergence and performance criteria to include more practical cases such as: (a) systems whose periodic disturbance are a function of some state, instead of time; (b) systems in which more than one controller is used in parallel; (c) systems in which the [digital] repetitive controller must sample at a slower rate than the plant (i.e., multi-rate RLC); and (d) systems where non-harmonic errors are also present. Tests were performed both in simulation and empirically on a custom designed test fixture to verify the predicted results.

If the system's periodic disturbances are strict functions of time, RLC is shown to drive the tracking error to zero, regardless of the disturbance amplitude. However, it is proven both theoretically and experimentally that, if the disturbances depend instead on a state of the system (e.g., angular shaft position), then an upper bound exists on the amplitude of the disturbances, above which, convergence of RLC is no longer assured. In addition, two somewhat novel repetitive controller formulations were developed: (1) a hybrid repetitive controller and (2) an adaptive external model repetitive controller (A-EMRC).

# CHAPTER I

## INTRODUCTION

### Motivation

In today's increasingly competitive global marketplace, manufacturers must press the performance capabilities of their products and processes further and further in order to gain and maintain the all-important competitive edge. As a result, the demand for ultra-precise control capabilities is greater than ever. The uncertainties and disturbances inherent in virtually all systems is a major hurdle to the idealized goal of "perfect" output regulation and/ or trajectory tracking. Friction, stiction, structural compliance, backlash, rotating imbalance, etc..., are only a few examples of such obstacles.

Familiar control techniques such as Proportional-plus-Derivative (PD) and Proportional-plus-Integral-plus-Derivative (PID) are often employed, with varying success, to eliminate errors. When unaided, however, these and other common techniques are often unable to provide the zero (or near zero) tracking required by many of today's precision systems. Such requirements are usually met only after: (a) incorporating high-tolerance (and cost) components into the design to minimize the disturbances and uncertainty; (b) adding integrators to the control loop and accepting the resulting reduction in controller bandwidth and performance; and/ or (c) adding an appropriate feedforward input to the plant. The latter approach is of primary interest to this research effort.

## Repetitive Control Fundamentals

Many applications which require precise tracking control have one thing in common: the desired trajectory and the significant disturbances are periodic in nature. Examples include robotic control, process control, and velocity regulation for rotating machinery. The cyclic nature of these systems allows the implementation of a technique known as repetitive learning control (RLC). Fundamental to this controller is the notion that any periodic signal with a known period can be generated by a free dynamical system that has a positive feedback around a pure time delay. This idea, combined with the Internal Model Principle<sup>1</sup> has been the basis of repetitive control theory (3). A repetitive controller exploits the cyclic nature of a system by using the error signal from previous periods to correct and refine the current feedforward plant input. This procedure can be shown to drive the tracking error to zero for a stable plant in the absence of transients and noise [e.g., see (12)].

In order to understand the basic concept of repetitive learning control, recall that for a stable dynamic system, any desired and attainable steady-state (SS) output has at least one corresponding SS input. If the desired output is periodic, then so too is the corresponding input. Figure 1 illustrates this relationship. Furthermore, authors such as (22) have proved that, for an exponentially stable plant, if an attainable desired output is periodic with period  $T$ , then, subject to minor constraints, there exists a unique input that is also periodic in time  $T$ . RLC uses this fact to first form a periodic input that is one learning period long (i.e., one cycle length) and then fine tune this input over each subsequent period. This refinement

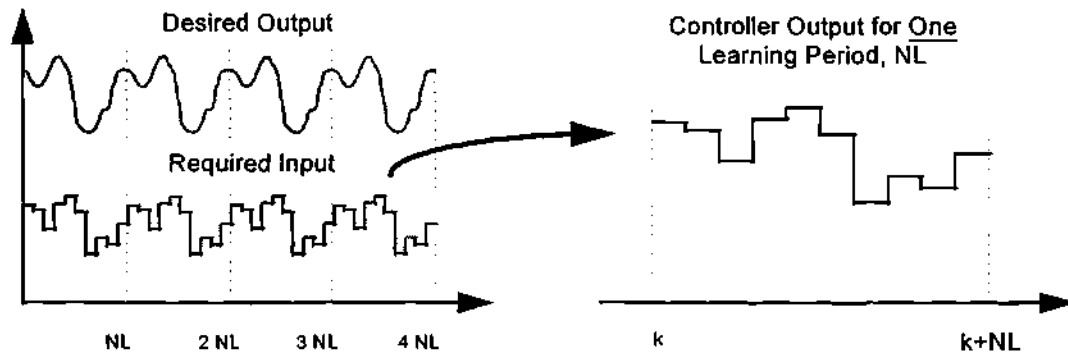


Figure 1 - Relationship between a generic steady-state periodic output and its corresponding discrete-time periodic input. Note that  $NL$  (the cycle length or learning period) is the number of discrete steps in one learning cycle.

process is akin to a human adjusting the individual bands of a graphic equalizer on an audio system to obtain the desired sound. For the case of continuous control systems, one single-period input is composed of an appropriate combination of basis functions. With digital control systems, sampling divides the single-period input into multiple segments, each of which is adjusted over time to drive the tracking error to ideally zero. All designs and analyses in this thesis were conducted in the digital domain unless otherwise noted.

It is important to realize that a learning controller is more of a supplemental control system than a stand-alone controller. Although the “raw” plant itself need not be stable, the system on which the learning controller operates must be exponentially stable, provide some degree of disturbance rejection across a broad band, and have reasonably acceptable dynamic response characteristics. This can be achieved by augmenting the raw plant with some form of feedforward and/ or feed-

---

<sup>1</sup> Francis and Wonham, 1975

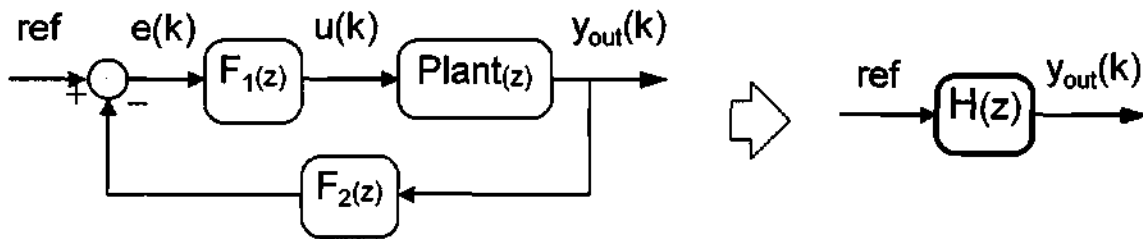


Figure 2 - Block-diagram representation of an open-loop plant stabilized with feedforward and feedback compensation to form a closed loop system / plant,  $H(z)$ .

back compensation; e.g., PD, PID, polynomial, etc... The block diagrams in Figure 2 illustrate this arrangement; the closed-loop plant,  $H(z)$ , is assumed to be exponentially stable, proper, and rational. Thus the term “system” will be taken to mean the stabilized closed-loop plant  $H(z)$  unless otherwise noted.

### Repetitive Controller Architecture

Repetitive controllers can be classified as either internal model based or external model based. Controllers using the internal model are linear and have periodic signal generators in them. Conversely, the external model views the cancellation signal as being injected from outside the basic plant/ controller feedback loop (16). Both the internal model approach, which is sometimes referred to as the Q-filter technique, and the external model approach were employed in this study. The theoretical and architectural details of internal model RLC will now be addressed. Since external model RLC is largely an extension of the internal model concept, the details specific to it will be discussed in a later chapter on controller design.

A common configuration for the implementation of internal model based RLC is shown in Figure 3. This architecture is often referred to as a “Plug-in” repetitive

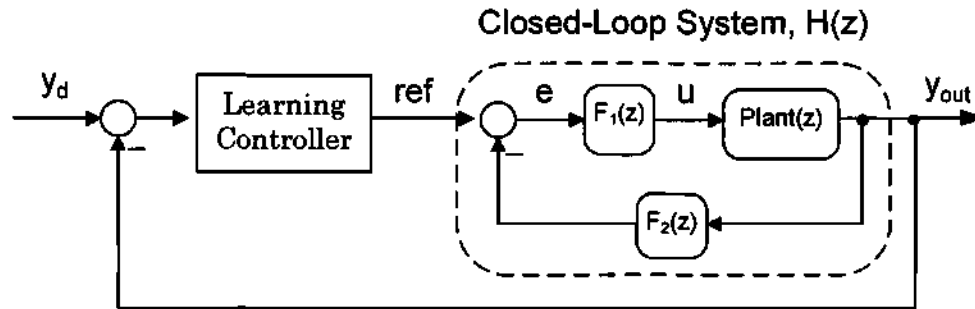


Figure 3 - "Plug-in" repetitive learning controller augmenting a closed-loop plant,  $H(z)$ .

learning controller [e.g., see (4) and (27)] because the compensator is used to augment a nominal system. The block diagram in Figure 4 is a variation on the "plug-in" configuration, herein referred to as the "Bypass" repetitive controller. This configuration is so named because the DC part of the desired trajectory bypasses the repetitive controller so that the RLC only feeds the AC signal necessary to cancel the repetitive errors. Note that the disturbances are shown entering the system at the output; however, since the plant is linear and the magnitude and phase of the disturbances are unknown, the exact point of injection is not important (15).

In Figure 4, the error signal,  $e_r(k)$ , is the difference between  $y_d$  and  $y_{out}$ , the desired output and the measured output, respectively. This signal is fed into the

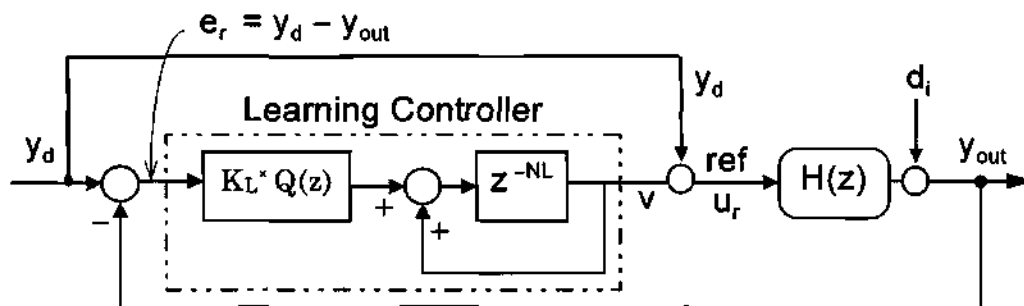


Figure 4 - Diagram of a "Bypass" repetitive learning controller augmenting the closed loop system,  $H(z)$ . Disturbances are shown entering at the plant output.

learning controller, through a gain  $K_L$  and filter  $Q(z)$ . The signal then enters an  $NL$ -step delay positive feedback loop. The resulting signal,  $v(k)$ , augments the unfiltered desired output, thus forming the reference signal  $u_r(k)$ . The positive integer  $NL$  is called the learning cycle length (or learning period or  $CycL$ ) and is the number of discrete steps in one learning cycle.  $NL$  has the units "samples / learning cycle".

An equivalent block-diagram representation of the learning controller in Figure 4 is given in Figure 5. Here the filter  $Q^*(z)$  represents the realizable form of filter  $Q(z)$ . The  $g$ -step delay (where the integer  $g \geq 0$ ) serves to make  $Q^*(z)$  causal and thus realizable in the event that  $Q(z)$  is improper (i.e., relative degree less than zero). Therefore,  $g$  is defined by:

$$g = -1 \times \min\{ 0, \text{relative degree} [ Q(z) ] \} \quad (1)$$

In order to cancel the effect of the  $g$ -step delay, a corresponding shift is added to the repetitive controller to form the companion controller,  $R^*(z)$ . As will be shown in a later chapter, there are times when additional filtering is required in the forward loop of the repetitive controller. This filter will be symbolized by  $W(z)$ . The location

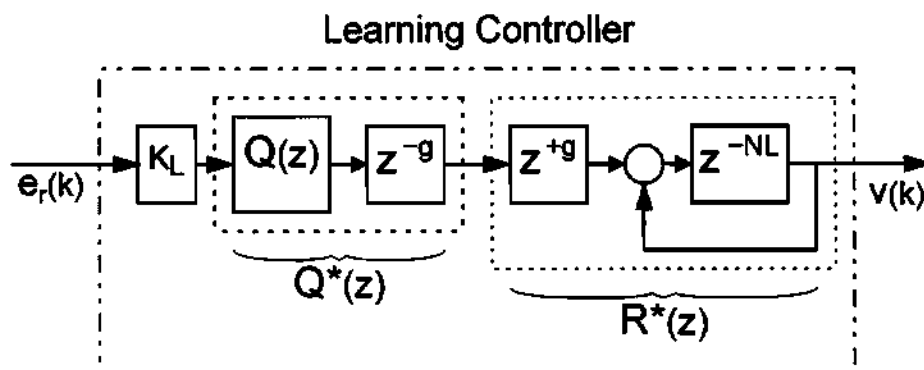


Figure 5 - Learning controller block diagram.  $K_L$ ,  $Q^*(z)$ , and  $R^*(z)$  represent the learning gain, "realizable"  $Q$ -filter, and the companion repetitive controller, respectively.

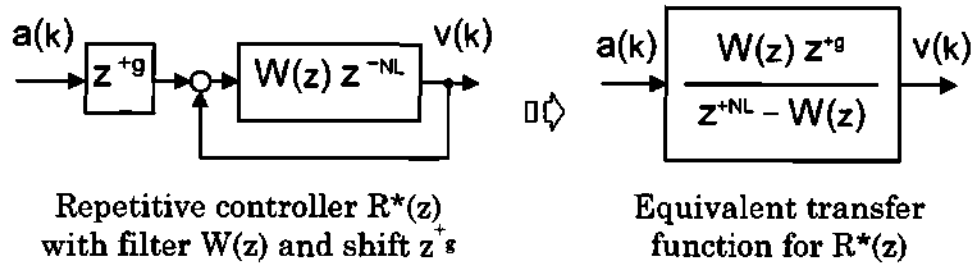


Figure 6 - Block diagrams showing the general form of repetitive controller,  $R^*(z)$  and its equivalent transfer function. Note that the  $z^{+g}$  term cancels the delay term in  $Q^*(z)$  and the linear phase FIR filter  $W(z)$  is for robustness improvement. Setting  $W(z)$  to unity removes it and yields the “pure delay” form of RLC.

of  $W(z)$  in the learning controller formulation is illustrated in Figure 6, along with the equivalent  $z$ -domain transfer function. Setting  $W(z)$  equal to unity reduces the controller to the original (pure delay) form of the repetitive controller,  $R^*(z)$ .

With the internal model  $Q$ -filter approach to RLC, the phase and amplitude of the periodic task and disturbance signals need not be known - only their frequencies. The task and disturbance frequencies are modeled as the combination of some fundamental frequency ( $f_0$ ) and its associated harmonics ( $f_i$ ,  $i=1,2,\dots, NL/2$ ). In this way, the internal model puts marginally stable poles (i.e., on the unit circle) at the same frequencies as the task and disturbance frequencies. This creates an infinite loop gain at these frequencies and thus, drives the error signal [theoretically] to zero. Unfortunately, because of the high loop gains, the controller is sensitive to noise, non-harmonic disturbances, and unmodeled dynamics. Therefore, in practical implementations, compromises between tracking performance, controller robustness, and controller stability are often necessary. Such solutions are discussed and implemented later in this thesis.

### Filtered Repetitive Controller

Since a repetitive controller puts marginally stable poles on the unit circle, there is always the potential for amplifying noise or exciting unmodeled modes, especially in the high frequency range. Typically most, if not all, of a system's harmonic task and disturbance frequencies are in the lower end of the spectrum. Therefore, it may be advantageous from the point of view of robustness to reduce the action of RLC at higher frequencies by incorporating a low-pass filter in the repetitive controller design. In the general form of the repetitive controller given in Figure 6,  $W(z)$  could be such a filter.

A commonly used class of causal digital filters is the infinite impulse response (IIR) type; examples include Butterworth and Chebyshev filters. The inherent phase delay of such filters, however, is often intolerable in control systems, and especially with repetitive controllers. As an alternative, a class of non-causal filter with linear or no phase shift is the finite-impulse-response (FIR) filter. In the  $z$ -domain, a  $p$ -th order FIR filter is of the following form:

$$W^*(z) = b_p \cdot z^p + b_{p-1} \cdot z^{p-1} + \dots + b_0 + b_1 \cdot z^{-1} + b_2 \cdot z^{-2} + \dots + b_p \cdot z^{-p} \quad (2)$$

$$W^*(z) = b_0 + \sum_{i=1}^p b_i \cdot (z^i + z^{-i})$$

which is non-causal because it requires  $p$  future values. The generally high relative degree of repetitive controllers, however, allows us to get around this problem. Define the coefficient vector  $\lambda$  as  $\lambda^T = [b_p, b_{p-1}, \dots, b_1, b_0, b_1, \dots, b_{p-1}, b_p] \in \mathfrak{R}^{2p+1}$  and express the filtered repetitive control T/F in Figure 6 as

$$R^*(z) = \frac{W^*(z) \cdot z^g}{z^{NL} - W^*(z)} \times \left( \frac{z^{-p}}{z^{-p}} \right) = \frac{W(z)}{z^{(NL-p-g)} - W(z) \cdot z^{-g}} \quad (3)$$

where  $W(z) = z^{-p} \cdot W^*(z) = \sum_{i=0}^{2p} \lambda_i \cdot z^{-i}$ . Then, so long as  $NL > g+p$ , both the filter

$W(z)$  and the repetitive controller  $R^*(z)$  are causal and realizable. In this manner, low pass filtering can be added with out the penalty of phase delay. Note that the sum of the coefficients in the vector  $\lambda$  is unity.

The LP filter  $W(z)$  effectively moves the marginally stable high frequency poles of the controller slightly inward off the unit circle. While increasing robustness, this reduces the control action at those frequencies. To illustrate this, define a 2nd order "Least Squares" FIR filter, which has the following vector of coefficients:

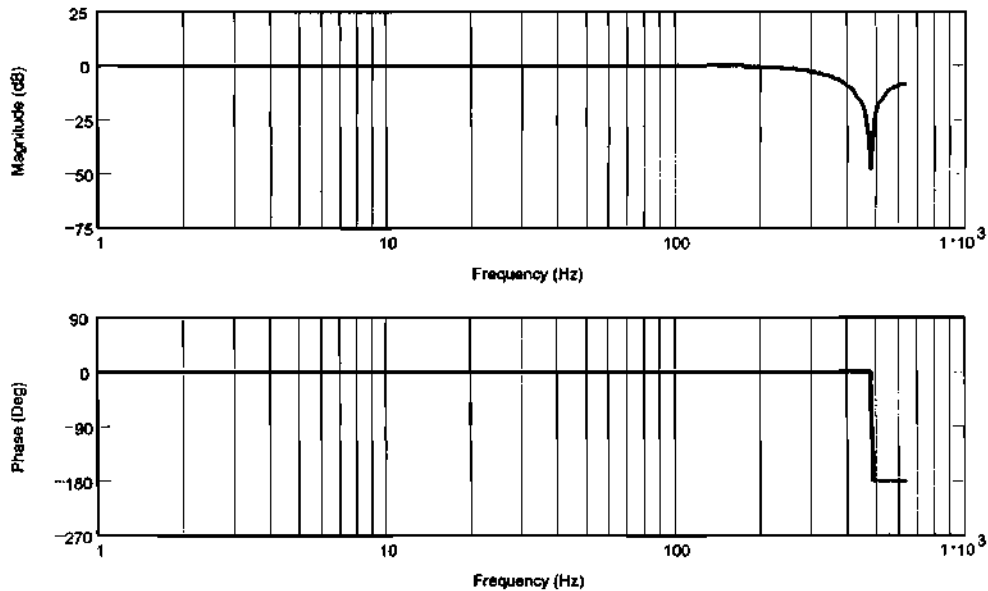


Figure 7 - Frequency response of a 2<sup>nd</sup> order Least Squares FIR low-pass filter. The cutoff frequency (-3dB) is at 300 radians per second and the sample time = 5msec. Note the zero phase shift characteristic all the way to the stop band (~480rad/s).

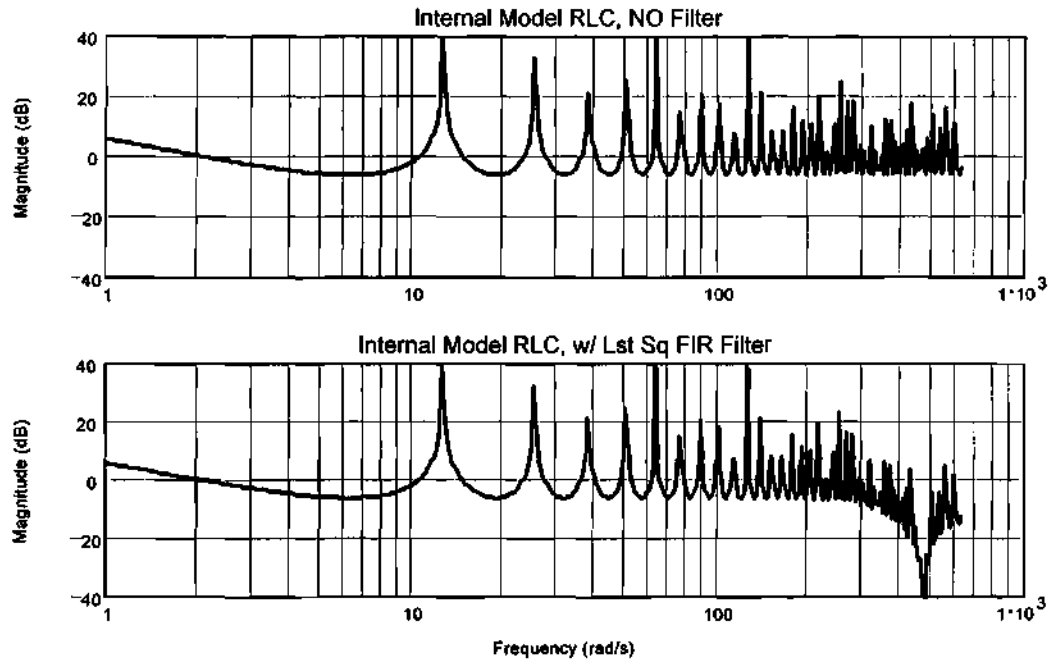


Figure 8 - Two magnitude vs. frequency plots for the transfer functions of an internal model repetitive controller with and without a least-squares FIR filter. Note the decrease in the high frequency attenuation ability of the filtered controller

$\lambda^T = [-0.0857, 0.3429, 0.4875, 0.3429, -0.0857]$ . The frequency response of this filter is given in Figure 7. From the figure, note the zero phase shift characteristic all the way up to the stop band frequency ( $\sim 480$ rad/s). After applying this filter to the internal model controller in Figure 15, the magnitude response of the resulting controller was computed and is plotted in Figure 8.

### The Repetitive Learning Cycle, NL

The fundamental controller frequency ( $f_0$ ) assumed by the internal model in the Q-filter formulation is directly related to the learning cycle, NL.  $f_0$  is selected to be the largest harmonic frequency whose inclusive set of harmonics ( $f_i = i \times f_0$ ,

$i=1,2,\dots, NL/2$ ) contain all of the task and disturbance frequencies ( $t_i$  and  $d_i$ , respectively). So for example, if the task / disturbance frequencies are 20hz, 25hz, and 30hz, the largest controller frequency whose harmonic set contains these frequencies is 5hz. Note that this frequency is the greatest-common-denominator of the task frequencies cited. The learning cycle, NL, is an integer equal to the number of sampling instants contained in one cycle of the fundamental task/ disturbance frequency. Based on the controller sampling time, the learning cycle is selected to give the controller a period proportional to the inverse of the fundamental. The formula for this is as follows:

$$NL = \frac{1}{T_s \cdot f_0} \quad (4)$$

where  $T_s$  is the controller sampling time (seconds per sample) and  $f_0$  is the fundamental frequency (hertz). A detailed account of the specification and implications of NL is given in Chapter 2.

## CHAPTER II

### PERFORMANCE AND STABILITY ISSUES

Theoretically, repetitive learning control (RLC) provides perfect attenuation of cyclic errors by putting infinite gains in the feedforward loop at the frequencies of the periodic task and disturbances. With the Q-filter configuration of RLC, the filter  $Q(z)$  provides the cancellation of the plant's phase shift necessary for stability. Since  $Q(z)$  is usually formed from a plant model or empirical tests, it is subject to approximation inaccuracies. This is especially true at higher frequencies. Hence, the stability and performance of RLC can be compromised by the presence of unmodeled dynamics. Furthermore, altering the loop gain to have strong attenuation at the task/ disturbance harmonics necessarily reduces the attenuation at frequencies between these harmonics. This makes the performance of RLC susceptible to noise and non-periodic disturbances. As will be shown, the goals of stability and perfect attenuation are usually conflicting.

#### General Stability Criteria

The RLC architecture of primary interest in this study is the bypass configuration shown in Figure 9. In order to study the stability of RLC, the z-domain relationship between the error, desired output, and disturbances is found to be

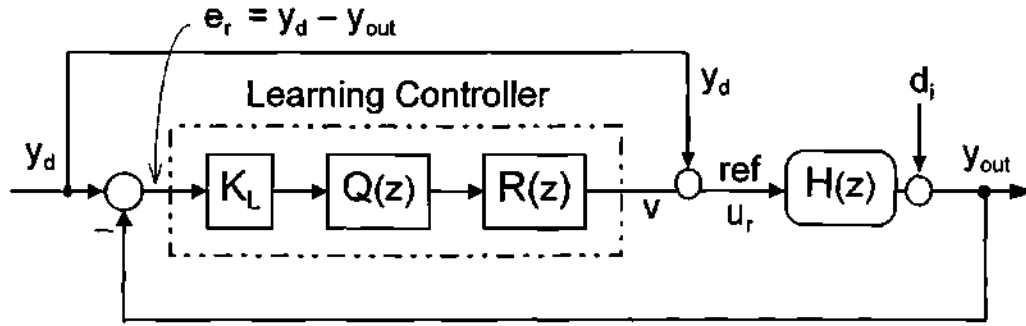


Figure 9 - Bypass repetitive learning control configuration with learning gain  $K_L$ ,  $Q$ -filter  $Q(z)$ , repetitive controller  $R(z)$ , closed loop system  $H(z)$  and disturbances  $d_i$ .

$$E(z) = \frac{1}{K_L \cdot Q(z)H(z)R(z) + 1} \cdot [(1 - H(z)) \cdot Y(z)_{\text{desired}} + D(z)] \quad (5)$$

where  $z = z(\omega) = \exp(\sigma \cdot Ts) \cdot \exp(j \cdot \omega \cdot Ts)$ . Setting the denominator in (5) equal

to zero and recalling that  $R(z) = \frac{1}{(z^{NL} - 1)}$ , we have

$$\left\{ 1 + \frac{K_L \cdot QH(z)}{z^{NL} - 1} \Rightarrow 0 \right\} \rightarrow \left\{ z^{NL} = 1 - K_L \cdot QH(z) \right\}$$

Thus, by the Nyquist criteria, the constraint

$$\left| 1 - K_L \cdot QH(\exp(j\omega)) \right| < 1 \quad (6)$$

with  $-\pi < \omega \leq \pi$ , is nearly necessary for stability (12). To illustrate the boundaries in the complex plane in which condition (6) is satisfied, we represent the open-loop transfer function  $QH$  by

$$QH(z(\omega)) = x(\omega) + j y(\omega), \quad (7)$$

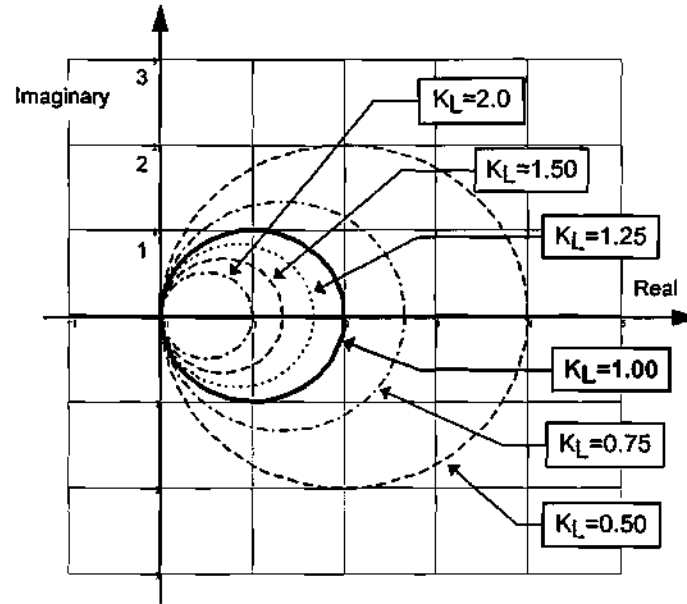


Figure 10 - Complex plane envelopes for the regions in which a system with the open-loop transfer function  $K_L QH(z)$  is stable in the presence of RLC. The boundaries are based on the stability condition in equation (6) and are plotted for several values of learning gain,  $K_L$ . No value of  $K_L$  will provide stability if the phase shift of  $QH(z)$  is greater than  $\pm 90^\circ$ .

where  $x$  and  $y$  are the real and imaginary parts, respectively. The resulting envelopes are plotted in Figure 10 for  $K_L$  values ranging from 0.5 to 2.00. From the figure, we see that both the gain and phase margins increase as  $K_L$  decreases towards its trivial minimum of  $K_L = 0$ . The gain margin is maximized as  $K_L$  is minimized. Note that no value of  $K_L$  will provide stable RLC if the phase shift of  $QH(z)$  is greater than  $\pm 90^\circ$ . Thus, we define the following two stability criteria for an asymptotically stable system subject to repetitive learning control (22):

i)  $\text{Re}\{Q(z_i) H(z_i)\} > 0$ , for  $i = 0, 1, 2, \dots, NL-1$ , where

$$z_i = \exp\left(\frac{2\pi \cdot j}{NL} \times i\right), \text{ and}$$

- ii)  $K_L$  and must be chosen so that the Nyquist diagram of  $z^{-NL} (K_L H(z)Q(z) - 1)$  does not encircle  $-1$  in the complex plane.

The first requirement dictates that the magnitude of the phase shift between  $Q(z)$  and  $H(z)$  be less than  $\pm 90$  degrees at the harmonic frequencies of the repetitive controller. The second requirement limits the value of the learning gain,  $K_L$ , to a value that assures that the roots of the characteristic equation are not unstable. A Nyquist diagram is used to assess stability instead of direct examination of the roots because the characteristic equation of repetitive controllers is often of high order. Solving for the roots of such a system would likely require prohibitive amounts of computation and be subject to inaccuracies. In addition, assessing the resulting data would not be as straight forward as viewing a graphical diagram and checking for encirclement of the  $-1$  point.

### Periodic Disturbances and Tasks

The requirement that the desired output and the system disturbances be harmonics of a fundamental frequency  $\omega_0$  means that  $Y_d(z)$  and  $D(z)$  in Figure 9 are non-zero only at  $\omega_i = i \times 2 \pi \omega_0$ ,  $i = 0, 1, \dots, NL/2$ . Using the equation for  $NL$  given in the previous chapter gives the following expression for  $z$  at the harmonic frequencies,  $\omega_i$  :

$$z_i = \exp(\sigma \cdot Ts) \cdot \exp(j \cdot 2\pi \cdot i) = \exp(\sigma \cdot Ts) \quad (8)$$

Substituting the expression for  $R(z)$  from Figure 6 into the equation for the feedback error ( 5 ), setting  $W(z)=1$ , and recalling that the roots of the RLC are marginally stable (i.e.,  $\sigma \equiv 0 \rightarrow z_i \equiv 1$ ), yields:

$$E(z_i) = \frac{(1 - H(z_i)) \cdot Y(z_i)_d + D(z_i)}{Q(z_i)H(z_i) \left( \frac{1}{z_i^{NL} - 1} \right) + 1} = \frac{(1 - H(z_i)) \cdot Y(z_i)_d + D(z_i)}{Q(z_i)H(z_i) \left( \frac{1}{0} \Rightarrow \infty \right) + 1} \Rightarrow 0 \quad (9)$$

Therefore, if the desired output and the system disturbances have periodic frequencies equal to the harmonics of the RLC fundamental frequency, then the control error will be driven to zero, resulting in theoretically perfect tracking. Unfortunately, if the disturbances are not strictly periodic<sup>2</sup> in time, then the above guarantee of perfect tracking will not hold. This will be proven in the following sections.

### Non-Harmonic Disturbances

It has been previously shown that when the task and all disturbances of a particular system are strictly periodic, the control action of RLC drives the errors to zero. Often, however, a periodic system is subjected to non-harmonic disturbances as well. We seek to determine the effect of such signals on a system under RLC. The following analysis is an extension of the work of T. Inoue (12).

A modified version of equation ( 5 ) is now formed. Since we are concerned only with non-harmonic signals at this time, the user-specified task ( $y_a$ ) (which is

---

<sup>2</sup> A function is "strictly periodic" if it is only dependent on time; i.e., not dependent on another state.

required to be exactly harmonic) is neglected. Thus, after some minor manipulation, the transfer function between the disturbance and the error becomes  $G_d(z)$ :

$$\frac{E(z)}{D(z)} = \frac{1}{K_L \cdot QH(z) \cdot \frac{z^{-NL}}{1-z^{-NL}} + 1} \Rightarrow G_d(z) = \frac{1-z^{-NL}}{1+z^{-NL}(K_L \cdot QH(z)-1)}$$

$$G_d(\exp[j \cdot \omega]) = \frac{1 - \exp[-j \cdot \omega \cdot NL]}{1 + \exp[-j \cdot \omega \cdot NL] \cdot \{K_L \cdot QH(\exp[j \cdot \omega]) - 1\}} \quad (10)$$

$$z = z(\omega) = \exp[j \cdot \omega] \quad (11)$$

where the function in ( 11 ) is periodic in  $\omega$  with period length  $2\pi/NL$ . Because the response to non-periodic signals will differ from frequency to frequency, we simplify the discussion by assuming that the disturbance is defined by a constant power spectrum  $S_d^2$ , similar to that of white noise. Then the power of the control error averaged over one period of  $\exp(j\omega)$  is given by

$$S_e^2(\omega) = \frac{NL}{2\pi} \int_{-\frac{\pi}{NL}}^{\frac{\pi}{NL}} |G_d(\exp[j \cdot (\omega + \lambda)])|^2 \cdot S_d^2 \cdot d\lambda \quad (12)$$

To simplify matters, assume that  $NL$  is large which makes the integration interval small. Thus, the gain of  $QH(\exp[j \cdot \omega])$  is approximately constant over the averaging interval and the averaged power of the control error in equation ( 12 ) can be well approximated by

$$S_e^2(\omega) = A_d(\omega)^2 \cdot S_d^2 \quad (13)$$

$$A_d(\omega)^2 = \frac{2 \cdot \text{Re}\{K_L \cdot QH(z(\omega))\}}{1 - |K_L \cdot QH(z(\omega)) - 1|^2} \quad (14)$$

where

In this form,  $A_d(\omega)^2$  represents the loop gain of the system under RLC at all frequencies  $0 < \omega \leq \frac{\pi}{T_s}$  other than the harmonics of the repetitive controller. Using the representation for  $QH(z)$  in equation ( 7 ),  $A_d(\omega)^2$  can be expressed as:

$$A_d(\omega)^2 = \frac{2 \cdot K_L \cdot x(\omega)}{1 - (K_L \cdot x(\omega) - 1)^2 - y(\omega)^2} \quad (15)$$

In Figure 11, envelopes were generated with  $K_L = 1.0$  for the regions of the complex plane in which  $QH(z)$  is stable. The regions for which  $A_d(\omega)^2$  is less than 1.0 and 1.5 are also plotted as shaded areas. The area for  $A_d(\omega)^2 \leq 1$  represents the complex values of the transfer function  $QH(z)$  in which RLC will not amplify (and may attenuate) a non-harmonic white noise disturbance. The area for  $A_d(\omega)^2 \leq 1.5$  represents the values of  $QH(z)$  in which RLC will not amplify non-harmonic noise by more than 50%. Notice that there is no region in which the dual objectives of stability and non-harmonic disturbance attenuation ( $A_d(\omega)^2 \leq 1$ ) are satisfied. Hence, the conclusion is made that RLC will provide some degree of amplification to error signals that are not harmonic. While zero amplification of non-harmonic disturbances is not possible, there are regions of the stable solution space in which this amplification is relatively insignificant. Since non-harmonic noise signals are typically very small with respect to the amplitudes of harmonic disturbances, a small amount of magnification is usually tolerable and often negligible. It is, however,

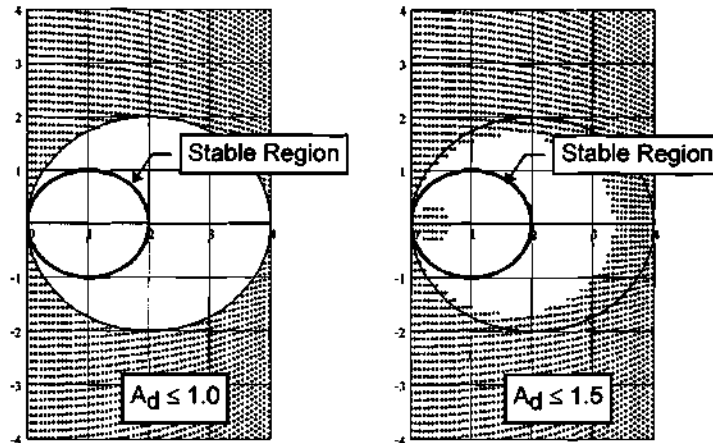


Figure 11 - Complex plane envelopes for  $K_L = 1.0$ . Shown are the regions inside of which (i)  $QH(z)$  is stable (solid line) and (ii)  $A_d(\omega)$  - the amplification factor for non-harmonic disturbances - is less than some threshold (shaded region). Notice that there is no region in which stability and noise attenuation ( $A_d(\omega) \leq 1$ ) coexist. However, when the amplification threshold is raised to  $A_d(\omega) \leq 1.5$ , the shaded envelop expands and enters the "stable region".

important to be aware of the effect that the frequency dependent transfer function  $K_L QH(z)$  has on the amplification of noise. Care must be taken in selecting a Q-filter and learning gain,  $K_L$ , so as to balance the seemingly contradictory requirement of stability with the goal of [white] noise attenuation.

## Finite Attenuation of Periodic Perturbations

### Introduction

Disturbances are found in virtually all mechanical and electro-mechanical systems. These disturbances often result from (or are strongly related to) the rotation of system components. Examples include the runout of shafts, the engagement

and disengagement of gear teeth, the torque ripple of a motor due to commutation, and the movement of cams or other actuators. In such cases, if the components are operating at a constant or near-constant speed, then the disturbances will be periodic. If these disturbances are strictly periodic with respect to time, then the errors can theoretically be driven to zero via the internal model principle. However, as will be shown, if the disturbances are not strict functions of time, then uncancellable tracking error may remain in the presence of RLC. Furthermore, a system with RLC that is shown to be stable under the assumption of strictly time dependent disturbances, can become unstable if this assumption is violated and the magnitude of the disturbance exceeds some threshold.

### Modeling Periodic System Disturbances

In this section, two models for representing periodic disturbances are developed. For clarity, the following assumptions will apply to both:

- a) The system is to operate at a constant speed.
- b) The output or state being controlled is directly related to the rotational velocity of some shaft or component in the system (e.g., the surface speed of a conveyor belt is directly related to the rotational velocity of a roller in constant contact with it via the instantaneous radius between the roller center and the belt).
- c)  $\omega_0$  (radians/sec) designates the frequency of the fundamental disturbance present in the system; additional disturbances may exist at frequencies that are integer multiples of  $\omega_0$ ; i.e., harmonics.
- d) The system is sampled at a constant rate of  $T_s$  (sec/sample).

- e) The cycle length (or learning period) is given by  $NL = \frac{1}{T_s \times \omega_0}$ .

### Classical Disturbance Model

The classical model is so named because it is found in the works of various authors and is relatively straightforward. The primary assumption of this model is that the periodic disturbances are strict functions of time. Hence, the system disturbance at sampling instant  $k$  is modeled by:

$$d(k) = \sum_{i=1}^{NL/2} B_i \times \sin\left(\frac{2\pi \cdot i}{NL} \cdot k + \alpha_i\right) \quad (16)$$

with  $k = 0, 1, 2, \dots$ ; scale factor  $B_i \geq 0$ ; and phase  $|\alpha_i| \leq \pi$ . The sine term in (16) represents the disturbance component resulting from as many as  $NL/2$  periodic perturbations to the system. Note that these perturbations have purely time-dependent frequencies that are multiples / harmonics of a constant fundamental,  $2\pi/NL$  (radians/sample). Researchers such as Kempf et. al. (15) have shown that the tracking errors induced by periodic disturbances which follow this model are driven to zero by an internal model repetitive learning controller.

Unfortunately, in practical situations, the governing assumption that the disturbances be strictly functions of time is often violated. As a result, the guarantee of perfect disturbance attenuation no longer holds. The development of a more appropriate disturbance model follows.

### Modified Disturbance Model

The limitation of the classical model is its assumption that the disturbances are strict functions of time. In actuality, periodic disturbances in rotating machinery are usually functions of the instantaneous angular position or velocity of a rotating component, even though the position of such a component may be a function of time. Modifying the second term in ( 16 ) to reflect this relationship yields the following expression for the system's output velocity error due to harmonic perturbations:

$$d'(k) = \sum_{i=1}^{NL/2} B_i \times \sin(i \cdot \theta(k) + \alpha_i) \quad (17)$$

As before, the summation term on the right side of the equation represents the disturbance component resulting from periodic perturbations. This time, however, the fundamental disturbance frequency (i.e.,  $T_s \cdot i \cdot \omega(k)$  where  $\omega$  is the instantaneous angular shaft velocity) is a nonlinear function of the output angle,  $\theta(k)$ . The following is an analysis of the stability of a repetitive learning control system subject to periodic disturbances that are not strict functions of time. The bypass RLC configuration is shown in Figure 12. The angular position of the output is related to the measured velocity by

$$\theta(k) \equiv \int_{\tau=0}^k \omega(\tau) \cdot d\tau \quad (18)$$

Expressing this relationship in the z-domain,

$$\Theta(z) \equiv P(z) \cdot \frac{z}{z-1} \cdot \Omega(z) \quad (19)$$

where  $\Theta(z)$  and  $\Omega(z)$  are the z-transform equivalents of  $\theta(k)$  and  $\omega(k)$ , respectively, and  $P(z)$  is an asymptotically stable transfer function. Referring to Figure 12, the z-domain expression for the feedback error is

$$\begin{aligned} E &\Rightarrow \Omega_d - D - E \cdot (R + 1) \cdot C \cdot H \quad \text{or} \\ e &= \omega_d - d - e \cdot (r + 1) \cdot c \cdot h \end{aligned} \quad (20)$$

Using the mean-value theorem, the system disturbance can be expressed as

$$d(\theta) = d(\omega_d \cdot t) + \frac{\partial d(\psi)}{\partial \theta} \cdot (\theta - \omega_d \cdot t) \quad (21)$$

where  $\psi$  is a point between  $\theta$  and  $\omega_d \cdot t$ , and  $d(\omega_d \cdot t)$  represents the part of the disturbance that is strictly a function of time.

Assuming that the disturbance  $d$  is composed of some unknown and potentially complex combination of bounded  $\theta$ -dependent sine functions, the derivative in equation (21) is also a bounded combination of sine functions. Let this derivative be represented by  $\gamma(k)$  and let the angular error be given by

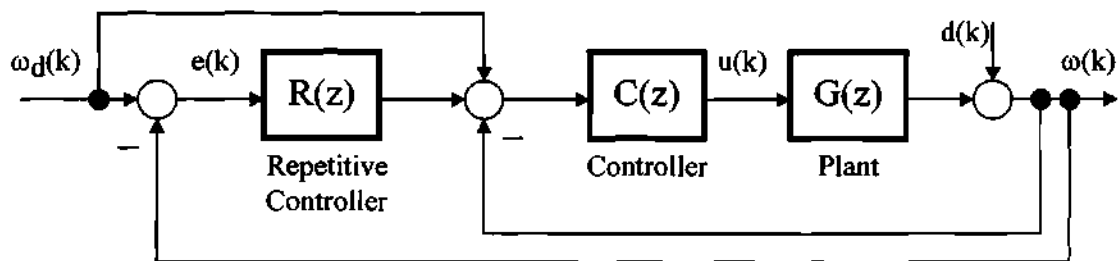


Figure 12 - Bypass repetitive control configuration with plant  $G(z)$ , disturbance  $d(k)$ , feedback error  $e(k)$ , [perturbed] output velocity  $\omega(k)$ , and desired velocity  $\omega_d(k)$ .

$$e_{\theta}(k) \equiv \theta(k) - \omega_d k \cdot T_s \quad (22)$$

where  $T_s$  is the sampling time. Then equation ( 21 ) becomes

$$d = d_t + \gamma(k) \cdot e_{\theta}(k) \quad (23)$$

where  $d_t$  is short-hand notation for the time dependent disturbance component  $d(\omega_d t)$ . The expression for  $e_{\theta}(k)$  in equation ( 22 ) is of the same form as ( 18 ) and can therefore be expressed in the z-domain as

$$E_{\theta}(z) \equiv P(z) \cdot \frac{z}{z-1} \cdot E(z) \quad (24)$$

Next, define the periodic disturbance

$$d_p = d_t - \omega_d \quad (25)$$

Substituting this expression into equation ( 20 ), simplifying, and making use of equation ( 23 ) yields

$$e = -d_p - \gamma \cdot e_{\theta} - e^*(r+1) \cdot c \cdot g \quad (26)$$

$$\text{or, in the z-domain,} \quad E = -D_p - \gamma \cdot E_{\theta} - E \cdot S \cdot C \cdot G \quad (27)$$

where  $S(z) = R(z) + 1$ . Now, assuming that the controller  $C(z)$  has an integrator, the open-loop transfer function  $CG(z)$  can be expressed as

$$CG(z) \equiv \frac{z \cdot W(z)}{z-1} \quad (28)$$

$$\text{Then} \quad CG(z) \cdot E(z) = W(z) \cdot \frac{z}{z-1} \cdot E(z) \quad (29)$$

Defining  $\Lambda(z) = \frac{z}{z-1} \cdot E(z)$ , then equations ( 24 ) and ( 29 ) become, respectively,

$$E_\theta(z) = P(z) \cdot \Lambda(z) \quad (30)$$

and

$$CG(z) \cdot E(z) = W(z) \cdot \Lambda(z) \quad (31)$$

The convolved discrete-time equivalents of these two expressions are  $e_\theta = p * \lambda$  and  $c * g * e = w * \lambda$ , where  $\lambda(k)$  is the discrete-time representation of  $\Lambda(z)$ . Substituting these expressions into equation ( 27 ) gives

$$e = -d_p - s * w * \lambda - \gamma \cdot p * \lambda$$

$$\text{or, in the z-domain} \quad E = -D_p - S \cdot W \cdot \Lambda - \gamma \cdot P \cdot \Lambda \quad (32)$$

We desire a state-space expression for the terms on the right side of equation ( 32 ). Representing the transfer function  $SW(z)$  by the system  $[A_{sw}, B_{sw}, C_{sw}, 0]$  with input signal  $\lambda(k)$ , and letting the state-space representation of  $P(z)$  be  $[A_p, B_p, C_p, 0]$  (also with input signal  $\lambda(k)$ ), we have the following:

$$\begin{aligned} x_{sw}(k+1) &= A_{sw} \cdot x_{sw}(k) + B_{sw} \cdot \lambda(k) \\ y_{sw}(k) &= C_{sw} \cdot x_{sw}(k) \Rightarrow s * w * \lambda \end{aligned} \quad (33)$$

$$\begin{aligned} x_p(k+1) &= A_p \cdot x_p(k) + B_p \cdot \lambda(k) \\ y_p(k) &= \gamma(k) \cdot C_p \cdot x_p(k) \Rightarrow \gamma \cdot p * \lambda \end{aligned} \quad (34)$$

Substituting the output of the above expressions into equation ( 32 ) and letting  $y(k) \equiv -e(k)$ , yields

$$y(k) = -e(k) = d_p(k) + C_{sw} \cdot x_{sw}(k) + \gamma(k) \cdot C_p \cdot x_p(k) \quad (35)$$

Note that the definition of  $\Lambda(z)$  above gives the following relationship in the discrete-time domain:

$$\lambda(k+1) = e(k+1) + \lambda(k) \quad (36)$$

Since  $d_p(k)$  is periodic, the eigenvalues of  $A_{sw}$  include the poles of  $D_p(z)$ . Thus, for a certain initial condition, the Periodic Signal Generation Lemma (Appendix B) states that a periodic function such as  $d_p(k)$  can be generated from the subsystem

$$\begin{aligned} \bar{x}_{sw}(k+1) &= A_{sw} \cdot \bar{x}_{sw}(k) \\ d_p(k) &= C_{sw} \cdot \bar{x}_{sw}(k) \end{aligned} \quad (37)$$

Defining the new states  $\hat{x}_{sw} = x_{sw} - \bar{x}_{sw}$  gives

$$\hat{x}_{sw}(k+1) = A_{sw} \cdot \hat{x}_{sw}(k) + B_{sw} \cdot \lambda(k) \quad (38)$$

so that

$$y(k) = C_{sw} \cdot \hat{x}_{sw}(k) + \gamma(k) \cdot C_p \cdot x_p(k) \quad (39)$$

Since  $y(k) = -e(k)$ , we have

$$e(k+1) = -C_{sw} \cdot \hat{x}_{sw}(k+1) - \gamma(k+1) \cdot C_p \cdot x_p(k+1) \quad (40)$$

$$\begin{aligned} e(k+1) &= -[C_{sw} \cdot A_{sw}] \cdot \hat{x}_{sw}(k) - [C_p \cdot \gamma(k+1) \cdot A_p] \cdot x_p(k) + \\ &\quad - [C_{sw} \cdot B_{sw} + C_p \cdot \gamma(k+1) \cdot B_p] \cdot \lambda(k) \end{aligned} \quad (41)$$

Assuming that the incremental change in  $\gamma$  is small (i.e.,  $\gamma(k+1) \approx \gamma(k)$ ), the state equations can be expressed as  $\chi(k+1) = \underline{A}(k) \cdot \chi(k)$ , where

$$\chi = \begin{bmatrix} \hat{x}_{sw} \\ x_p \\ \lambda \end{bmatrix} \in \mathfrak{R}^{n \times 1} \quad \text{and}$$

$$\underline{\mathbf{A}}(\mathbf{k}) = \begin{bmatrix} \mathbf{A}_{sw} & 0 & \mathbf{B}_{sw} \\ 0 & \mathbf{A}_p & \mathbf{B}_p \\ -\mathbf{C}_{hs} \cdot \mathbf{A}_{sw} & -\gamma(\mathbf{k}) \cdot \mathbf{C}_p \cdot \mathbf{A}_p & -[\mathbf{C}_{sw} \cdot \mathbf{B}_{sw} + \gamma(\mathbf{k}) \cdot \mathbf{C}_p \cdot \mathbf{B}_p] \end{bmatrix} \in \mathfrak{R}^{n \times n} \quad (42)$$

Thus, asymptotic stability of the repetitive control system will be preserved in the presence of periodic disturbances that are not strict functions of time if, for all  $\mathbf{k} > 0$ :

i)  $\gamma(\mathbf{k}) \equiv 0$ , in which case  $\underline{\mathbf{A}}(\mathbf{k}) \rightarrow \underline{\mathbf{A}}$  and  $\left\| \prod_{\tau=\mathbf{k}}^{\mathbf{k}+\mathbf{n}-1} \underline{\mathbf{A}}(\tau) \right\| = \left\| \underline{\mathbf{A}}^{\mathbf{n}} \right\| < 1$

or

ii)  $\gamma(\mathbf{k})$  is sufficiently small such that  $\left\| \prod_{\tau=\mathbf{k}}^{\mathbf{k}+\mathbf{n}-1} \underline{\mathbf{A}}(\tau) \right\| < 1$

Based on this result, the following theorem is stated:

**Theorem 1** For a closed-loop system composed of an exponentially stable plant and a repetitive controller, if the complete system has been proven to be asymptotically stable under the previously stated stability criteria (which implicitly assume that the disturbances are strict functions of time), then the system will remain stable in the presence of periodic disturbances that are functions of angular output position [of the form given in ( 23 )] if the amplitudes of the disturbance components are sufficiently small.

The direct implication of this theorem is that a stable system whose tracking error is predicted to converge to zero in the presence of RLC when perturbed by strictly time dependent periodic disturbances,  $d(\mathbf{k})$ , may not converge (and may even become unstable) if the actual disturbances are not strict functions of time. If, instead of time, the disturbances are functions of the output angle  $\theta(\mathbf{k})$ , then the combined amplitudes of the periodic disturbances must be sufficiently small such that

$\gamma(\mathbf{k}) \cong \frac{\partial d(\mathbf{k})}{\partial \theta}$  remains below some threshold. Otherwise, instability is predicted to occur. Thus, the performance and effectiveness of repetitive control is dependent on the particular system and the nature of the disturbances present. This claim was proven in simulation and will be discussed in a later chapter.

### Cycle Length (NL) Uncertainty and Mismatch

The error and/ or uncertainty associated with the implemented cycle length of a repetitive learning controller can significantly reduce the attenuation capabilities of the controller. This is, of course, in addition to the potentially imperfect attenuation characteristics mentioned in the previous section. The graph in Figure 13 shows the theoretical effect of NL mismatch on attenuation. Notice that for a particular sampling time ( $T_s$ ), as the mismatch percentage increases from zero, the measured RMS error degrades rapidly from the theoretical ideal of zero. In addition, using a larger  $T_s$  significantly increases the effect of learning cycle mismatch on the degradation of RLC attenuation. For the test case studied, the lower and upper horizontal lines represent the design error tolerance and the error achieved without the use of RLC, respectively. Depending on the sampling time chosen, an amount of mismatch beyond some small threshold will result in errors that do not meet the specifications. If the amount of mismatch is even larger, the measured error will be equal to or greater than that which would result without RLC.

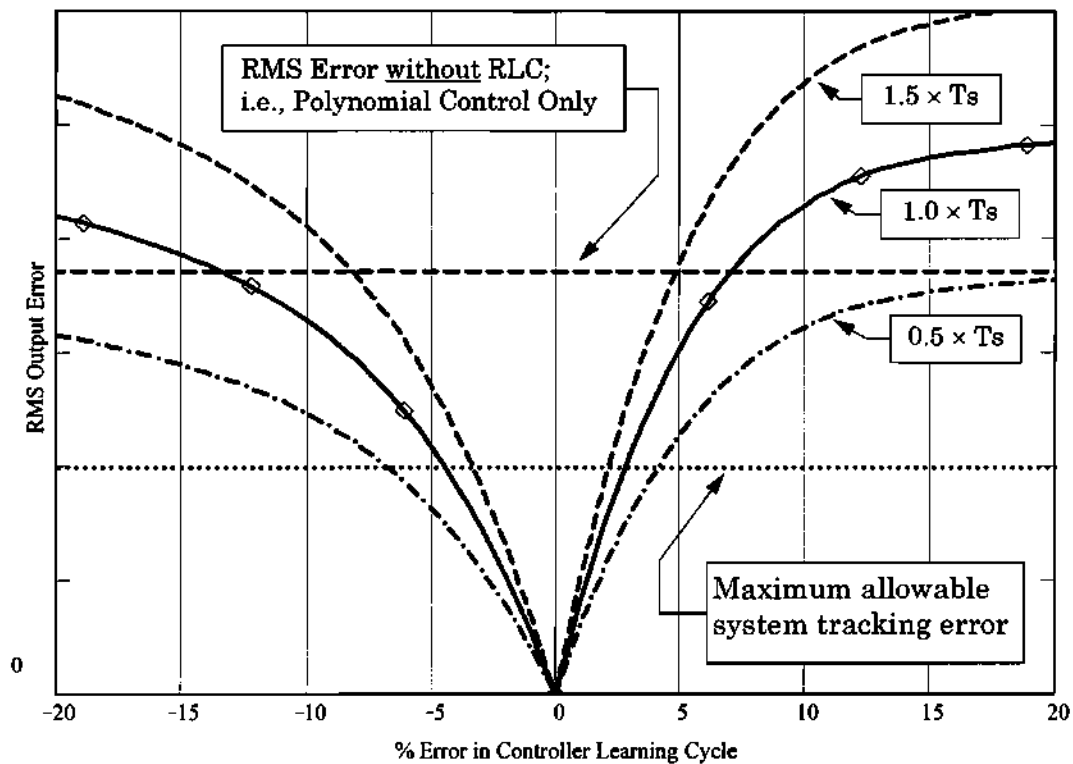


Figure 13 - The effect of learning cycle (NL) mismatch on the RLC error attenuation for three different controller sample times ( $T_s$ ).

Cycle length mismatch can result from either an error in the selection of NL (e.g., a value - say 20 - is selected and the “correct” value is actually 21) or the round-off / truncation error associated with forcing NL to be an integer. The likelihood of a selection error can be reduced significantly by taking careful and accurate system characterization measurements. Errors associated with truncation and round-off, however, are not always so easy to avoid. Since NL represents the number of discrete time delays in the fundamental disturbance / task period, it must be

an integer. The relationship between  $NL$ ,  $T_s$ , and  $f_0$  (the fundamental frequency) was already stated in equation ( 4 ) as

$$NL = \frac{1}{T_s \cdot f_0}$$

If, for example,  $T_s = 0.010$  sec and  $f_0 = 9.6$  Hz, then the cycle length would equal 10.4167 samples/ cycle. Since  $NL$  must be an integer,  $NL \cong 10$  samples/ cycle would be implemented. Unfortunately, the mismatch error associated with this truncation is 4.2%, which the preceding figure shows will result in a large degradation in error attenuation. Two possible solutions to this situation are to:

- i) redesign or modify the plant such that the fundamental disturbance frequency produces an integer  $NL$  (e.g.,  $f_0 = 10.0$  Hz in the case above would make  $NL = 10.00$  samp/ cycle, which results in 0% mismatch), or
- ii) change the sampling time to minimize the mismatch (e.g., in the above example, if  $T_s = 0.0104$  sec, then  $NL$  would be 10.016 samp/ sec, or 0.2% mismatch).

While both solutions are valid, a redesign or modification of an existing system would most likely be impractical. Hence, the second option is the stronger candidate. Note that simply reducing  $T_s$  by an order of magnitude (instead of tuning it) would reduce the mismatch to 1.6% (i.e., if  $T_s = 0.001$ , then  $NL = 104.167 \cong 104$ ). Of course other factors may limit the range of sampling times available. The control engineer must balance all of these factors when implementing RLC.

### Potentially Large NL Values

The periodic disturbance spectrum of a system generally consists of various perturbations from multiple sources which combine to form the total disturbance present at the output. In other words, the disturbance  $d$  is a composite signal that completely contains all of the components. This leads to the following definition:

**Definition 1** If a composite signal is made up of individual signal with frequencies  $f_i$ ,  $i=1,2,\dots$ , then the fictitious fundamental frequency,  $f_0$ , of the composite signal is the greatest common divider of the frequencies in the set  $f_i$ ; i.e.,  $f_0$  is the largest frequency which, when divided into all  $f_i$ , produces an integer.

Note that the fundamental frequency is generically called “fictitious” here because no disturbance may actually exist at this frequency. However, if a single repetitive learning controller is to attenuate all of the component disturbances, then the learning cycle, NL, must be based on this frequency.

This concept is illustrated in Figure 14. Three arbitrary signals with periods of 4, 3, and 2 samples and frequencies of 0.250, 0.500, and 0.333 cycles/ sample, respectively, combine to form a composite signal with a period of 12 samples and a frequency of 0.0833 cyc/ samp. While the periods of the individual signals may be small, the period of the composite signal will be no less than the largest component period and most likely greater. If the three signals represent disturbances to the output of a system, then the composite signal is what would be measured at the output of the system. In this case, a repetitive learning controller would be designed with a [fictitious] fundamental of 0.0833 cyc/samp and a learning cycle equal

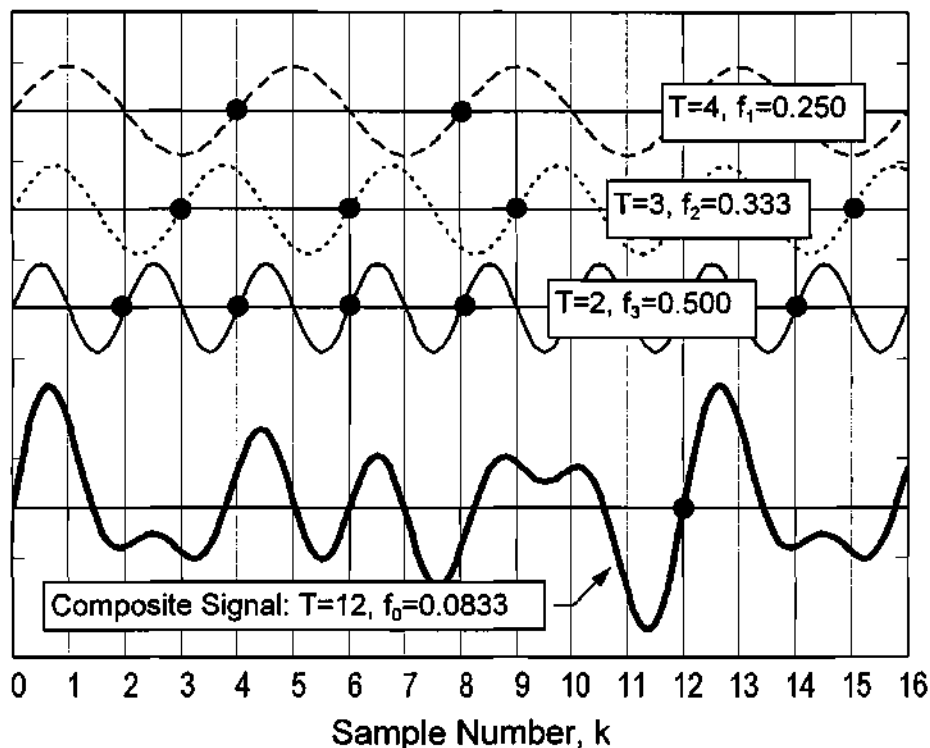


Figure 14 - Illustration of how 3 distinct sinusoidal signals in the discrete-time domain combine to form a composite signal whose periodic frequency is the “fictitious” fundamental of the three components.

to the composite signals period; i.e.,  $NL \Rightarrow 12$  samples. Herein lay a potential problem with the use of single repetitive learning controller.

If some or all of the significant disturbance signals have frequencies that are disparate or close together, then the fictitious fundamental may have a very large period (i.e., a very low frequency). In such a case,  $NL$  could be a prohibitively large number. For example, if the three disturbance components illustrated in Figure 14 had periods of 5.0, 3.0, and 3.5 samples, then the fictitious fundamental of the composite signal would jump from 12 to 105 samples! Clearly, in an actual system

where the frequency spectrum of the disturbances would likely be more diverse, there is the potential for NL to grow very large.

One proposed solution for this phenomenon is to utilize more than one repetitive learning controller in parallel. With such a configuration, the preceding example could use two controllers: one with NL=15 (to account for the two disturbance with periods of 5 and 3 samples) and the other with NL=7 to take care of the third disturbance. A variation on the use of multiple learning controllers is to have the controllers sampling at different rates (multi-rates) from the plant and/ or each other. Only the former technique was studied in this research effort.

### Robustness to Noise and Unmodeled Dynamics

Theoretically, RLC provides perfect attenuation of periodic errors by putting infinite gains in the feedforward loop at the frequencies of the task and disturbances. With the Q-filter configuration for RLC, the filter  $Q(z)$  provides the cancellation of the plant's phase shift necessary for stability. Since  $Q(z)$  is usually formed from a plant model or empirical tests, it is subject to approximation inaccuracies. This is especially true at higher frequencies. Hence, the stability and performance of RLC can be compromised by the presence of unmodeled dynamics. Furthermore, altering the loop gain to have strong attenuation at the task/ disturbance harmonics necessarily reduces the attenuation at frequencies between these harmonics. This makes the performance of RLC susceptible to noise and non-periodic disturbances as well. A solution to this problem was presented in Chapter I where a low pass

FIR filter with zero-phase shift characteristics was incorporated into the controller design. By reducing the controller gain at higher frequencies, the filter increases the closed-loop system's robustness to unmodeled dynamics and noise.

## CHAPTER III

### ALTERNATIVE RLC FORMULATIONS

#### Introduction

Repetitive learning control functions by creating infinite gains in the feed-forward loop at the frequencies of the periodic system disturbances, thereby [theoretically] canceling them in time. As mentioned in the introduction, repetitive controllers can be classified as either internal or external model based. Frequency response plots for an internal and external repetitive controller are given in Figure 15. These plots illustrate the unique gain characteristics of RLC. Visually, the primary difference between the magnitude response of the internal and external model controllers is frequency selectivity. With the internal model controller, infinite gain spikes are placed at all harmonics of the fundamental frequency, up to one-half the Nyquist frequency. This can cause potential problems by exciting unmodeled high frequency dynamics. Implementation, however is straightforward and computational requirements are relatively small.

On the other hand, external model repetitive control allows the individual disturbance harmonics to be selectively included or excluded. When all harmonics are included (up to one-half the Nyquist frequency), the external model repetitive controller reduces identically to the internal model controller. Unfortunately, the computational requirements are much higher for the external model controller. However, as will be shown in a later section, the external model formulation gives it

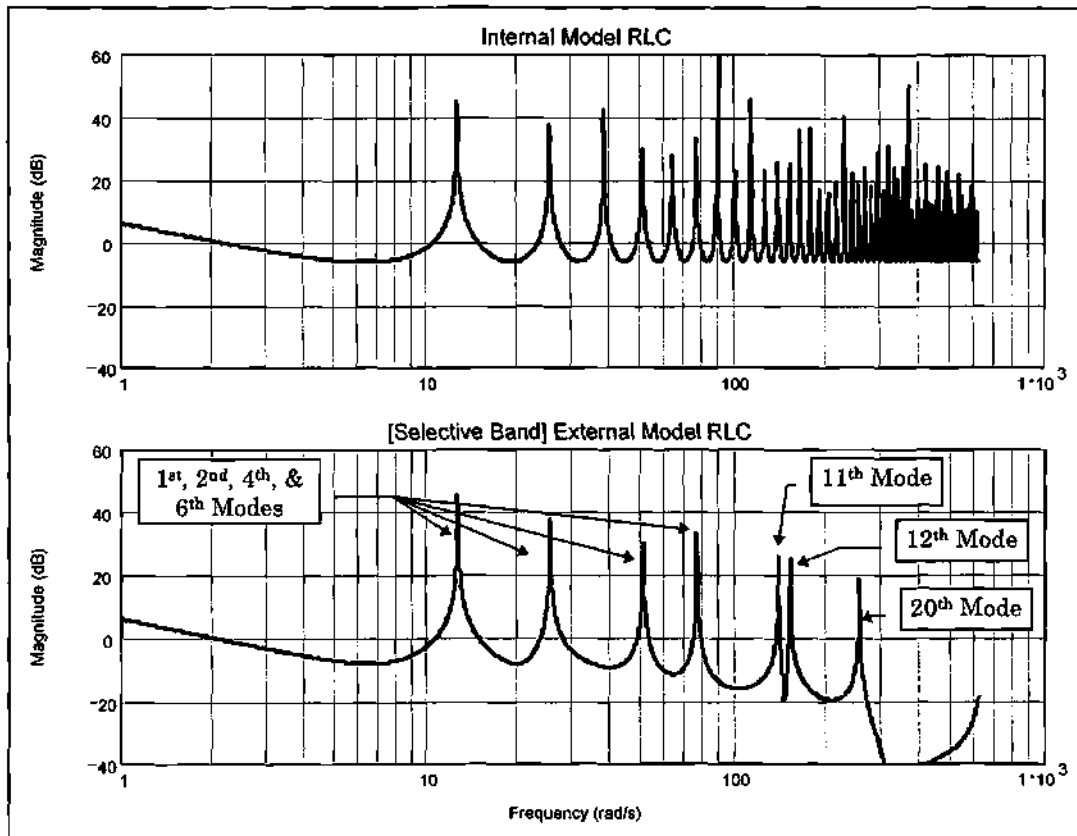


Figure 15 - Frequency response magnitude plots for an internal model RLC (12.56 rad/s fundamental frequency) and an equivalent external model RLC with selective frequency bands. For illustrative purposes, only the 1<sup>st</sup>, 2<sup>nd</sup>, 4<sup>th</sup>, 6<sup>th</sup>, 11<sup>th</sup>, 12<sup>th</sup>, & 20<sup>th</sup> harmonic frequencies were activated.

a powerful adaptation capability that is not possible with the internal model controller.

### Internal Model Repetitive Control

The block diagram for a repetitive controller is shown in Figure 16, along with its transfer function equivalent. The T/F has NL poles at  $|z|=1$  and  $g$  zeros at  $z=0$  if  $g>0$ . To understand the mechanics behind the internal [and external] model

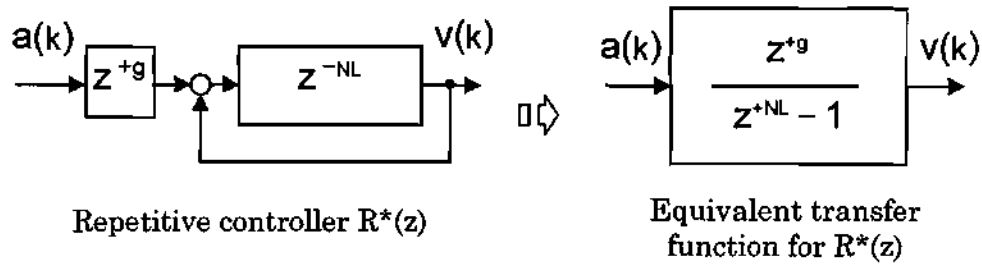


Figure 16 - Equivalent T/F representation of a RLC block diagram with a g-step shift

formulation, note that by partial fraction expansion, the NL-th order T/F can be expressed as the sum of NL separate 1-st order transfer functions. That is,

$$R^*(z) = \frac{z^g}{z^{NL} - 1} \equiv \sum_{i=1}^{NL} \frac{c_i}{z - a_i} \quad (43)$$

where  $c_i$  represents the i-th undetermined coefficient and  $a_i$  is the i-th root given by:

$$a_i \equiv \exp\left(j \frac{2\pi}{NL} \times i\right) = \cos\left(\frac{2\pi}{NL} \times i\right) + j \cdot \sin\left(\frac{2\pi}{NL} \times i\right) \quad (44)$$

Manipulating equation (43) yields the following solution for  $c_i$ :

$$c_i = \frac{1}{NL} \cdot a_i^{g-NL+1} = \frac{1}{NL} \cdot \exp\left(\frac{2\pi j}{NL} \cdot (g+1) \times i\right) \quad (45)$$

for  $i = 1, 2, \dots, NL$ . Thus, we have

$$R^*(z) = \left( \frac{c_{NL}}{z - a_{NL}} + P(z) \right) + \sum_{i=1}^M \left( \frac{c_i}{z - a_i} + \frac{c_{(NL-i)}}{z - a_{(NL-i)}} \right) \quad (46)$$

where M and  $P(z)$  are, respectively, an integer and a transfer function that depend on whether NL is an odd or even integer as follows:

- if NL is EVEN, then  $P(z) \equiv \frac{c_{(NL/2)}}{z - a_{(NL/2)}}$  and  $M \equiv \frac{NL - 2}{2}$ . Otherwise,
- if NL is ODD, then  $P(z) \equiv 0$  and  $M \equiv \frac{NL - 1}{2}$ .

Examining the relationship in equation ( 46 ) between the  $a_i$  and  $a_{(NL-i)}$  terms, as well as the  $c_i$  and  $c_{(NL-i)}$  terms, we note that both sets are complex conjugate pairs; i.e.,  $a_{(NL-i)} = \text{conj}(a_i) = \bar{a}_i$  and  $c_{(NL-i)} = \text{conj}(c_i) = \bar{c}_i$ . Therefore, equation ( 46 ) can be expressed as

$$R^*(z) = \left( \frac{c_{NL}}{z - a_{NL}} + P(z) \right) + \sum_{i=1}^M \left( \frac{c_i}{z - a_i} + \frac{\bar{c}_i}{z - \bar{a}_i} \right) \quad (47)$$

which, after substituting for  $c_i$  and  $a_i$  and simplifying, becomes

$$R^*(z) = \frac{1}{NL} \cdot \left( \frac{1}{z-1} + P^*(z) \right) + \frac{2}{NL} \cdot \sum_{i=1}^M \left( \frac{\cos\left(\frac{2\pi \cdot (g+1) \cdot i}{NL}\right) \cdot z - \cos\left(\frac{2\pi \cdot g \cdot i}{NL}\right)}{z^2 - 2 \cdot \cos\left(\frac{2\pi \cdot i}{NL}\right) \cdot z + 1} \right) \quad (48)$$

Here, the integer M is as defined above and  $P^*(z) = \frac{(-1)^{g+1}}{z+1}$  when NL is even and zero when NL is odd.

By putting the transfer function for the repetitive controller in the form shown in equation ( 47 ) or ( 48 ), it becomes clear that the controller is essentially composed of the combination of a low-gain integral controller (the first term in parentheses on the right side) and M resonant gains at  $\omega_i = 2\pi \cdot i / NL$  radians per sec-

ond for  $i = 1 \dots M$ . Implementing this controller as written would involve numerous calculations, but the internal model repetitive controller gives the equivalent control action by simply using the positive feedback delay arrangement shown in Figure 16. However, with the internal model controller, there is no way to select the resonant modes; i.e., all  $M$  modes will be present in the feedforward loop. This may cause excitation and stability problems due to unmodeled dynamics, especially at higher frequencies. The concept of filtered RLC addressed in Chapter I is a potential remedy for this problem.

### External Model Repetitive Control

The repetitive controller derivation performed in the section on internal model RLC is especially useful in the formulating the external model. It was shown that  $R^*(z)$ , the transfer function of a repetitive controller, can be expressed as the sum of individual 1st order transfer functions:

$$\text{where } R^*(z) = \frac{1}{NL} \left( \frac{1}{z-1} + P^*(z) \right) + \sum_{i=1}^M \left( \frac{c_i}{z-a_i} + \frac{\bar{c}_i}{z-\bar{a}_i} \right) \quad (49)$$

$$a_i \equiv \exp\left(j \frac{2\pi}{NL} \times i\right) = \cos\left(\frac{2\pi}{NL} \times i\right) + j \cdot \sin\left(\frac{2\pi}{NL} \times i\right) \quad (50)$$

$$c_i = \frac{1}{NL} \cdot a_i^{g-NL+1} = \frac{1}{NL} \cdot \exp\left(\frac{2\pi j}{NL} \cdot (g+1) \times i\right)$$

and  $M$  and  $P(z)$  are, respectively, an integer and transfer function that depend on whether  $NL$  is an odd or even integer as follows:

- if NL is EVEN, then  $P^*(z) = \frac{(-1)^{g+1}}{z+1}$  and  $M \equiv \frac{NL-2}{2}$ . Otherwise,
- if NL is ODD, then  $P^*(z) \equiv 0$  and  $M \equiv \frac{NL-1}{2}$ .

Recall that the learning cycle length was defined as  $NL = \frac{1}{T_s \times f_0} = \frac{2\pi}{T_s \times \omega_0}$ , where  $T_s$  and  $\omega_0$  are the sampling time and fundamental controller frequency (rad/s), respectively. Rearranging this expression yields  $\frac{2\pi}{NL} = T_s \times \omega_0$ , which is the same term present in the exponential functions ( 50 ). Replacing  $2\pi/NL$  in those equations yields the following:

$$\begin{aligned} a_i &\equiv \exp(j \cdot T_s \cdot \omega_0 \times i) = \cos(T_s \cdot \omega_0 \times i) + j \cdot \sin(T_s \cdot \omega_0 \times i) \\ c_i &= \frac{1}{NL} \cdot \exp(j \cdot T_s \cdot \omega_0 \cdot (g+1) \times i) \end{aligned} \quad (51)$$

It is through the value of these coefficients that RLC creates infinite loop gains at the harmonics of the fundamental disturbance/ task frequency,  $\omega_0$ . Note that this value is a constant; as a result, for good performance, repetitive controllers of this form (i.e., the internal model or non-adaptive external model) require that the actual fundamental frequency be constant as well. If the harmonic disturbances are strict functions of time, then this condition is satisfied. However, if (as was mentioned in a chapter II) the disturbances are functions of angular position and these disturbances perturb the output velocity, then the fundamental and harmonic frequencies of the disturbance are no longer constant. Instead, they will oscillate about their ideally constant values.

The advantage of the external model formulation is that, despite its increased computational complexity, it allows us to directly alter the fundamental controller frequency over time. In that way, if the harmonic frequencies of the disturbance fluctuate with angular position, then the harmonic frequencies of the repetitive controller can be made to track them adaptively. Before preceding, we simplify the formulation somewhat by letting  $NL$  be even and expressing  $R^*(z)$  as:

$$R^*(z) = \frac{1}{NL} \left( \frac{1}{z-1} + \frac{(-1)^{g+1}}{z+1} \right) + \sum_{i=1}^M \left( \frac{c_i}{z-a_i} + \frac{\bar{c}_i}{z-\bar{a}_i} \right) \Rightarrow V(z) + \sum_{i=1}^M S_i(z) \quad (52)$$

If the discrete-time controller input and output signals are  $u(k)$  and  $y(k)$ , respectively, then the output is obtained by convolving the input and the inverse transform of the discrete controller; i.e.,

$$y(k) = Z^{-1}\{V(z)\} * u(k) + Z^{-1}\{S(z)\} * u(k) = y_v(k) + y_s(k). \quad (53)$$

Simplifying the  $y_v(k)$  component of  $y(k)$  first, we have

$$\begin{aligned} y_v(k) &= \frac{1}{NL} \sum_{\tau=0}^k 1^{k-1-\tau} \cdot u(\tau) + \frac{(-1)^{g+1}}{NL} \sum_{\tau=0}^k (-1)^{(k-1-\tau)} \cdot u(\tau) \\ &= \frac{1}{NL} \sum_{\tau=0}^k u(\tau) + \frac{1}{NL} \sum_{\tau=0}^k (-1)^{(k+g-\tau)} \cdot u(\tau) \end{aligned} \quad (54)$$

$$= \frac{1}{NL} \cdot (\psi_1(k) + \psi_2(k)) \quad (55)$$

where the recursive states are defined and updated as follows:

$$\psi_1(k) = \psi_1(k-1) + u(k), \quad \text{with } \psi_1(0) = u(0) \quad \text{and}$$

$$\psi_2(k) = -\psi_2(k-1) + (-1)^g \cdot u(k), \quad \text{with } \psi_2(0) = (-1)^g \cdot u(0). \quad (56)$$

Next we address the  $ys(k)$  component of the output equation. Substituting for the coefficients and expanding  $ys(k)$  yields

$$\begin{aligned} ys(k) = & \frac{1}{NL} \sum_{i=1}^M \cdot \sum_{\tau=0}^k \exp[j \cdot \omega_0 \cdot Ts \cdot i \cdot (k+g-\tau)] \times u(\tau) \\ & + \frac{1}{NL} \sum_{i=1}^M \cdot \sum_{\tau=0}^k \exp[-j \cdot \omega_0 \cdot Ts \cdot i \cdot (k+g-\tau)] \times u(\tau) + \end{aligned} \quad (57)$$

which can also be expressed as

$$\begin{aligned} ys(k) = & \frac{1}{NL} \sum_{i=1}^M \exp[j \cdot \omega_0 \cdot Ts \cdot i \cdot k] \cdot \left( \sum_{\tau=0}^k \exp[-j \cdot \omega_0 \cdot Ts \cdot i \cdot (\tau-g)] \times u(\tau) \right) + \\ & + \frac{1}{NL} \sum_{i=1}^M \exp[-j \cdot \omega_0 \cdot Ts \cdot i \cdot k] \cdot \left( \sum_{\tau=0}^k \exp[j \cdot \omega_0 \cdot Ts \cdot i \cdot (\tau-g)] \times u(\tau) \right) \end{aligned} \quad (58)$$

If the fundamental frequency  $\omega_0$  is the nominal angular velocity of the output shaft, i.e., the time rate of change in  $\theta(k)$ , then  $\theta(k) = \omega_0 \cdot Ts \times k$  and  $\theta(\tau-g) = \omega_0 \cdot Ts \times (\tau-g)$ .

With this fact, equation ( 58 ) becomes

$$\begin{aligned} ys(k) = & \frac{1}{NL} \sum_{i=1}^M \exp[j \cdot \theta(k) \cdot i] \cdot \left( \sum_{\tau=0}^k \exp[-j \cdot \theta(\tau-g) \cdot i] \times u(\tau) \right) + \\ & + \frac{1}{NL} \sum_{i=1}^M \exp[-j \cdot \theta(k) \cdot i] \cdot \left( \sum_{\tau=0}^k \exp[j \cdot \theta(\tau-g) \cdot i] \times u(\tau) \right) \end{aligned} \quad (59)$$

If we define the time dependent state  $\eta$  and its complex conjugate to be

$$\begin{aligned}\eta_i(k) &= \sum_{\tau=0}^k \exp[-j \cdot \theta(\tau - g) \cdot i] \times u(\tau) \\ \bar{\eta}_i(k) &= \sum_{\tau=0}^k \exp[j \cdot \theta(\tau - g) \cdot i] \times u(\tau)\end{aligned}\tag{60}$$

then these states may be updated recursively as follows

$$\begin{aligned}\eta_i(k) &= \eta_i(k-1) + \exp[-j \cdot \theta(k - g) \cdot i] \times u(k) \\ \bar{\eta}_i(k) &= \bar{\eta}_i(k-1) + \exp[j \cdot \theta(k - g) \cdot i] \times u(k)\end{aligned}\tag{61}$$

Therefore, the equation for the output component  $ys(k)$  becomes

$$ys(k) = \frac{1}{NL} \sum_{i=1}^M \left\{ \exp[j \cdot \theta(k) \cdot i] \cdot \eta_i(k) + \exp[-j \cdot \theta(k) \cdot i] \cdot \bar{\eta}_i(k) \right\}\tag{62}$$

Noting that this expression is composed of the product of two complex conjugate pairs, we define a new set of recursive states based on (61):

$$\begin{aligned}\mu_i(k) &= \mu_i(k-1) + \cos[\theta(k - g) \cdot i] \times u(k) \\ \hat{\mu}_i(k) &= \hat{\mu}_i(k-1) + \sin[\theta(k - g) \cdot i] \times u(k)\end{aligned}\tag{63}$$

where both expressions are real quantities. Thus, after complex manipulation and simplification, equation (62) becomes

$$ys(k) = \frac{1}{NL} \sum_{i=1}^M \left\{ \cos[\theta(k) \cdot i] \cdot \mu_i(k) + \sin[\theta(k) \cdot i] \cdot \hat{\mu}_i(k) \right\}\tag{64}$$

and the complete repetitive controller output equation for the adaptive external model repetitive controller (A-EMRC) becomes

$$y(k) = \frac{1}{NL} \left( \psi_1(k) + \psi_2(k) + \sum_{i=1}^M \{ \mu_i(k) \cdot \cos[\theta(k) \cdot i] + \hat{\mu}_i(k) \cdot \sin[\theta(k) \cdot i] \} \right) \quad (65)$$

where the states  $\psi$  and  $\mu$  are as defined in equations ( 56 ) and ( 63 ), respectively.

Equation ( 65 ) represents an adaptive control law equivalent of a repetitive controller. Note that it has the following three (3) inputs:  $u(k)$ , the current error signal;  $\theta(k)$ , the current angular position of the output shaft or some other shaft(s) whose position is directly related to the disturbances; and  $\theta(k-g)$ , the  $g$ -step delayed angular position. Although it is much more computationally involved than the simple positive feedback delay of the internal model, it offers the following two capabilities:

1. The harmonic frequencies at which the controller puts infinite gains are now selectable. In the summation term in which  $i$  ranges from 1 to  $M$ , the index  $i$  corresponds to the harmonic number. Therefore, instead of summing all of the  $M$  harmonics, a subset of these harmonics can be used.
2. Unlike the internal model which assumes that the controller fundamental frequency is constant (implying that the angular position of the output is a constant-slope ramp function) the A-EMRC uses the actual position to track and adapt to the harmonic disturbance frequencies.

Therefore, if attenuation of only specific harmonics is desired or if the periodic disturbances present are functions of the angular output position instead of time, then the A-EMRC is a superior method of repetitive control. This of course assumes that the increased computational requirements are tolerable.

To gain a more intuitive understanding of what equation ( 65 ) represents, consider the equation for the  $i$ -th harmonic component of a generic disturbance:

$$\begin{aligned} d_i(k) &= A_i \cdot \sin(\theta(k) \cdot i + \phi_i) \\ &\Rightarrow [A_i \cdot \sin(\phi_i)] \cdot \cos(\theta(k) \cdot i) + [A_i \cdot \cos(\phi_i)] \cdot \sin(\theta(k) \cdot i) \end{aligned} \quad (66)$$

where  $A_i$  and  $\phi_i$  are the unknown amplitude and phase, respectively, of the disturbance component. If we let a recursive estimate of the bracketed terms in ( 66 ) corresponding to the unknown constants be designated by  $\mu_i(k)$  and  $\hat{\mu}_i(k)$ , respectively, then equation ( 66 ) becomes

$$d_i(k) = \mu_i(k) \cdot \cos(\theta(k) \cdot i) + \hat{\mu}_i(k) \cdot \sin(\theta(k) \cdot i) \quad (67)$$

which is identical to the summation term in equation ( 65 ). Clearly, the repetitive controller models the harmonic disturbance components and attempts to find the unknown coefficients corresponding to the actual perturbations such that the modeled disturbances match the real disturbances. In that way, by sending the modeled (and inverted) disturbances through the feedforward path, the actual disturbances are canceled.

### Parallel Repetitive Controllers

The chapter on RLC issues introduced the potential problem of having too large a cycle length (NL). As mentioned, when all of the disturbance frequencies are not integer multiples of the same fundamental, then the value of NL for all of the frequencies can be inhibitive large. The experimental test fixture used in this research and detailed in Chapter V provides a good example of this phenomenon.

While virtually all of the disturbances in the fixture are harmonics of a 2Hz fundamental (e.g., 4Hz, 6Hz, 20Hz, etc...), disturbances at other frequencies such as 0.73Hz do exist. These disturbances may be of negligible magnitude and may not normally be considered in designing a repetitive controller; however, for the sake of illustration, we will assume that the disturbance at 0.73Hz is relatively significant.

Assuming a 5msec sampling rate, the learning cycle length for all of the disturbances with 2Hz as a fundamental becomes  $NL = 1 / (5\text{ms} \times 2\text{Hz}) = 100$  samples. If we now want to include the 0.73Hz frequency, we must find the greatest common divisor that will rationally divide (i.e., the quotient is an integer, or nearly an integer). This denominator will become the new [fictitious] fundamental frequency for the repetitive controller. After a few iterations, a fundamental of  $\omega_0 = 0.182\text{Hz}$  is selected because it divides into one frequency (2Hz)  $10.99 \rightarrow 11$  times and it divides into the other (0.73Hz)  $4.01 \rightarrow 4$  times. Thus, we successfully found a common fundamental frequency. However, when the cycle length is recomputed, the previously determined length of 100samples soars to 1,099samples. This number is far too large, from both a memory storage and a transient performance point of view, to be of any practical use. Fortunately, there is another alternative.

Suppose that, instead of using the original repetitive controller to cancel all perturbations, a second repetitive controller is designed specifically for the 0.73Hz disturbance (and its harmonics). Then the cycle length of this second controller would be  $NL_2 = 1 / (5\text{msec} \times 0.73\text{Hz}) \approx 274$  samples. If these two controllers were placed in parallel as shown in Figure 17, then the resulting control action would attenuate all of the disturbance frequencies, while requiring less storage space and

having better convergence characteristics than the single controller equivalent. Magnitude plots for the frequency response of two individual repetitive controllers (RLC #1 and RLC #2 in Figure 17), are provided in Figure 18, along with the response of their combined “parallel” equivalent. The stability proof of the parallel system is now derived.

Let  $R_1(z)$  and  $R_2(z)$  denote two filtered repetitive controllers, each of which has been independently proven to form a stable closed-loop system with an asymptotically stable plant,  $H(z)$ , for some learning gain  $K_L$ . If  $R_1(z)$  and  $R_2(z)$  are placed in parallel with separate gains  $K_1$  and  $K_2$ , respectively, as shown in Figure 17, then the characteristic equation for the closed-loop system with these controller acting in parallel on  $H(z)$  is:

$$1 + H(z) \cdot (K_1 \cdot R_1(z) + K_2 \cdot R_2(z)) = 0 \quad (68)$$

Note that the closed-loop characteristic equation for one controller, say  $R_1(z)$ , acting on  $H(z)$  is  $\{1 + K_1 \cdot R_1(z) \cdot H(z)\}$ . Dividing equation (68) by this expression yields:

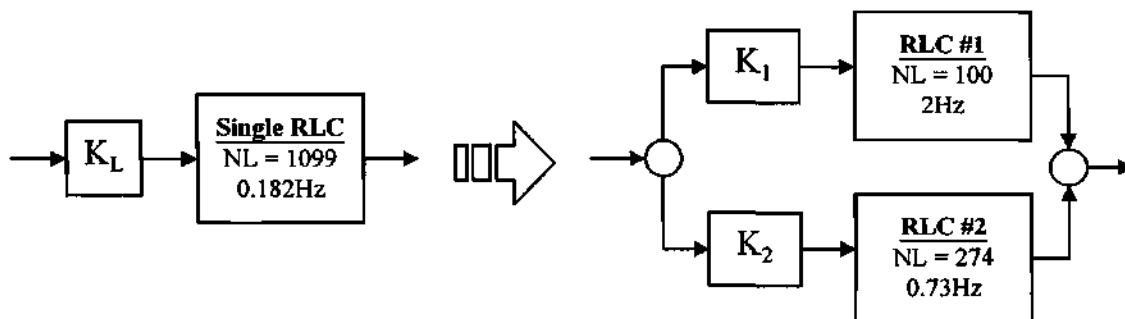


Figure 17 - Schematic illustration of how a single repetitive controller with an prohibitively large learning cycle ( $NL=1099$ ) can be equivalently represented by two (or more) parallel controllers with smaller learning cycles. The learning cycle of each controller is shown, along with its fundamental frequency.  $K_1 + K_2 \leq K_L$ .

$$\frac{1 + K_1 \cdot H(z) \cdot R_1(z)}{1 + K_1 \cdot H(z) \cdot R_1(z)} + \frac{K_2 \cdot H(z) \cdot R_2(z)}{1 + K_1 \cdot H(z) \cdot R_1(z)} = 0 \quad (69)$$

$$\Rightarrow 1 + K_2 \cdot \left( \frac{H(z)}{1 + K_1 \cdot H(z) \cdot R_1(z)} \right) \cdot R_2(z) = 0$$

The expression in parentheses in equation ( 69 ) is the closed-loop transfer function of a system with  $H(z)$  and  $K_1 \cdot R_1(z)$  in the feedforward and feedback paths, respectively. Let this equivalent closed-loop system be designated by  $S(z)$ . Substituting

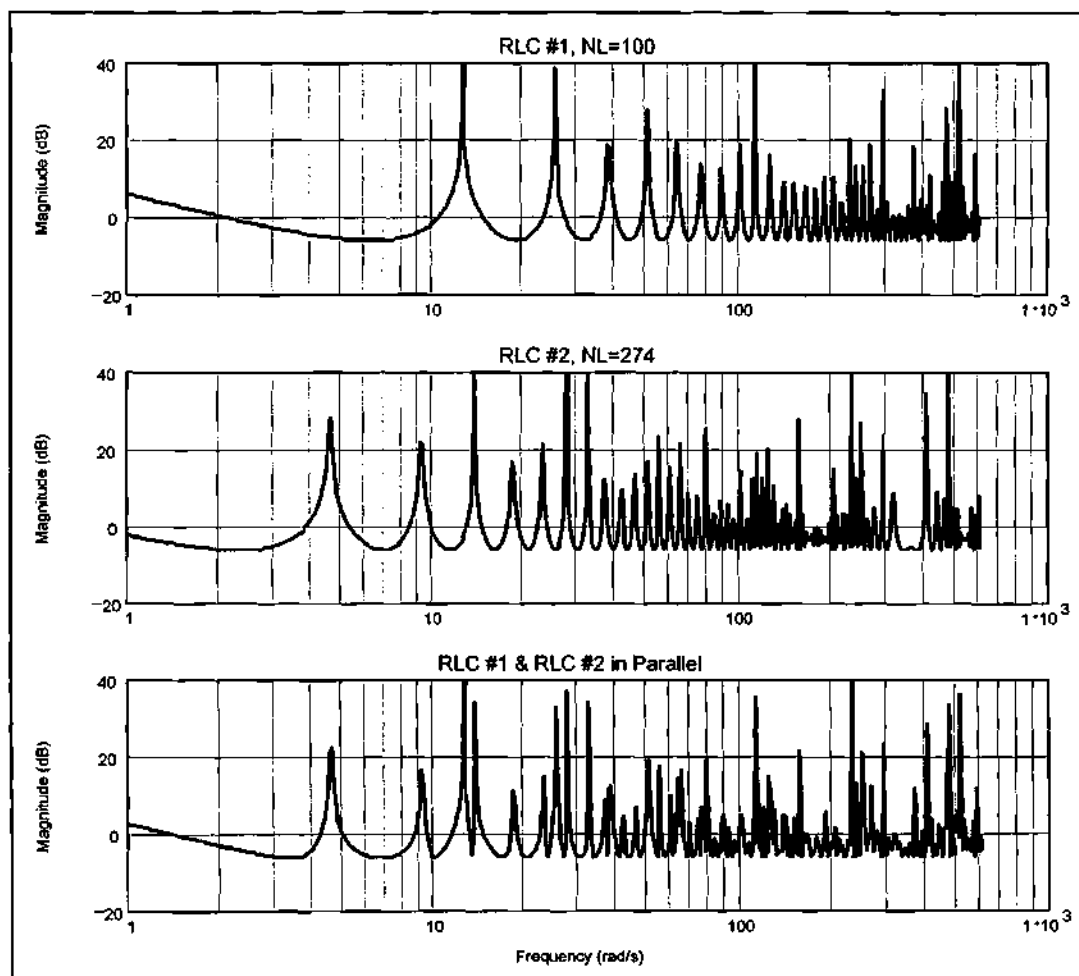


Figure 18 - Three frequency response magnitude plots for RLC #1, RLC #2, and both controllers in parallel, respectively. The parallel configuration has infinite loop gains at the harmonics of both individual controllers.

this into equation ( 69 ) gives the following closed-loop characteristic equation:

$$1 + K_2 \cdot S(z) \cdot R_2(z) = 0 \quad ( 70 )$$

The original requirement that each controller be individually stable for means that  $S(z)$  is stable. Therefore, if two repetitive controllers,  $R_1(z)$  and  $R_2(z)$ , each form stable closed loop systems with a stable plant, then there exists a pair of gains  $K_1$ ,  $K_2$ , where  $K_1 + K_2 \leq K_L$  such that the system whose closed-loop characteristic equation is denoted by equation ( 70 ) is stable under the aforementioned RLC stability criteria (see Chapter II). That is, the Nyquist diagram of  $z^{-NL_2} (K_2 S(z)Q(z) - 1)$  does not encircle  $-1$  in the complex plane, where  $NL_2$  is the cycle length (period) of  $R_2(z)$  and  $Q(z)$  is a stable Q-filter.

### Hybrid Repetitive Controllers

The preceding section shows how two or more repetitive controllers can work together to attenuate different parts of the disturbance spectra. Implicit in that formulation, was the assumption that all controllers in parallel would be of the same type; i.e., internal or external model based. However, in the same way that disturbances with discordant disturbance fundamentals can be effectively handled by two or more repetitive controllers of the same type, different "types" of harmonic disturbances (i.e., those that are strict functions of time versus those that are dependent on angular shaft positions) can be effectively handled by a combination of different "types" of repetitive controllers.

In the sections of this chapter dealing with the formulation of internal and external repetitive controllers, it was shown that both controller types have inherent advantages and disadvantages. The internal model architecture is computationally efficient and, since it assumes a constant disturbance fundamental, works very well at attenuating perturbations that are strictly functions of time. On the other hand, the [adaptive] external model repetitive control (A-EMRC) formulation is more involved computationally, but is able to track a mildly varying disturbance fundamental. Also, A-EMRC can attenuate a select number of disturbance harmonics, as opposed to the internal model which attenuates all harmonics up to one-half the Nyquist frequency. The computational requirements of A-EMRC are directly proportional to the number of selected disturbance harmonics; therefore, the computational complexity decreases as the number of selected harmonics decreases. If the A-EMRC is tuned to reduce only those frequency components that fluctuate, its computational burden on the control system will be minimized.

In many, if not most practical systems, the task and disturbance frequencies present are a combination of the types just mentioned. Therefore, it would seem that superior tracking performance could be realized in such cases by using both an internal and an external model controller (i.e., a hybrid controller) in parallel. This hypothesis turns out to be heuristically true; as the results of this research will show, the hybrid repetitive control configuration produced the best tracking performance of all architectures considered.

## CHAPTER IV

### MULTI-RATE REPETITIVE LEARNING CONTROL

#### Introduction

When two or more digital elements interface with each other, it is important that the sampling rate of each element be compatible with the other(s). The simplest case is when two connected elements have the same rates; then, one element reads the output of the other and then they both update. There are times, however, when elements will have different sampling rates. In such cases, some information loss is likely due to the change in resolution. In digital communications, this situation is called “up-sampling” if the receiving device is sampling at a higher rate than the sending device, or “down-sampling” if the receiving device is sampling at a lower rate. For our purposes, we will assume that the ratio between two interfacing digital elements is an integer,  $m$ .

The concepts of up-sampling and down-sampling are important to RLC because it is often inefficient or impossible to operate repetitive controllers at the same relatively high sampling rate of the open-loop plant’s compensation. Operating at too high a rate can result in an excessively large learning cycle length (NL). If this occurs, then memory storage is wasted and the closed-loop system may be rendered unstable due to the learning controller’s high order. Since the stability criteria for a system under RLC requires a closed-form model, we seek to derive a state-space representation of a closed-loop repetitive control system with its repeti-

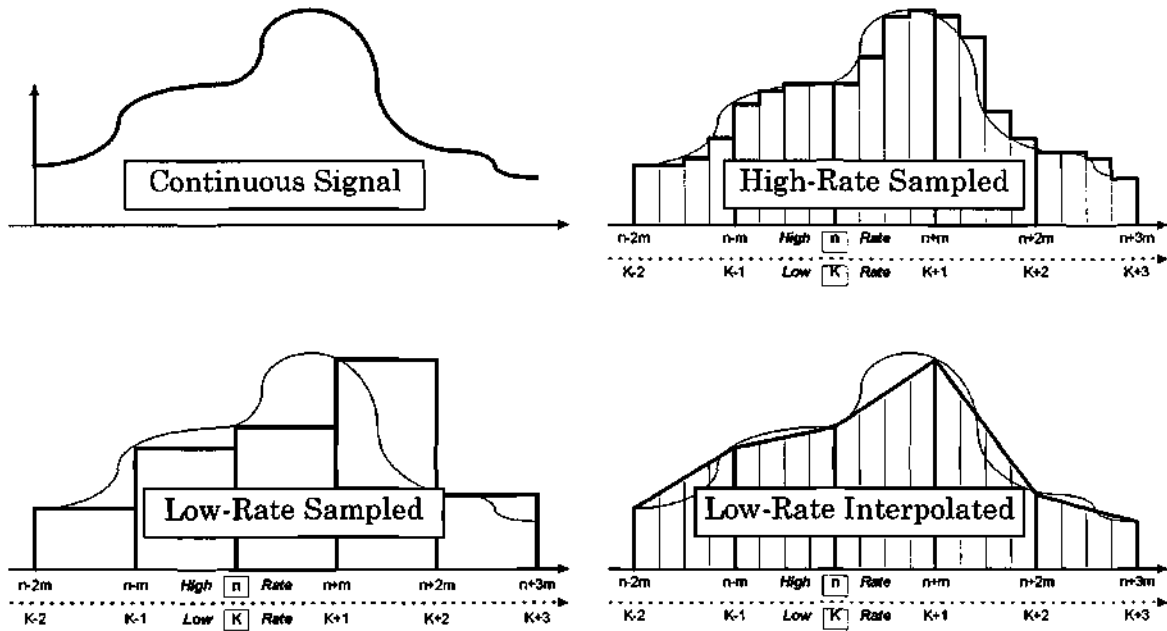


Figure 19 - Four views of a signal: (a) continuous, (b) sampled at high-rate with zero order hold (ZOH), (c) sampled at low-rate with ZOH but reconstructed with linear interpolation (i.e., first order hold). The ratio between the high and low sampling rates as shown is  $m=4$ . The indices for the high and low rates are 'n' and 'K', respectively.

tive controller operating at a slower rate than that of the plant. Then, the previous stability criteria can be extended to this class of controller configurations.

The way in which up-sampling or down-sampling is handled determines the degree to which information is lost. Figure 19 has four different views of the same continuous signal. The first view is the unsampled signal and the second is a digital representation that was sampled at the higher of two rates using a zero order hold (ZOH). Although the very nature of sampling implies that some information will be lost, the high-rate ZOH curve appears to be a good representation of the original signal. The third view is the continuous signal sampled with a ZOH at a low rate

equal to  $1/m$  times that of the high-rate. Finally, the fourth view is a first order hold (FOH) representation that was also sampled at the low rate. Elements from these view will be referenced in the sections that follow. Note that in the figure, the fast sampling rate instants are designated by 'n' and the slow instants are designated by 'K'. This convention will be used throughout this thesis.

### Down-Sampling

Down-sampling is the process of passing a signal from a digital device sampling at one rate to another device sampling at a lower rate. The simplest approach is to ignore the intermediate points and apply a ZOH to every  $K$ -th point. Figure 20 illustrates this method. The rather coarse representation shown is an unavoidable byproduct of the reduction in resolution. However, since most measurements contain some degree of noise, an alternative approach to ignoring the intermediate data points is to sum a weighted average of the previous 'm' points, the future 'm' points, and the current 'K-th' or 'n-th' point. This results in a filtered signal that is less sensitive to noise and abrupt changes in value. Figure 21 shows an example of a

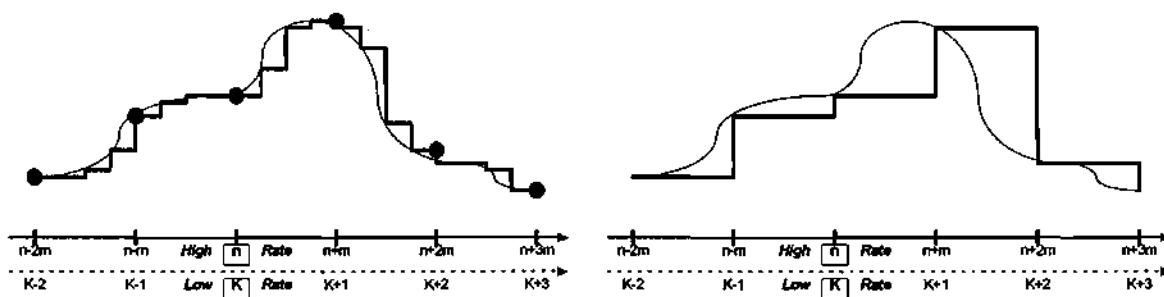


Figure 20 - ZOH Down-Sampling: a signal sampled at one rate is resampled at a slower rate. Here, the faster rate is  $m=4$  times greater than the slower. Therefore,  $m-1=3$  points of data are lost at every  $K$ -th sampling instant.

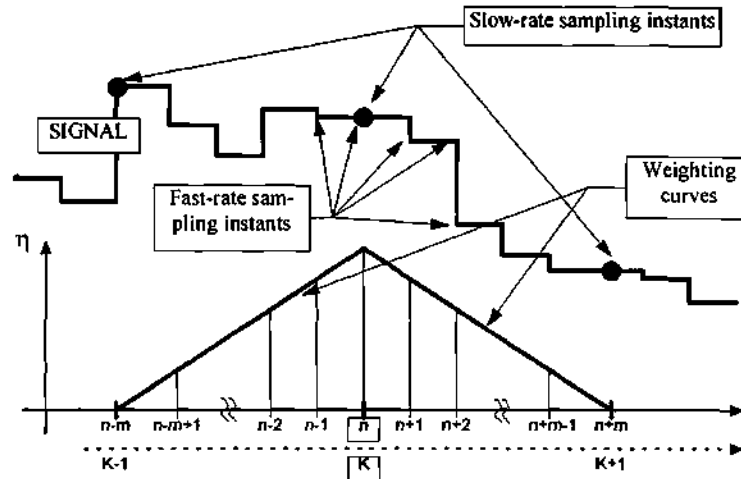


Figure 21 - Linear weighted average curve for the intermediate down-sampling points. The appropriate weight value is applied to the 'm' future and 'm' past fast-rate sample points, as well as the current slow-rate sampling point, K. The  $(2m+1)$  weighted points are summed and the result becomes the 'filtered' signal value at time instant K.

linear weighted average curve and how it would be applied to the inter-sample points of a sample signal. Although the inter-sample points contribute to the filtered signal value, data is only stored at the K-th sampling instants.

### Up-Sampling

Up-sampling is the opposite of down-sampling; i.e., it is the process of passing a signal from one digital device that is sampling at a lower rate to another device sampling at a higher rate. Essentially, the faster device is attempting to take more data than is available. If the slower device uses a ZOH, then the faster device will read  $m-1$  "held" values before reading an updated signal value. In this manner, the higher sampling rate is wasted because no more data is received than if the faster device were sampling  $m$  times slower. This process is illustrated in Figure

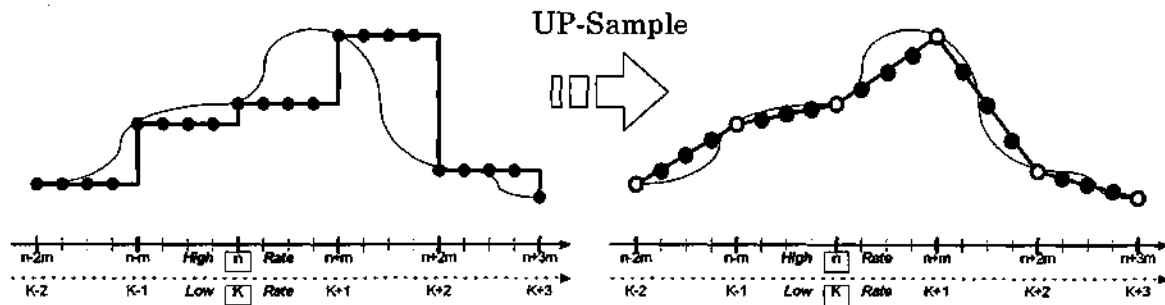


Figure 22 - FOH Up-Sampling: a signal sampled at one rate is resampled at a higher rate. Linear (FOH) interpolation is used to approximate the missing intermediate data points, rather than a ZOH. The interpolated curve clearly produces a better representation of the original continuous curve than the ZOH curve. Here, the faster rate is  $m=4$  times greater than the slower. Therefore,  $m-1=3$  points of data must be created between slow-rate sampling instants.

22. An alternative method is to use linear interpolation between two slow-rate sampling instants to yield a better approximation of the ideally continuous signal. Since interpolation requires a future and a past value, it would seem that a delay is necessary to accomplish this. However, it will be shown in a future section that this can be overcome without adding delay.

### Equivalent Closed-Loop System Transformation

The terminology and methods for interfacing digital system components with different rates have been introduced. A method is now sought to transform a system sampling at a high rate to an equivalent system sampling at a slower rate with up-sampled input and/ or down-sampled output interfaces. Let a linear time invariant (LTI), single input, single output discrete system be represented by the following state-space equations:

$$\begin{aligned} \mathbf{x}(n+1) &= \mathbf{A} \cdot \mathbf{x}(n) + \mathbf{B} \cdot u(n) \\ y(n) &= \mathbf{C} \cdot \mathbf{x}(n) + \mathbf{D} \cdot u(n) \end{aligned} \quad (71)$$

where  $\mathbf{x}(n)$ ,  $u(n)$ , and  $y(n)$  are the state vector, system input, and system output, respectively. The pulse transfer function for the system is  $H(z)$ , the sample time is  $T_s$  (sec/sample) and the corresponding discrete time index is 'n'. We wish to transform the system to an equivalent system sampling at a slower rate of  $T_c = m \times T_s$ , where  $m$  is a positive integer; the discrete index corresponding to this sampling time is 'K'. The system input  $u(n)$  is the up-sampled equivalent of an input signal  $\bar{u}(K)$  sampling at  $T_c$  and  $y(n)$  is the output of the system, which gets down-sampled to a slower rate signal,  $\bar{y}(K)$ . The desired transformation is illustrated in Figure 23.

To apply the state-space stability criteria to a multi-rate system, all components of the system must be transformed to a single-rate equivalent. It is desired that the high-rate system in ( 71 ) be transformed to the same rate as that of a slower sampling controller, while incorporating the effects of up-sampling and/ or down-sampling. The following derivations will first be performed for the case where there is no weighted-averaging down-sampling; i.e., a ZOH sampling at the slower rate ( $T_c$ ) is used and the inter-sample data points are essentially ignored.



Figure 23 - Illustration of a high-rate system with input  $u(n)$ , output  $y(n)$ , and discrete index 'n' being transformed to an equivalent slow-rate system with index K. The effects of any down-sampling and up-sampling are accounted for in the transformation process.

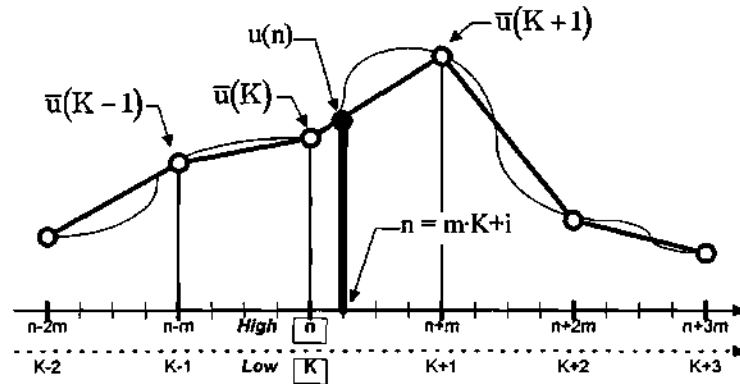


Figure 24 - Linear interpolation of the signal  $u$  at intermediate-sampling instant  $n=mK+i$ .

### Up Sampling Only

The structure of the linear interpolating up-sampler is illustrated in Figure 24. From this, the interpolated control input (still at the higher rate,  $T_s$ ) is given by

$$\begin{aligned}
 u(n) &= \left( \frac{m-i}{m} \right) \cdot \bar{u}(K) + \frac{i}{m} \cdot \bar{u}(K+1) \\
 0 &\leq i \leq m \\
 n &= m \cdot K + i
 \end{aligned} \tag{72}$$

The state update equation for an  $m$ -step increment, subject to the interpolated input in equation (72) is

$$\begin{aligned}
 x(n+m) &= A^m \cdot x(n) + \sum_{i=0}^{m-1} A^{m-1-i} \cdot B \cdot u(n+i) \\
 x(n+m) &\Rightarrow A^m \cdot x(n) + \frac{1}{m} \sum_{i=0}^{m-1} A^{m-1-i} \cdot B \cdot [(m-i) \cdot \bar{u}(K) + i \cdot \bar{u}(K+1)]
 \end{aligned}$$

If we define modified B vectors,

$$B_1 = \left( \sum_{i=0}^{m-1} \left(1 - \frac{i}{m}\right) \cdot A^{m-1-i} \right) \cdot B$$

$$B_2 = \left( \sum_{i=0}^{m-1} \frac{i}{m} \cdot A^{m-1-i} \right) \cdot B$$

then

$$x(n+m) \Rightarrow A^m \cdot x(n) + B_1 \cdot \bar{u}(K) + B_2 \cdot \bar{u}(K+1) \quad (73)$$

The non-causality of this equation presents a problem to implementation and must be removed. Define the following state:  $\bar{x}(K) \equiv x(K \cdot m) - B_2 \cdot \bar{u}(K)$  and increment  $K$  by one which yields  $\bar{x}(K+1) \equiv x(K \cdot m + m) - B_2 \cdot \bar{u}(K+1)$ . Substituting this expression into equation (73) and the output equation in (71) yields

$$\bar{x}(K+1) \Rightarrow A^m \cdot \bar{x}(K) + (A^m \cdot B_2 + B_1) \cdot \bar{u}(K) \quad (74)$$

and

$$y(K) \Rightarrow C \cdot (\bar{x}(K) + B_2 \cdot \bar{u}(K)) + D \cdot \bar{u}(K) \quad (75)$$

$$y(K) = \underline{C} \cdot \bar{x}(K) + (C \cdot B_2 + D) \cdot \bar{u}(K)$$

so that the new state-space system becomes

$$\begin{aligned} \bar{x}(K+1) &= \underline{A} \cdot \bar{x}(K) + \underline{B} \cdot \bar{u}(K) \\ y(K) &= \underline{C} \cdot \bar{x}(K) + \underline{D} \cdot \bar{u}(K) \end{aligned} \quad (76)$$

where

$$\begin{aligned} \underline{A} &\equiv A^m & \underline{C} &\equiv C \\ \underline{B} &= A^m \cdot B_2 + B_1 & \underline{D} &= C \cdot B_2 + D \end{aligned} \quad (77)$$

Thus, the pulse transfer function of the plant transformed to sampling time  $T_c$  and subject to up-sampling only becomes

$$\underline{H}(z) = \underline{C} \cdot (z \cdot \underline{I} - \underline{A})^{-1} \cdot \underline{B} + \underline{D} \quad (78)$$

### Up and Down Sampling

In the preceding analysis, the plant's sampling rate was transformed from  $T_s$  to a slower  $T_c = m \times T_s$ . The formulation of this equivalent system treated the plant input as an up-sample signal from a slower device, but the plant output was assumed to be simply resampled at the slower rate via a ZOH (see Figure 20). In what follows, the original plant will be transformed again, however this time, the down-sampled output will be a weighted average of the high-rate output.

Figure 25 depicts the linear weighting curve used for down-sampling. Since the faster rate is  $m$  times faster than the slower rate, the algorithm will use the previous ' $m$ ', the future ' $m$ ', and the current output to produce a filtered output at the current time instant. Thus,  $2m+1$  weights are needed, the sum of which must be unity. The curve in the figure sets the first and last weighting values to zero, but

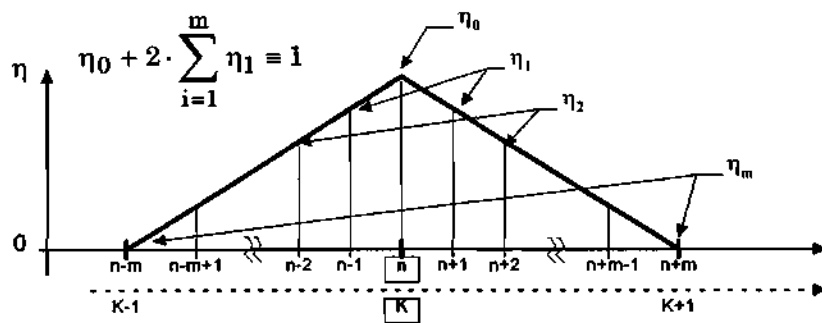


Figure 25 - Linear weighted average curve for the intermediate down-sampling points.

this is not necessary. The formulation will include these weights as well. Letting  $n=K \times m$ , the weighted output at instant  $K$  can be expressed as

$$\bar{y}(K) = \eta_0 \cdot y(K \cdot m) + \sum_{i=1}^m [\eta_i \cdot y(K \cdot m - i) + \eta_i \cdot y(K \cdot m + i)] \quad (79)$$

The  $i$ -th input and output are, respectively

$$u(n - i) = \left(\frac{m - i}{m}\right) \cdot \bar{u}(K) + \frac{i}{m} \cdot \bar{u}(K - 1) \quad (80)$$

$$u(n + i) = \left(\frac{m - i}{m}\right) \cdot \bar{u}(K) + \frac{i}{m} \cdot \bar{u}(K + 1)$$

$$y(n - i) = C \cdot x(n - i) + D \cdot u(n - i) \quad (81)$$

$$y(n + i) = C \cdot x(n + i) + D \cdot u(n + i)$$

Substituting equation (80) into (81) and then substituting that into (79) yields

$$\begin{aligned} \bar{y}(K) = & \eta_0 \cdot y(K \cdot m) + \sum_{i=1}^m [\eta_i \cdot C \cdot (x(K \cdot m - i) + x(K \cdot m + i))] + \\ & + \sum_{i=1}^m [\eta_i \cdot D \cdot (2 \cdot \bar{u}(K) + \frac{i}{m} \cdot (\bar{u}(K - 1) - 2 \cdot \bar{u}(K) + \bar{u}(K + 1)))] \end{aligned} \quad (82)$$

The state vector update equation for ' $i$ ' steps into the future is

$$x(K \cdot m + i) = A^i \cdot x(K \cdot m) + \frac{1}{i} \sum_{j=0}^{i-1} A^{i-1-j} \cdot B \cdot [(i - j) \cdot \bar{u}(K) + j \cdot \bar{u}(K + 1)] \quad (83)$$

$$x(K \cdot m - i) = A^{-i} \cdot x(K \cdot m) - \frac{1}{i} \sum_{j=0}^{i-1} A^{-i-1+j} \cdot B \cdot [(i - j) \cdot \bar{u}(K) + j \cdot \bar{u}(K - 1)] \quad (84)$$

Forming composite **B** vectors for  $1 \leq i \leq m$ ,

$$\mathbf{B}_{2,i} = \left( \sum_{j=0}^{i-1} \frac{j}{m} \cdot A^{i-1-j} \right) \cdot \mathbf{B} \quad (85)$$

$$\mathbf{B}_{1,i} = \left( \sum_{j=0}^{i-1} A^{i-1-j} \right) \cdot \mathbf{B} - \mathbf{B}_{2,i}$$

$$\mathbf{B}_{4,i} = -1 \cdot \left( \sum_{j=0}^i \frac{j}{m} \cdot A^{-i-1+j} \right) \cdot \mathbf{B} \quad (86)$$

$$\mathbf{B}_{3,i} = -1 \cdot \left( \sum_{j=0}^i A^{-i-1+j} \right) \cdot \mathbf{B} - \mathbf{B}_{4,i}$$

Then the state update equations become

$$\begin{aligned} \mathbf{x}(K \cdot m - i) &= A^{-i} \cdot \mathbf{x}(K \cdot m) + \mathbf{B}_{3,i} \cdot \bar{\mathbf{u}}(K) + \mathbf{B}_{4,i} \cdot \bar{\mathbf{u}}(K - 1) \\ \mathbf{x}(K \cdot m + i) &= A^i \cdot \mathbf{x}(K \cdot m) + \mathbf{B}_{1,i} \cdot \bar{\mathbf{u}}(K) + \mathbf{B}_{2,i} \cdot \bar{\mathbf{u}}(K + 1) \end{aligned} \quad (87)$$

Summing these two equations yields

$$\begin{aligned} \mathbf{x}(K \cdot m - i) + \mathbf{x}(K \cdot m + i) &= \left( A^i + A^{-i} \right) \cdot \mathbf{x}(K \cdot m) + \left( \mathbf{B}_{1,i} + \mathbf{B}_{3,i} \right) \cdot \bar{\mathbf{u}}(K) \\ &\quad + \bar{\mathbf{u}}(K + 1) + \mathbf{B}_{4,i} \cdot \bar{\mathbf{u}}(K - 1) \end{aligned} \quad (88)$$

which is substituted back into equation (79). Next, define the following quantities:

$$\bar{\mathbf{C}} = \sum_{i=1}^m \eta_i \cdot \mathbf{C} \cdot \left( A^i + A^{-i} \right)$$

$$\bar{D}_2 = \sum_{i=1}^m \eta_i \cdot D \cdot \frac{i}{m}$$

$$\bar{D}_1 = 2 \cdot \sum_{i=1}^m (\eta_i \cdot D) - 2 \cdot \bar{D}_2$$

$$\hat{D}_1 = \bar{D}_1 + \sum_{i=1}^m \eta_i \cdot C \cdot (B_{1,i} + B_{3,i})$$

$$\hat{D}_2 = \bar{D}_2 + \sum_{i=1}^m \eta_i \cdot C \cdot B_{2,i}$$

$$\hat{D}_3 = \bar{D}_2 + \sum_{i=1}^m \eta_i \cdot C \cdot B_{4,i}$$

Then the transformed output equation becomes

$$\begin{aligned} \bar{y}(K) &= \eta_0 \cdot y(K \cdot m) + \bar{C} \cdot x(K \cdot m) + \hat{D}_1 \cdot \bar{u}(K) + \hat{D}_2 \cdot \bar{u}(K+1) + \hat{D}_3 \cdot \bar{u}(K-1) \\ &= \eta_0 \cdot (C \cdot x(K \cdot m) + D \cdot u(K \cdot m)) + \bar{C} \cdot x(K \cdot m) + \hat{D}_1 \cdot \bar{u}(K) + \dots \\ &= (\eta_0 \cdot C + \bar{C}) \cdot x(K \cdot m) + \eta_0 \cdot D \cdot u(K \cdot m) + \hat{D}_1 \cdot \bar{u}(K) + \dots \\ &= (\eta_0 \cdot C + \bar{C}) \cdot (\bar{x}(K) + B_{2,m} \cdot \bar{u}(K)) + \eta_0 \cdot D \cdot u(K \cdot m) + \hat{D}_1 \cdot \bar{u}(K) + \dots \end{aligned}$$

Let  $\tilde{C} \equiv \eta_0 \cdot C + \bar{C}$  and  $\tilde{D} \equiv \tilde{C} \cdot B_{2,m} + \eta_0 \cdot D + \hat{D}_1$ . Then the transformed system, including the previously defined state vector update equation, is given by:

$$\begin{aligned} \bar{y}(K) &= \tilde{C} \cdot \bar{x}(K) + \tilde{D} \cdot \bar{u}(K) + \hat{D}_2 \cdot \bar{u}(K+1) + \hat{D}_3 \cdot \bar{u}(K-1) \\ \bar{x}(K+1) &= \underline{A} \cdot \bar{x}(K) + \underline{B} \cdot \bar{u}(K) \end{aligned} \quad (89)$$

Unfortunately, it is not possible to find the pulse transfer function of this system in this form since the equation is non-causal. Unlike the previous case (i.e., upsampling only), the  $u(K+1)$  term still appears in the output equation, requiring future values. However, if a repetitive controller precedes the system, then it is

possible to use the structure of the repetitive controller to obtain a causal closed-loop representation of the complete system. Taking  $z$ -transforms of equation ( 89 ) gives the following:

$$\begin{aligned} X(z) &= (z \cdot I - \underline{A})^{-1} \cdot \underline{B} \cdot U(z) \\ Y(z) &= \tilde{C} \cdot X(z) + \tilde{D} \cdot U(z) + \hat{D}_2 \cdot z \cdot U(z) + \hat{D}_3 \cdot z^{-1} \cdot U(z) \\ &= \left[ \tilde{C} \cdot (z \cdot I - \underline{A})^{-1} \cdot \underline{B} + \tilde{D} \right] \cdot U(z) + z \cdot \left[ \hat{D}_2 + \hat{D}_3 \cdot z^{-2} \right] \cdot U(z) \end{aligned} \quad (90)$$

If the two bracketed terms in the equation for  $Y(z)$  are designated by  $H_1(z)$  and  $H_2(z)$ , respectively, then the pulse transfer function becomes

$$\frac{Y(z)}{U(z)} = [H_1(z)] + z \cdot [H_2(z)] \quad (91)$$

If the exponent 'g' of the RLC shift element  $z^g$  is incremented by one, then one delay must be added to the repetitive controller output (i.e., the plant input,  $U(z)$ ) to cancel the shift. This delayed plant input and the resulting causal pulse transfer function are

$$\begin{aligned} U^*(z) &\equiv z^{-1} \cdot U(z) \\ \frac{Y(z)}{U^*(z)} &= z^{-1} \cdot H_1(z) + H_2(z) \Rightarrow \tilde{H}(z) \end{aligned} \quad (92)$$

$$\tilde{H}(z) = z^{-1} \cdot \left[ \tilde{C} \cdot (z \cdot I - \underline{A})^{-1} \cdot \underline{B} + \tilde{D} \right] + \hat{D}_2 + \hat{D}_3 \cdot z^{-2} \quad (93)$$

Therefore, the equivalent slow-rate transfer function of the original “fast” plant with FOH up-sampling and weighted average down-sampling is given by equation ( 93 ), where the constant matrices, vectors, and coefficients are as previously defined.

### Multi-Rate RLC Stability

Figure 26 illustrates a possible configuration for multi-rate repetitive control. The diagram shows the location of both the down-sampler and the up-sampler with respect to the repetitive controller and other system components. Here, the plant samples at the higher rate,  $T_s$ , while the controller and Q-filter operate at the slower rate  $T_c = m \times T_s$ . The T/F defined by equation ( 93 ) can be used to design the Q-filter and to verify the closed-loop stability in accordance with the previously stated criteria for a single-rate system. This formulation requires that the repetitive controller's shift element 'g' be incremented by 1 to account for the delay necessary for transfer function causality. The FOH will also have a delay, which must be added to the controllers shift element too. The extension of the single-rate stability criteria to the multi-rate case is as follows:

**Theorem 2**    Multi-rate RLC Stability - Let  $H(z)$  be the transfer function of an asymptotically stable plant sampling at rate  $T_s$  and subject to up-sampling and down-sampling at its interfaces. If  $H(z)$  can be transformed into an equivalent system,  $\tilde{H}(z)$ , whose input and output are at the slower rate  $T_c = T_s \times m$ , then the closed-loop repetitive control system with a repetitive controller sampling at  $T_c$  (as shown in Figure 26) is asymptotically stable if the following two conditions are met:

$$i) \quad \text{Re}\{Q(z_i) \cdot \tilde{H}(z_i)\} > 0, \text{ for } i = 0, 1, 2, \dots, NL-1, \text{ where}$$

$$z_i = \exp\left(\frac{2\pi \cdot j}{NL} \times i\right), \text{ and}$$

- ii)  $K_L \leq 2$  is chosen such that there is no encirclement of  $-1$  in the complex plane by the Nyquist diag. of  $z^{-NL} (K_L Q(z_i) \cdot \tilde{H}(z_i) - 1)$ .

Thus, given a fast-sampling plant and a slower sampling repetitive controller, if an equivalent plant which samples at the same rate as the controller is found,

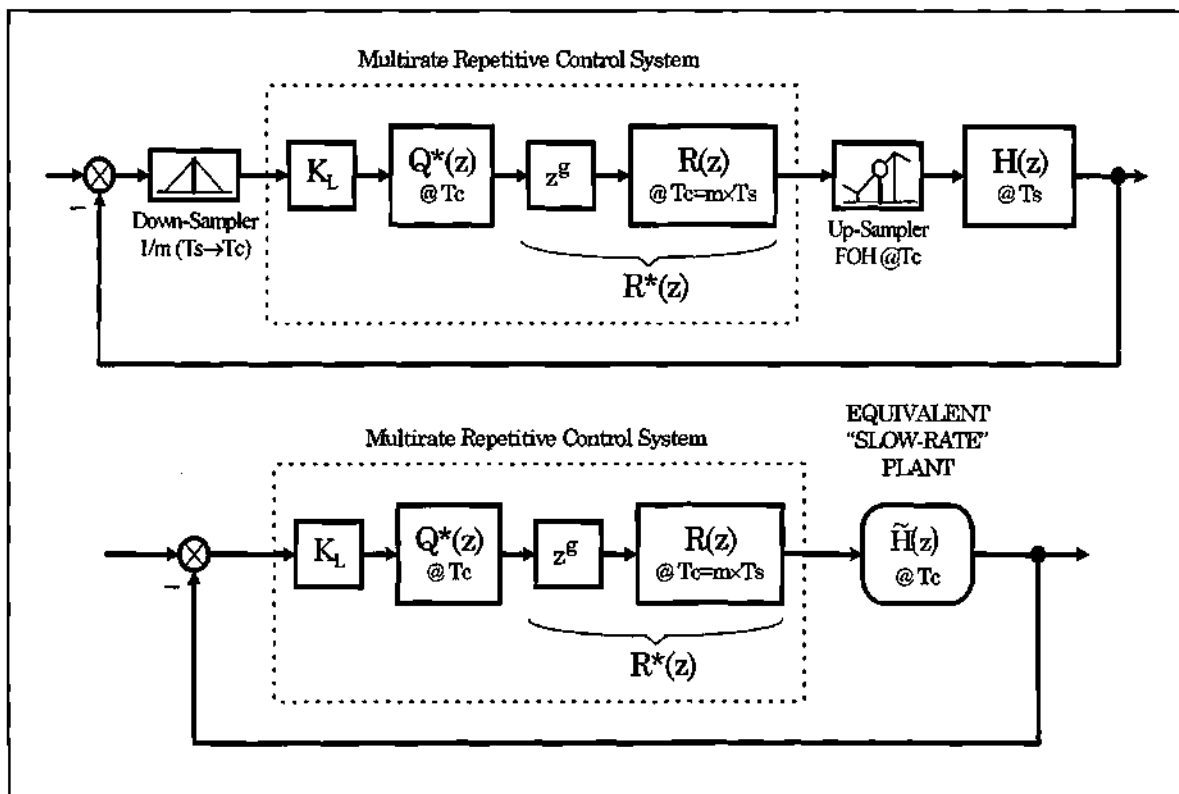


Figure 26- Two block diagrams of a repetitive control system. In the first diagram (multirate case), the plant  $H(z)$  samples at  $T_s$  samples/sec, while the Q-filter and controller,  $R(z)$ , sample at  $T_c = m \times T_s$ . The repetitive controller is shown preceded and followed by a weighted average down-sampler and a FOH up-sampler, respectively, as described in the beginning of the chapter. Each of these add 1 delay to the system, which is compensated for by increasing  $g$  by 2. In the second diagram, the use of the transformed plant,  $\tilde{H}(z)$ , causes the entire system to reduce to a single-rate system.

then the closed-loop repetitive control system reduces to that of a single-rate system and the established stability criteria can be applied.

## CHAPTER V

### EXPERIMENTAL APPARATUS

#### Objective

In order to assess the performance of the repetitive learning control (RLC) technologies developed in this study, a realistic experimental test fixture was needed. The ideal system would inherently have many of the “real-world” electrical and mechanical characteristics that make precise control difficult. A good example of such a system is a xerographic photo-receptor (P/R) module, which is illustrated generically in Figure 27. These modules are at the heart of virtually all photocopiers and laser printers. In the case of a laser printer, the desired image is laid down on the P/R belt medium in closely spaced lines (on the order of 1/600th of an inch apart) prior to developing and transferring it to paper. This process is extremely sensitive to speed fluctuations; tolerable levels of velocity error are often below 0.1% of nominal. Hence, a major control objective of the module is to move the receptive medium (i.e., the belt) with nearly perfect surface velocity. Unfortunately, disturbances due to tolerances and fabrication imperfections make such a stringent control task difficult to achieve. Note that typically the two major sources of disturbance are eccentricities of the rollers and torque ripple of the motor.

In the figure, we see that there are at least three architectural requirements of the P/R module that, by their very nature, frustrate perfect velocity control. First is the considerable distance between the plant input (voltage to the drive motor) and

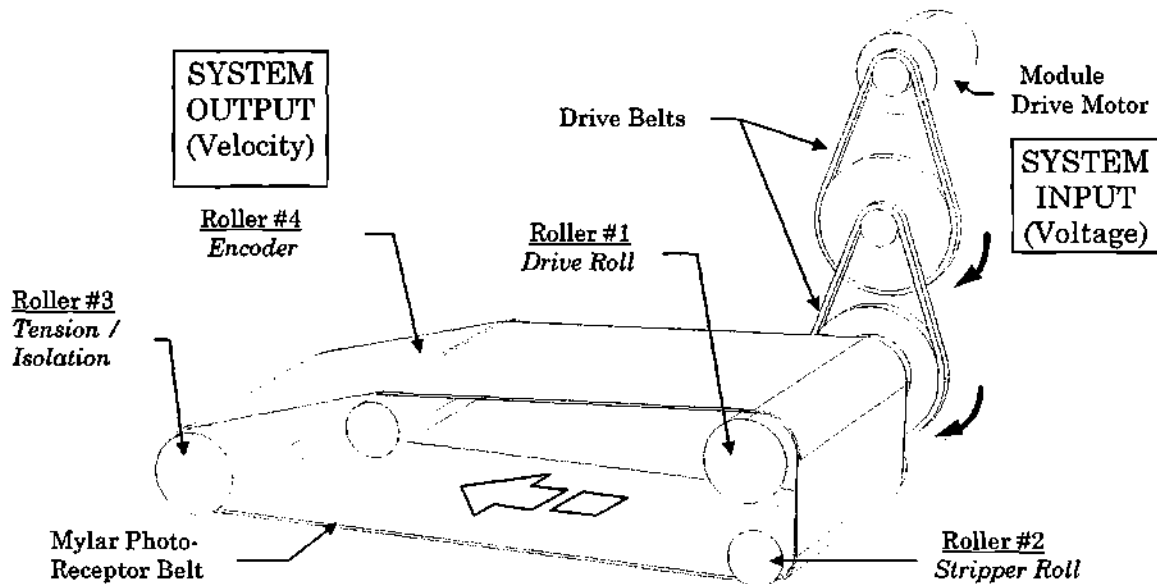


Figure 27- Schematic of a generic 4-roller xerographic photo-receptor module

the plant output (velocity at the encoder, roller #4). Note that in actual systems, the drive motor is often pulse width modulated (PWM) or servo-controlled which require an additional measurement source (i.e., plant output) at the motor. However, for the sake of simplicity and to make the control problem that much more challenging, the only output for the test fixture is at the encoder on the output shaft.

The second architectural attribute is the multiple stage reduction in the drive train via belts and pulleys which adds both noise from the repeated engagement of the teeth and compliance. Third is the connection between the measurement encoder and the rest of the system; this connection is made via the P/R belt which, relative to the rest of the system, has significant compliance. On the other hand, since the P/R belt operates at a constant surface velocity, the rollers and shafts that make up the system rotate ideally at a constant rate as well. If there

are errors or imperfections in these shafts or rollers, then their speed will fluctuate at a constant frequency about some nominal value. The disturbances caused by these fluctuations will have the same constant frequency and period as their source. Hence, this system is a good candidate for the application of repetitive learning control. It should be emphasized that most, if not all, of the aforementioned attributes exist in a variety of practical systems. The P/R module is merely a good example.

### Design Realization

#### Mechanical Subsystems

The goal in developing an experimental test fixture was to incorporate those qualities inherent in systems such as the P/R module which make control difficult, while allowing for the application of RLC. To that end, the following characteristics were considered crucial in the design of a practical apparatus:

- Multi-stage speed reduction. This provides intermediate rotating components which spin at a variety of frequencies and serve as potential sources for harmonic disturbance.
- Toothed timing belt power transfer. The non-slip nature of the teeth preserves the average velocity reduction between two connected members, while providing unwanted (but realistic) velocity perturbations from the tooth engagement.
- A DC motor driver. The inherent high-frequency torque fluctuations (ripple) resulting from commutation are a source of velocity error that is typically very difficult to attenuate.

- A velocity sensor that is located far from the system input so that all or most of the disturbances occur between it and the input.
- Cams to provide both high and low frequency disturbances that are synchronized with the rotation of the drive shafts.
- A hysteresis brake at the end of the power train to provide a ripple-free DC torque load iff/ when needed.
- A relatively compliant member within the power train.

The resulting experimental apparatus is shown in Figure 28. It consists of the following 4 major systems: (1) a motor subsystem which has voltage as an input and torque via a 10-tooth pulley as an output; (2) a Hi-Cam (or high frequency cam)

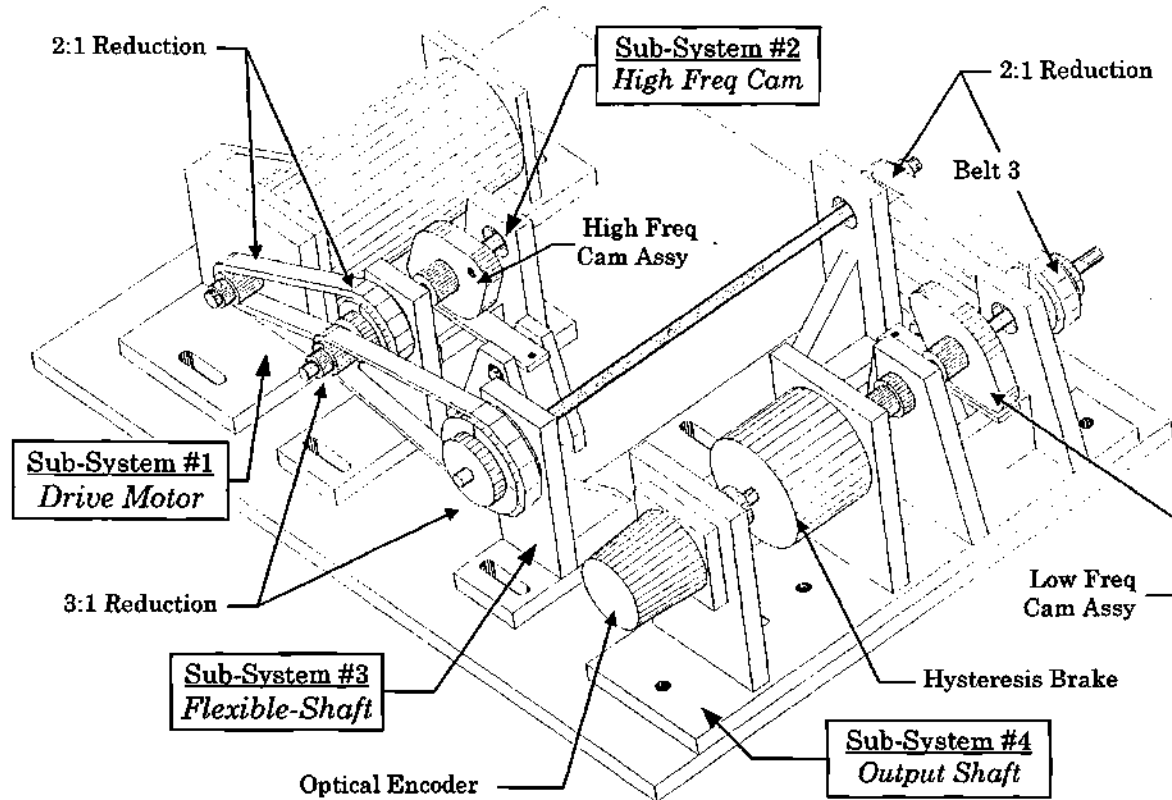


Figure 28 - Diagram of the research test fixture with all four major sub-system shown.

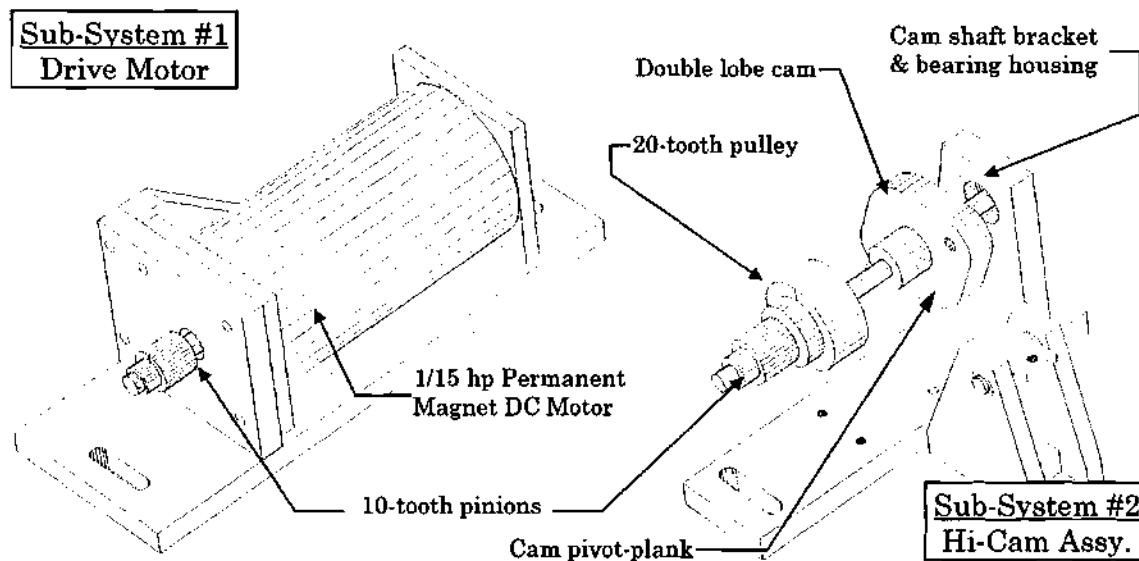


Figure 29 - Detailed illustration of subsystems 1 and 2. Note that the front bracket for the cam shaft is omitted for clarity. Also, the tension spring for the cam's pivot-plank is not shown.

subsystem which connects to the motor via a 2:1 gear reduction and imparts a perturbation whose frequency is equal to twice the Hi-Cam's rotational speed; (3) a Flex-Shaft (or torsionally flexible shaft) subsystem connected to the Hi-Cam subsystem by a 3:1 gear reduction; and (4) an output shaft subsystem which connects to the Flex-Shaft subsystem via a 2:1 reduction -- this subsystem includes a Low-Cam (or low frequency cam) coupled to a hysteresis brake, which in turn is coupled to an optical encoder for output measurement. Power is transmitted between subsystems by three 1/5" pitch timing belts. The entire speed reduction between the motor and the output shaft is 12:1 which is on par with reductions found in systems like the P/R module.

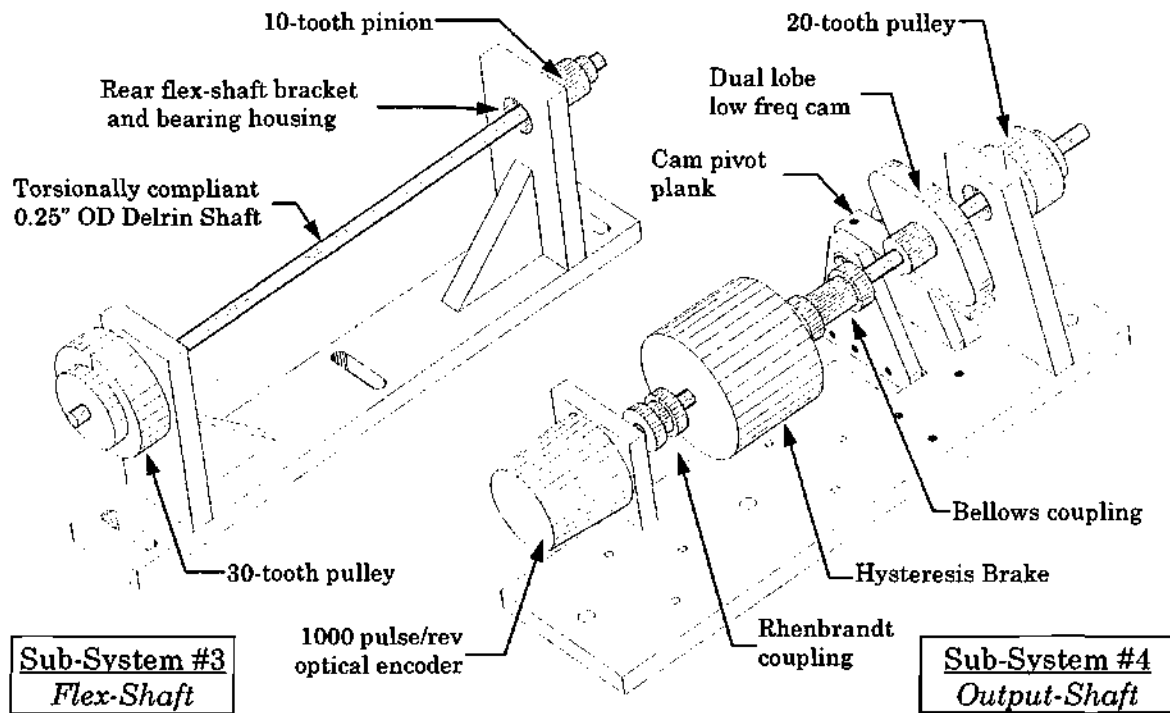


Figure 30 - Detailed illustration of subsystems 3 and 4. Three of the vertical bracket for the output shaft assembly are omitted to show the shaft couplings.

The first two subsystems are illustrated in greater detail in Figure 29 and the other two subsystems are similarly illustrated in Figure 30. In both figures, the relative scale between the two subsystems is preserved. The slots in the base plates of assembly 1 through 3 allow for disassembly and easy adjustment of the timing belt tensions. The high and low frequency cams run against a pivoted steel plank bar. On the other side of the pivot point (i.e., the short side) is a hole that connects to a vertically mounted extension spring (not shown). As the cam actuates, it applies a greater force on the pivot plank causing it to deflect and extend the tension spring further. The force necessary to deflect the plank results in an increase in the

torque of the cam shaft. The frequency and magnitude of this disturbance are direct functions of the cam shaft's angular position.

Kinematic analysis techniques were used to design the cam profile and pivot point location such that the maximum torque on a lubricated cam would not exceed 20 in-oz. The resulting profile for torque versus cam shaft angle is given in Figure 31. From the graph, we see that one complete cam shaft rotation (i.e., one cycle) produces two cycles of the cam disturbance torque. This is because of the dual lobe design of the cams. Hence, the frequency of the disturbances produced by these cam assemblies will be twice that of their respective shafts. The torque profile due to a single lobe is not symmetric because of the dynamic location of the cam contact point, with respect to the pivot point of the plank. Notice that, for a certain segment of the cam's rotation (indicated by the negative torque in the figure), the pivot plank energizes the cam and the system.

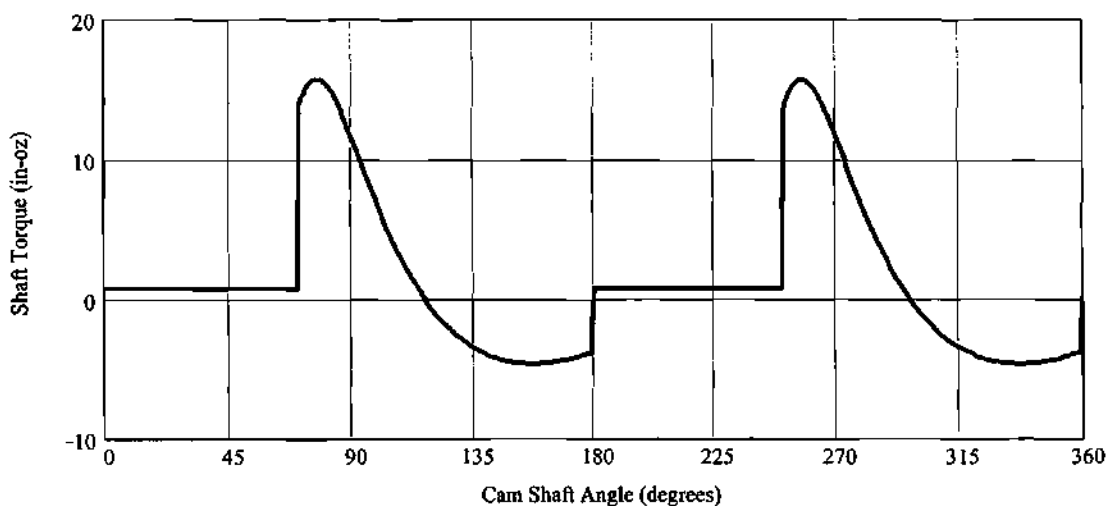


Figure 31 - Torque profile of a cam assembly as a function of rotation angle. The twin curves are due to the cam's dual lobes. Note the small positive torque offset; this is the torque required to overcome coulomb friction during the cam's dead zones.

## Electrical Subsystems

The mechanical system described in the previous section required actuation and control. Power for the motor was provided by a voltage-following DC power supply. The voltage gain between the input and the output was equal to 10. At the output of the fixture, the encoder produced a TTL (true-true-logic) pulse train whose frequency was 1000 times the instantaneous frequency of the output shaft. To convert this signal to a meaningful quantity, one of two things was done, depending on whether shaft position or velocity was desired. To measure position, the pulses were counted and used to determine the shaft's angular position relative to startup. For velocity, the pulse train was feed to a frequency-to-voltage (F-V) converter which in turn output a voltage that was proportional to the instantaneous frequency of the encoder shaft.

A schematic of the entire system is given in Figure 32, where the components within the dashed line comprise what will herein be referred to as the open-loop plant,  $G(z)$ . The input is a voltage that is amplified to provide sufficient power to the drive motor. As mentioned above, the output is a TTL pulse whose instantaneous frequency and count are proportional to the instantaneous angular velocity and position, respectively, of the system's output shaft. Analysis of the F-V output reveals a significant noise spike at the frequency of the pulse train, which is approximately 2kHz for this study. Since we are only interested in the F-V's DC output and the AC content below 200hz (i.e., the controller's Nyquist frequency), an analog filter was added as shown in Figure 32 to remove all frequencies above 600Hz. This

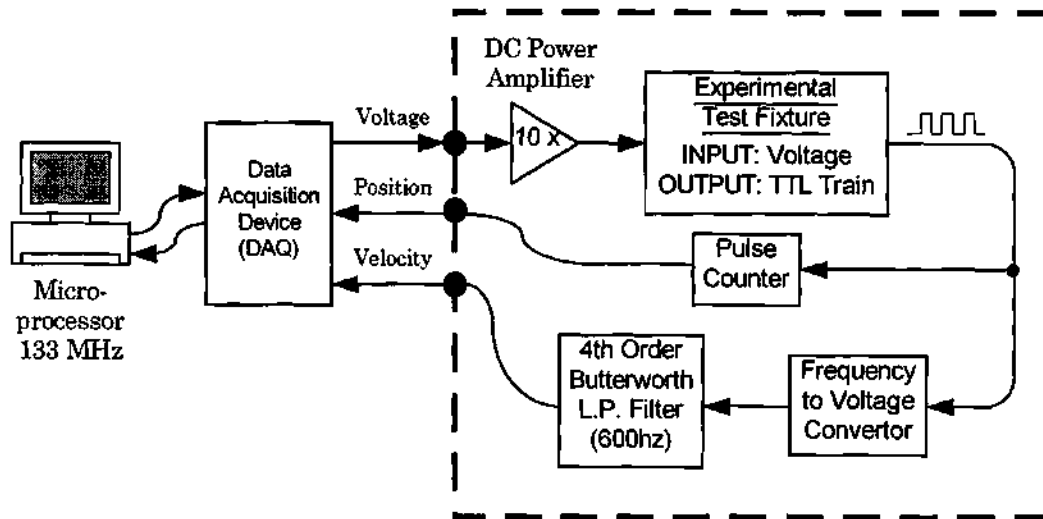


Figure 32 - Signal flow diagram of the test fixture and electrical interfaces. The components within the dashed boundary constitute the open-loop plant,  $G(z)$ . Voltage to the plant is a low current signal from the DAQ which is amplified and sent to the motor. The two outputs shown are the logical angular position and a voltage proportional to the instantaneous output shaft velocity. All control and analyses were performed in software on a Pentium computer running Windows NT.

seemingly high cutoff frequency was selected over a lower choice, say 250hz, in order to minimize the phase shift induced by the filter for frequencies below 200hz.

The electronic interface was a National Instruments data acquisition board with 2 analog outputs, 8 analog inputs, an onboard counter/ timer with 5 channels, and 8 digital I/O lines. For this research, only one output, one input, and one gated channel were needed. All of the analysis and control were accomplished in software using LabWindows/ CVI C-code, Matlab, and/ or an HP 3562A signal analyzer. The details of the components contained in the mechanical and electrical subsystems of the test fixture are summarized in Appendix A.

### System Characterization

Once the test fixture design was finalized and the system was fabricated, assembled, and debugged, the next step was to obtain a dynamic characterization. To accomplish this, a series of frequency response (F/R) tests were performed on the open-loop system. It should be noted that the desired output of the test fixture is 2rev/sec and the smallest practical sampling rate for the DAQ board was 2.5msec. The F/R measurements, however, were done using an HP 3562A dynamic signal analyzer which allowed for an even faster sampling rate.

#### Open-Loop Transfer Function

Since there were non-linearities present, the excitation for F/R measurements was selected to be a  $\pm 0.3$ volt sinusoidal perturbation on top of a 3.6volt DC carrier voltage. This choice of DC voltage resulted in an average system output velocity that was approximately equal to the reference (2rev/s) so that the resulting data would be linearized about the system's steady-state operating point. Ideally, the frequency range of interest was 0 to 200hz, which is the Nyquist frequency for a

Table 1 - Two empirically derived system models for the open-loop zero-pole-gain transfer function of the test fixture.

<u>Low Order Model</u>			<u>High Order Model</u>		
Gain = 8,285			Gain = 10,278		
0-Zeros (Hz)	3-Poles (Hz)	Damping	2-Zeros (Hz)	5-Poles (Hz)	Damping
—	-19.4	1.000	$-8.67 \pm 76.20j$	-19.39	1.000
—	$-2.2 \pm 28.3j$	0.078	—	$-2.2 \pm 28.26j$	0.078
—	—	—	—	$-4.96 \pm 85.42j$	0.058

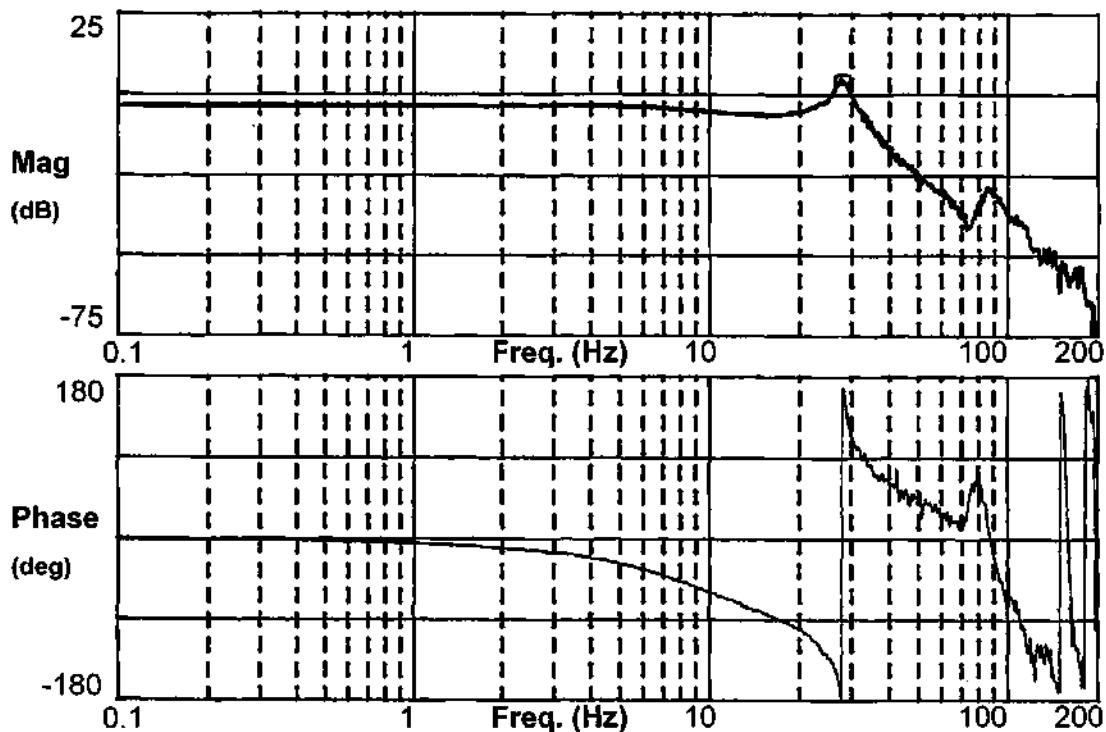


Figure 33 - Experimental frequency response (Bode) plot using a swept sine routine with a 0.3volt perturbation amplitude and a 3.6volt DC carrier voltage. This allowed the output of the fixture to oscillate about the desired steady-state velocity.

system sampled at 2.5msec. However, since the measurements displayed poor coherence above 100hz and since all significant disturbances were anticipated to be far below this, the actual frequency range considered was 0 to 100Hz.

A plot of the resulting frequency response data is given in Figure 33. From the data, we observe that the gain and phase remain relatively constant for frequencies below 5Hz. There is a significant resonance with a gain above 0dB near 28Hz and another one around 85Hz. The 28Hz mode is the flexible shaft's torsional resonance. The high frequency degradation of the measurements above 120Hz is especially apparent in the phase plot which starts to vary wildly.

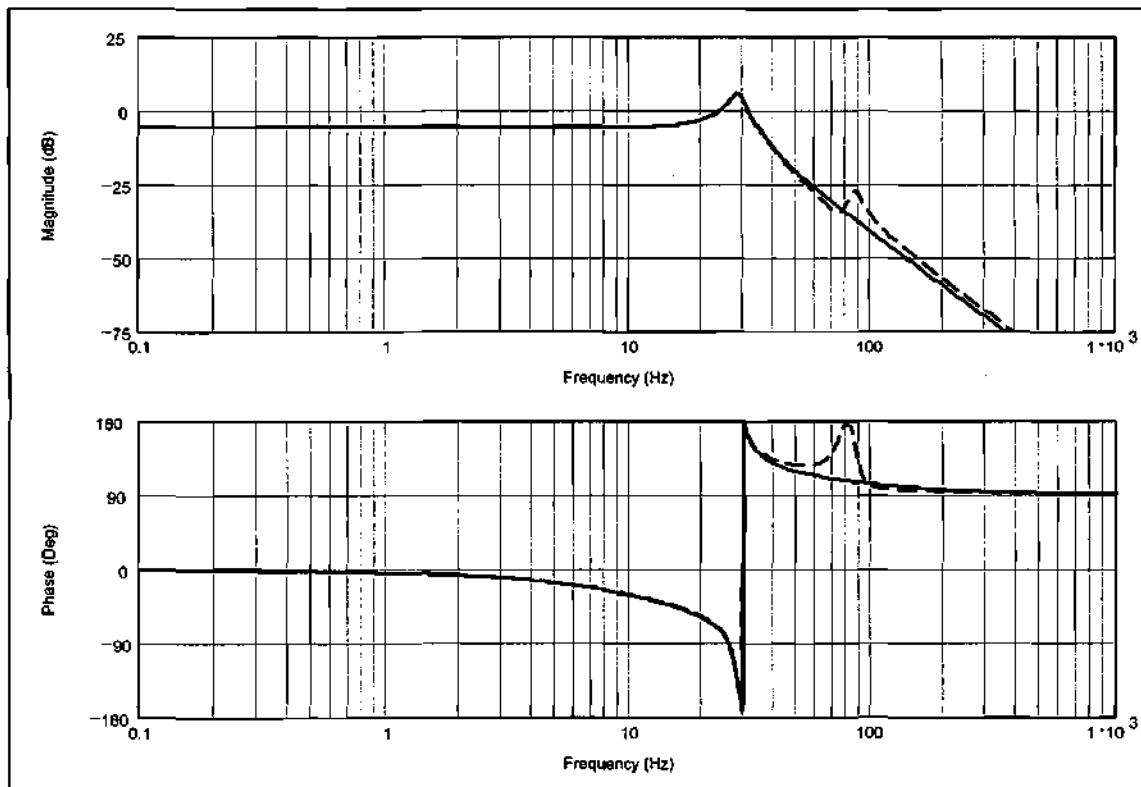


Figure 34 - Open-loop frequency response of two linear plant models. Both were derived from curve fits of the data from empirical frequency response tests performed on the test fixture. The lower order model (solid) has 3 poles and no zeros, while the higher order model (dashed) has 5 poles and 2 zeros.

Using the curve-fitting routine of the HP analyzer, the poles and zeros of the measured transfer function were estimated. After experimenting with different regression weighting parameters, two models, herein referred to as the low and high order models, were judged to be close approximations of the true system. The low order model had no zeros and 3 poles and the high order model had 2 zeros and 5 poles. Two systems were deemed necessary because a lower order model would produce a more stable feedback controller, while a higher order model would produce a better Q-filter design and more realistic simulation results. The zeros, poles, and

gains associated with each of these systems are summarized in Table 1. Frequency response curves for both of these systems are plotted together in Figure 34. A visual comparison between these curves and the empirical F/R curves of Figure 33 shows good correlation up to 100Hz.

### Disturbance Identification

In order to gain a qualitative understanding of the types of disturbances the test fixture is likely to encounter, the relationship between the mechanical components in the fixture was examined. This process involved a component-by-

Table 2 - Anticipated test fixture disturbance sources.

Item	Description	Rel.* Factor	Abs.** Freq.	Contribution***		
				Low	Med	Hi
Belt #1 Tooth Freq & 1x	Connects subsys #1 & #2; 1x freq on 1st line, tooth freq. on 2nd...	2.18 120	4.36 240	X X		
Belt #2 Tooth Freq & 1x	Connects subsys #2 & #3; 1x freq on 1st line, tooth freq. on 2nd...	1.00 60	2.0 120	X X		
Belt #3 Tooth Freq & 1x	Connects subsys #3 & #4; 1x freq on 1st line, tooth freq. on 2nd...	0.365 20	0.73 40	X		X
Subsys #4 Shaft Once around	Output shaft; Includes encoder, brake, low-cam, 20-tooth pulley, & 2 couplings.	1	2	X		
Subsys #3 Shaft Once around	Flex-Shaft subsystem	2	4			X
Subsys #2 Shaft Once around	Hi-cam subsystem	6	12	X		
Subsys #1 Shaft Once around	Drive motor subsystem	12	24	X		
Low-Cam 1x	Part of subsys #4; Dual lobe design	2	4			X
Hi-Cam 1x	Part of subsys #2; Dual lobe design	12	24			X
Drive Motor torque ripple	8 commutations/ rev (assumed) + 2 <sup>nd</sup> harmonic (16 cyc/rev)	96 192	192 384	X X		

\* Unitless speed factor relative to the once-around of the output shaft.

\*\* Absolute frequency in hertz, assuming a constant output shaft speed of 2rev/s (i.e., 2hz).

\*\*\* The anticipated significance of a disturbance's magnitude.

component assessment of potential disturbance sources, including an estimate of the significance of a perturbation's contribution and its steady-state frequency. For example, the high-cam assembly will rotate at a rate six times that of the output shaft (due to the 6:1 reduction), will have a disturbance frequency equal to twice its rotation rate (i.e.,  $2 \times 6 \times 2\text{Hz} = 12\text{Hz}$ ), and will likely contribute moderate to high torque perturbations. The results of this predictive analysis are given in Table 2.

Once it was established what disturbances *should* be present, an FFT was performed on the open loop system operating at the desired output of 2 revs/s to see what disturbances *were* present. The results are plotted in Figure 35. Based on Table 2, we expect to see a variety of perturbation at various frequencies, especially 4Hz. The FFT in Figure 35 confirms this. In addition, there are several large disturbances around 28Hz. Recalling that the F/R analysis revealed a strong resonance at this frequency, we conclude that the system is amplifying the disturbances in this region. This claim is bolstered by the tell-tale manner in which the base/floor of the FFT ascends prior to, and descends after the 28Hz frequency band. We wish to design a compensator that will minimize the effect of this and any other troublesome dynamics prior to applying RLC. It should be noted that for this and all subsequent tests, the high-cam actuator was deactivated because its contributions to the system's high-frequency disturbance content and non-linearities were judged to be unrealistically high.

Perturbations such as the low frequency timing belt disturbances, which were predicted in Table 2, are not evident in the spectral plot. The dominant disturbances all appear to be harmonics of the reference signal, 2Hz. As previously

indicated, a system with such attributes is a strong candidate for the application of repetitive learning control. Unfortunately, the magnitudes of the disturbances at the higher harmonics, say 20Hz and higher, are quite large relative to the lower frequencies. This can pose a problem; although digital RLC can theoretically attenuate all harmonics of the disturbance fundamental below the controller's Nyquist frequency, the effectiveness of the attenuation tends to decrease with increasing harmonic number. This will be addressed in a subsequent chapter.

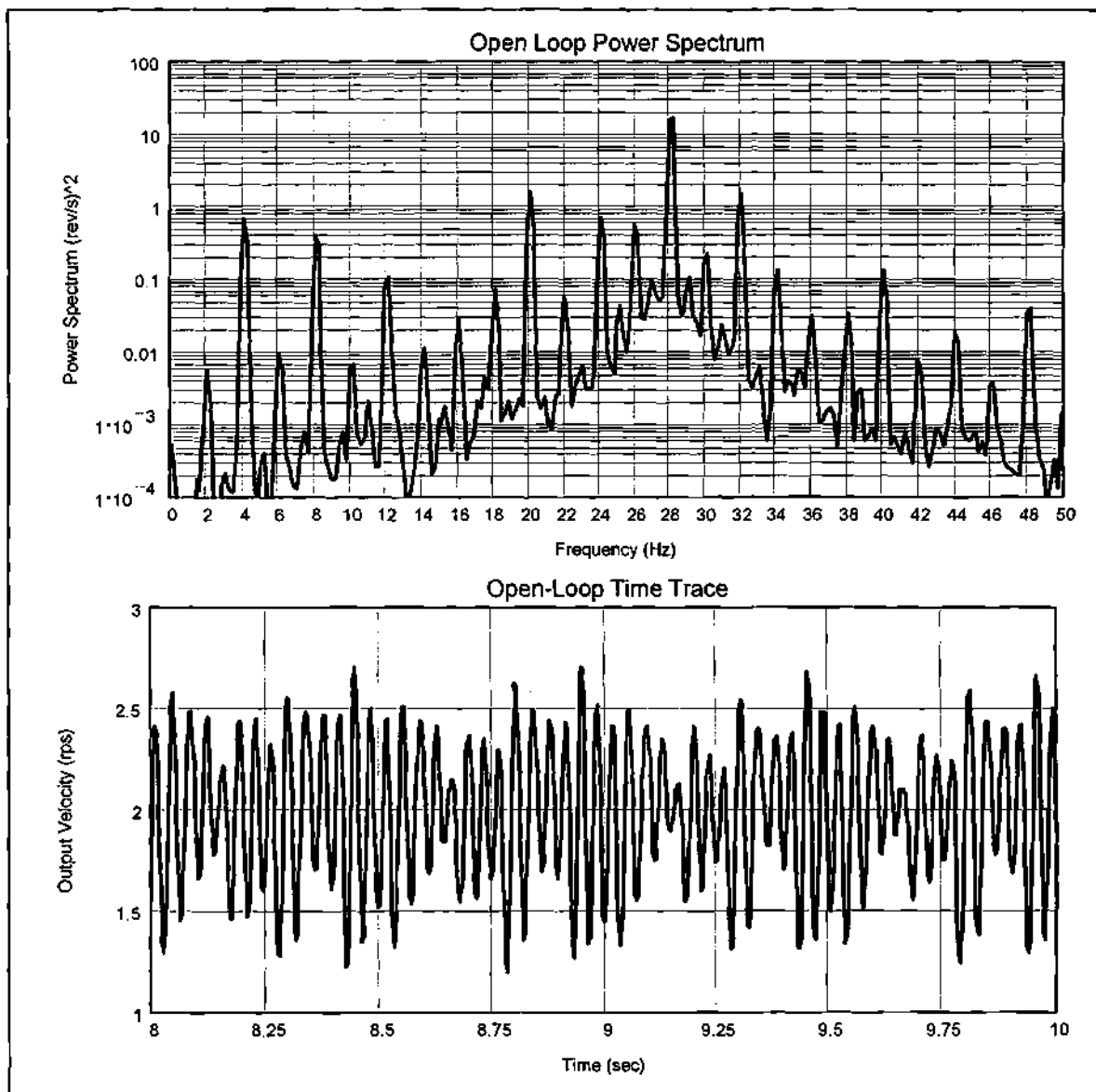


Figure 35 - Steady state time history and power spectral density for the open-loop system. Ten averages and a Hanning window were used in computing the FFT. Ref=2rps.

## CHAPTER VI

### CONTROLLER DESIGN

#### Simulation Model

In the preceding chapter, the dynamics of the test fixture were studied and found to be well approximated by either of two linear models that differ only in their order. The high order model (2 zeros, 5 poles) was judged to be best suited for simulation studies since it was theoretically a closer representation of the actual system. The higher order modes, however, had a greater degree of uncertainty associated with their measurement. Therefore, the lower order model (no zeros and 3 poles) was used for designing the controllers that would actually be implemented on the test fixture.

#### Closed-Loop Polynomial Control

Figure 36 shows the frequency spectrum for the test fixture's steady-state output velocity. Although the fixture is stable, the resonance at 28Hz and the apparent amplification of the local disturbances indicate that the dynamic characteristics of the open loop system should be improved a bit prior to applying repetitive learning control. Polynomial compensation design was the technique chosen to accomplish this because it allowed the desired closed-loop poles to be specified directly. As was previously mentioned, the low order model was used to establish

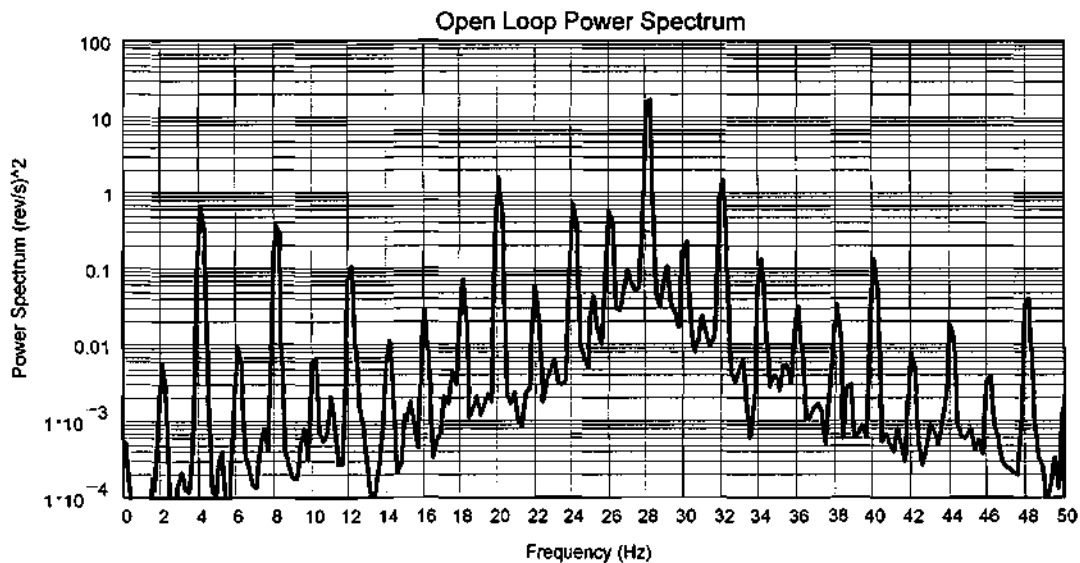


Figure 36 - Power spectrum of the open-loop plant's steady-state output velocity

which poles should be moved. Then, the resulting controller was applied to the high order model for simulations and the test fixture for empirical studies.

Figure 38 shows the stable pole/zero locations for the high order model in the  $z$ -plane. Examination of the root locations revealed a pair of lightly damped poles (i.e., near the unit circle) corresponding to the 28Hz mode in both the high and low order models. It was decided that these poles be moved along the line of constant natural frequency so that the effective damping ratio would be increased from 0.078

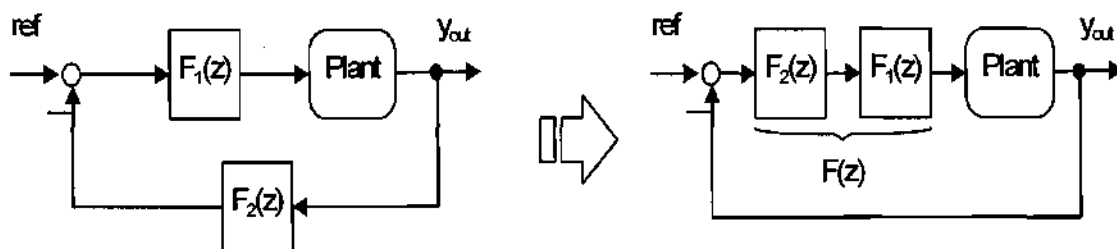


Figure 37 - Alternate arrangement of feedforward and feedback compensators.

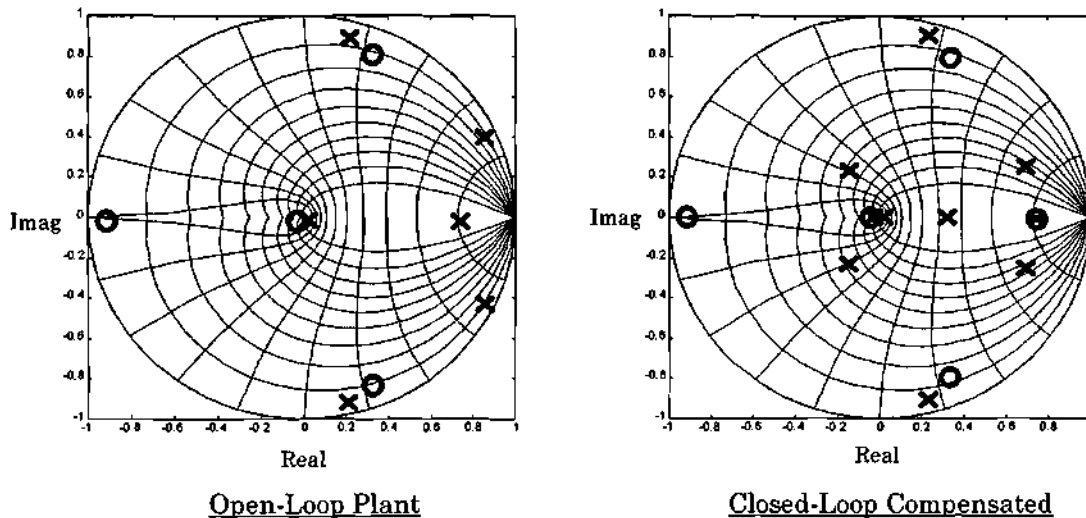


Figure 38 - Stable Z-Plane root location plots for the discrete open-loop plant and the discrete closed-loop compensated plant. Note that there are three unstable zeros at  $-20$ ,  $+5$ , and  $+10^{11}$  for the closed loop system and one unstable zero at  $-20$  for the open system, which are not visible. The closed-loop plot shows 2 pole-zero "near" cancellations and the relocation of the two poles corresponding to the 28Hz mode. This conjugate pair was moved to a region of increased damping.

to [at least] 0.707 without altering the natural frequency. This change is evident in the closed loop root plot. Note that the other pair of poles near the unit circle correspond to the 85Hz mode and were only present in the high order model. Therefore, they were not altered in the compensation design process.

The feedforward and feedback compensators resulting from the polynomial design,  $F_1(z)$  and  $F_2(z)$ , respectively, were arranged in an alternate architecture as shown in Figure 37. Therefore, the feedback compensation became unity and the feedforward compensation became the product of  $F_1(z)$  and  $F_2(z)$ . This architecture was preferred because the feedback compensator,  $F_2(z)$ , had high gain at high frequencies. Since the plant disturbances were modeled at the output and had significant high frequency content, putting  $F_2(z)$  in the feedback loop amplified their effect,

resulting in higher feedback errors. This made the job of the repetitive controller much more difficult since it would have to modify the reference input even more in the high frequency range to compensate.

The frequency response of the resulting feedforward controller,  $F(z)$ , is plotted in Figure 39. Although this controller also has high gain in the upper frequency bands, this gain is applied to the error signal and not the feedback signal,  $y_{out}$ . The frequency response of the high order model with the closed loop compensation applied is given in Figure 40. As expected, the resonance at 28Hz (176rad/s) is at

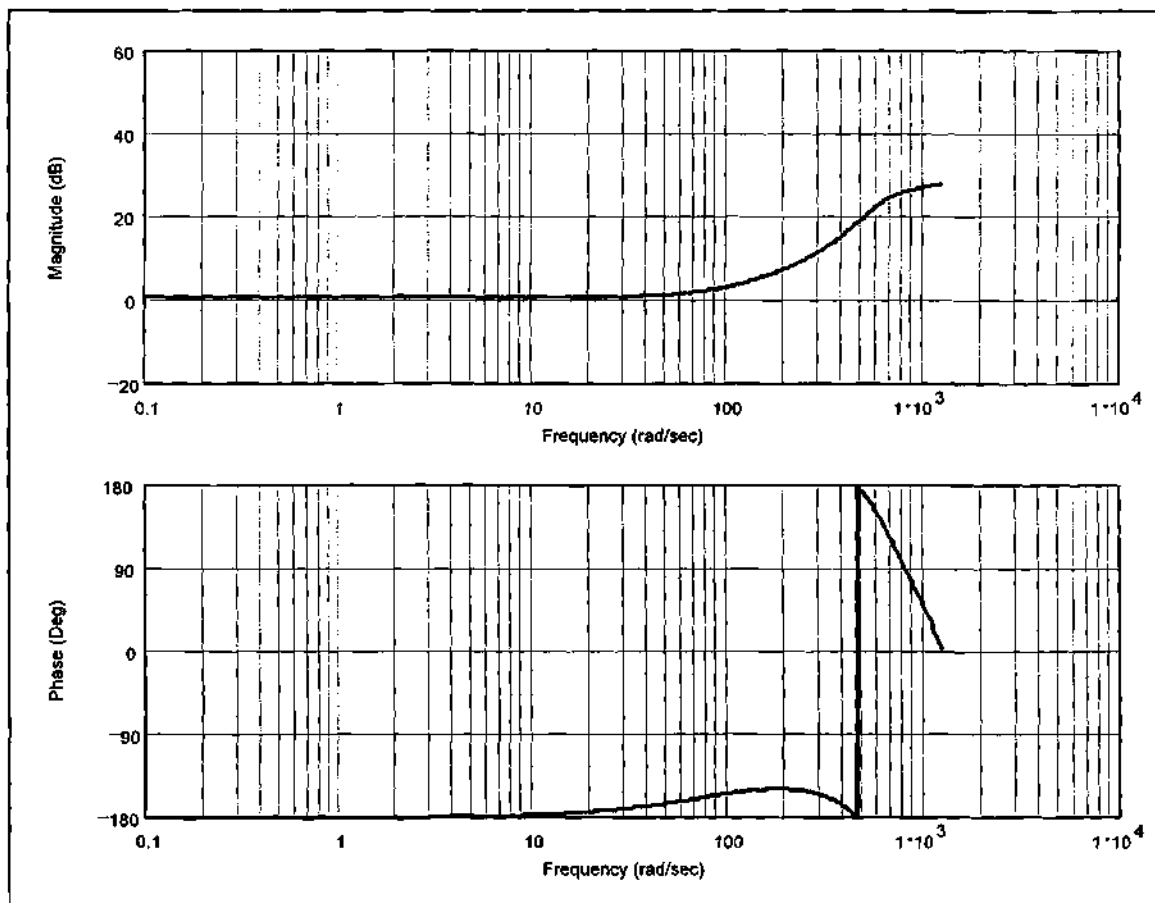


Figure 39 - Frequency response of the digital feedforward plant compensator ( $T_s = 2.5\text{msec}$ ), from 1 rad/s up to the Nyquist frequency (1257rad/s).

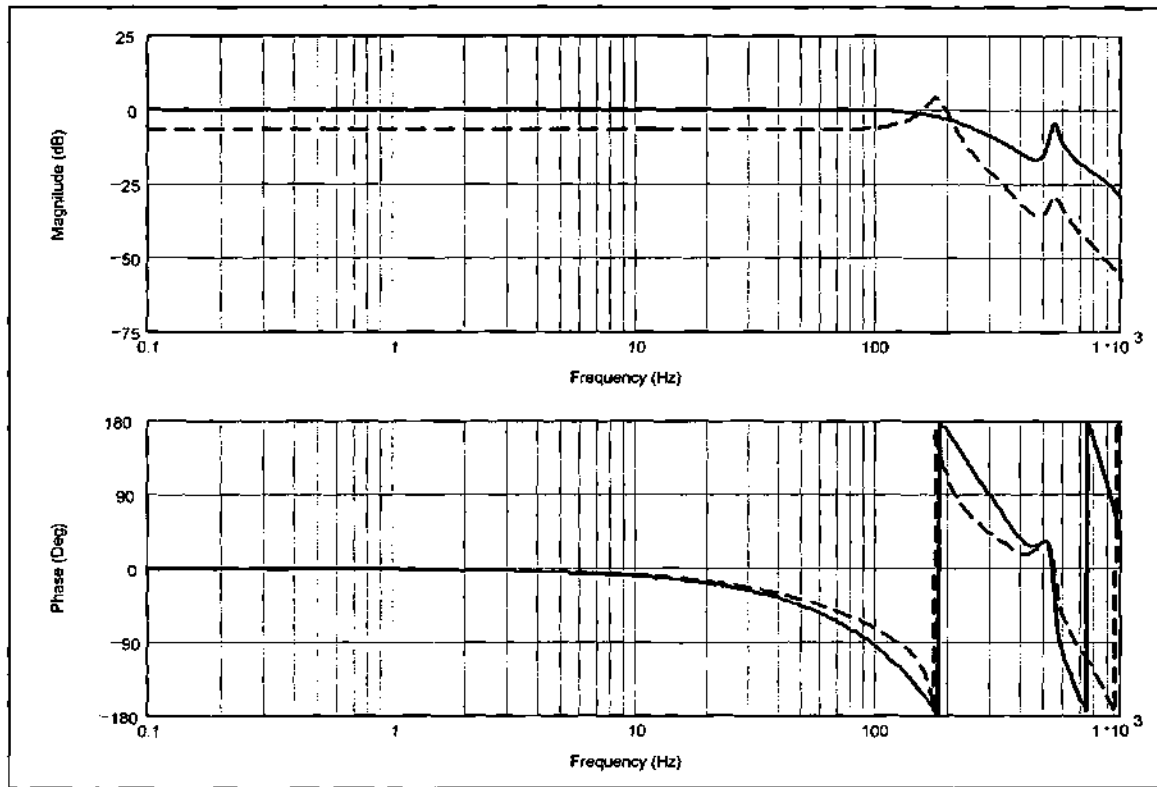


Figure 40 - Frequency response plot of the open loop (dashed) and compensated closed loop system,  $H(z)$  (solid). Note that the resonance at 28Hz (176rad/s) is attenuated and the system gain is improved overall. No attempt was made to alter the mode at 534 rad/s, because it was not present in the low order model.

tenuated and the system gain is improved overall. Since no attempt was made to alter the resonance at 85Hz (534 rad/s), the effect of this mode is still present in the closed-loop system.

### Polynomial plus Integral Control

In order to achieve increased steady-state and low frequency performance, the polynomial feedforward controller developed in the preceding section was modified with the addition of integral action. The resulting controller had relatively

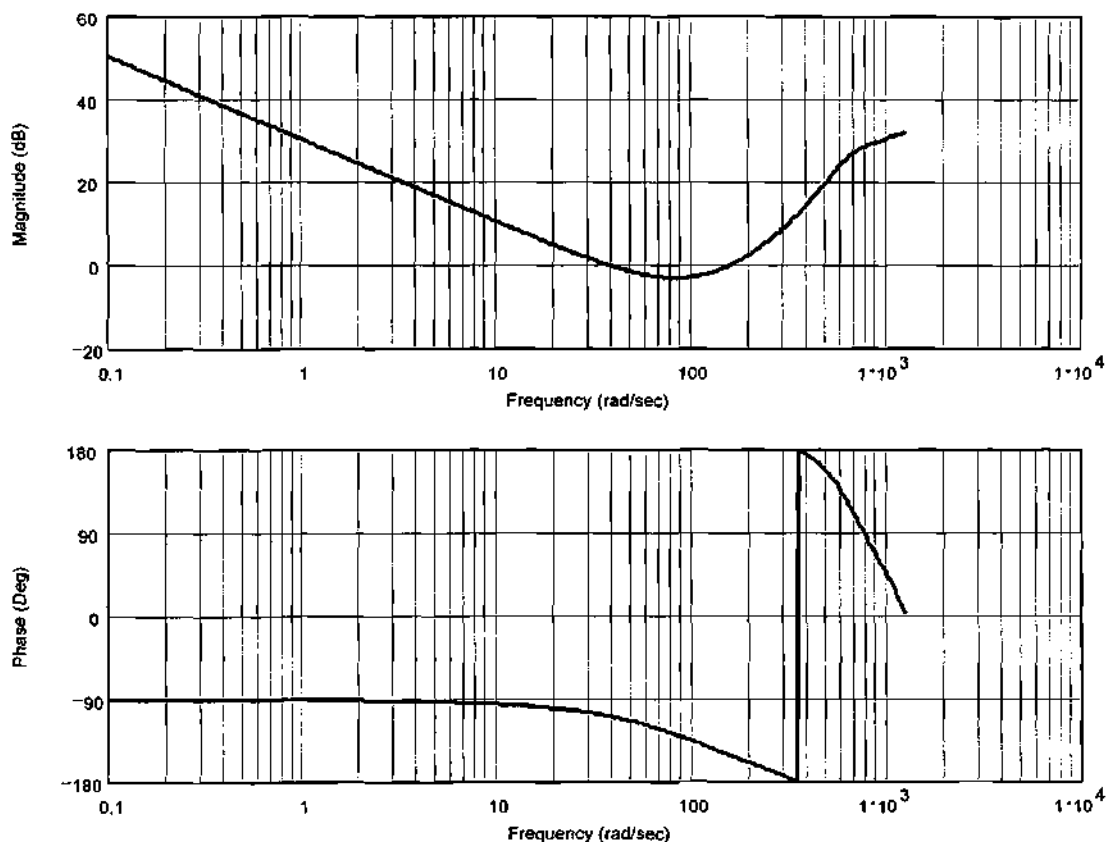


Figure 41 - Frequency response of the digital feedforward plant compensator ( $T_s = 2.5\text{msec}$ ), from 1 rad/s up to the Nyquist frequency (1257rad/s).

large coefficients; e.g., the largest coefficient for controller with integral action was roughly 600 times the largest coefficient for the controller without integral action. Therefore, this controller will be implemented (both with and without RLC) in simulation only. This is because the large gains of the controller coefficients would cause instabilities in the actual test fixture due to unmodeled dynamics and nonlinearities. A frequency response of the polynomial controller with integral action is provided in Figure 41.

### Q-Filter Design

The stability criteria presented in Chapter II showed that, for stable RLC operation, the closed loop plant  $H(z)$  must be filtered such that the total phase shift is less than  $\pm 90$  degrees. If this requirement is fulfilled by the  $H(z)$  alone, then no filtering is necessary. However, as the F/R curves in Figure 40 show, the phase shift exceeds 90 degrees and thus, filtering is necessary. Designating this filter by  $Q(z)$  in the z-domain, we seek to develop a filter that will ideally have a phase shift opposite to that of  $H(z)$  so as to cancel it. The simplest way to achieve this is to invert the plant; that is:

$$Q(z) \equiv \frac{1}{H(z)} \quad (94)$$

However, this alone may result in one or both of the following problems:

1. If  $H(z)$  is non-minimum phase<sup>3</sup>, then inverting it puts the unstable zeros in the denominator, thereby making the resulting filter unstable.
2. If the relative degree<sup>4</sup> of  $H(z)$  is not zero, then it will be positive, meaning that there are more poles than zeros. Inverting it results in a transfer function that has more zeros than poles; i.e., a non-causal system.

To account for the first problem, a technique for zero phase error tracking (or ZPET) developed by Tomizuka et al. (26) is employed, which essentially neglects the unstable zeros of  $H(z)$  in such a way that the resulting system is minimum phase, while the original phase characteristics are preserved. A seemingly undesirable by-

---

<sup>3</sup> A non-minimum phase system has at least one unstable zero; i.e., outside of the unit circle.

<sup>4</sup> The relative degree of a transfer function equals the number of poles "minus" the number zeros.

product of this procedure is that the relative degree of the new system is increased by an amount equal to the original number of unstable zeros. Therefore, even if the relative degree of the original system was zero, the new system will have a positive relative degree so that inversion will necessarily result in a non-causal system. This leads to the second stated problem.

The schematic for the RLC block in Figure 42 was originally given in Chapter I and is repeated here for convenience. If  $Q(z)$  represents the filter formed by inverting and stabilizing the closed loop plant  $H(z)$ , then by setting the delay value  $g$  equal to  $-1 \times$  (relative degree), the realizable (i.e., causal) filter  $Q^*(z)$  is formed. Note that this delay is canceled by the positive shift in  $R^*(z)$ . This is possible because the order and relative degree of the unshifted controller  $R(z)$  are both equal to  $NL$ , which is usually much larger than  $g$ . Therefore, the positive shift  $g$  is easily "absorbed" so that  $R^*(z)$  remains causal and realizable. Frequency response plots for  $Q(z)$ ,  $H(z)$ , and the product of these transfer functions, i.e.,  $QH(z)$  are given in

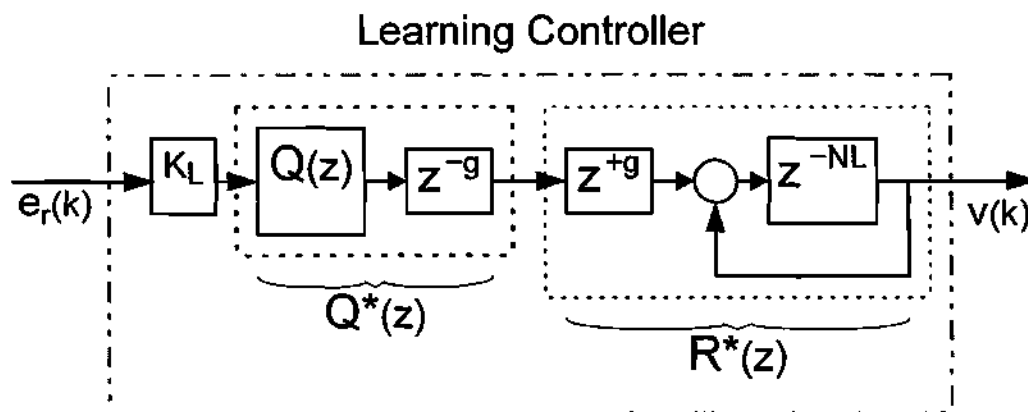


Figure 42 - Learning controller block diagram.  $K_L$ ,  $Q^*(z)$ , and  $R^*(z)$  represent the learning gain, "realizable" Q-filter, and the companion repetitive controller, respectively.

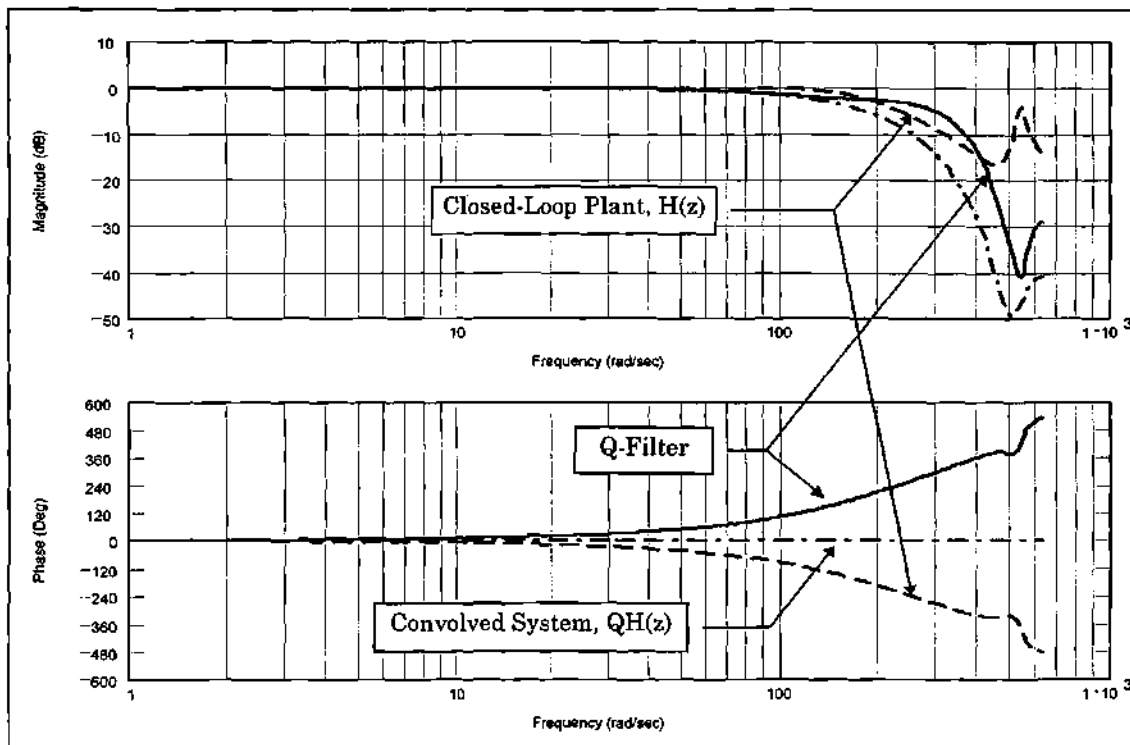


Figure 43 - Frequency response plots for the closed-loop plant  $H(z)$  (dashed) and the non-causal digital Q-filter (solid), from 1Hz up to the filter's Nyquist frequency (628rad/s). Convolving the plant and Q-filter results in a system with virtually zero phase shift and low pass characteristics (dash-dot).

Figure 43. Now that an effective stabilizing filter  $Q(z)$  has been found, we proceed with the development of the repetitive controllers.

### Repetitive Controller

Proper design of a repetitive controller requires prior knowledge of the task period and the system disturbances. In particular, the frequencies and source of the significant disturbances must be known; e.g., are they strict functions of time or are they related to the state of some system state(s), or both? A prudent approach to

system identification is comprised of essentially two steps: (1) analyze the system and component functionality to develop an understanding of the type of disturbances likely to be present and their predicted effect on system performance and (2) perform empirical tests to verify and refine these predictions. The results of this process were discussed and tabularized in the test fixture chapter.

Quantifying the nature of the disturbances in the experimental apparatus was somewhat challenging. It is probably accurate to say that virtually all of the significant disturbances are functions of the angular positions (states) of the various shafts, and not strict functions of time. The problem occurs, however, in measuring what those states are. Recall that the only output sensor is on the system's output shaft. While the position and velocity of these shafts are related to output shaft by a set of known gear reductions, compliances within the system make these relationships non-constant. Therefore, even though a component like the high frequency cam is clearly a function of its own shaft position, it is difficult to infer precisely the instantaneous value of this position from the output shaft's position. This problem could have been reduced or eliminated by the addition of more sensors (e.g., an encoder on each shaft, or at least on the motor shaft). However, resource limitations negated this option.

In what follows, three different RLC architectures will be designed for the experimental test fixture subjected to the closed-loop compensation designed earlier in this chapter. For all of the architectures, the plant's sample rate was  $T_s=2.5\text{msec}$  and the repetitive controller sampled at  $T_c=5.0\text{msec}$ . Thus, the concepts of multi-rate RLC introduced in a previous chapter were implemented, including first order

hold up-sampling and linearly weighted down-sampling. A multi-rate architecture allowed the plant compensation to have a relatively high band-width, while producing a repetitive controller that was more stable (lower order) and memory efficient than if it were also sampling at the higher rate.

The steady-state response of the closed-loop test fixture is depicted in Figure 44. Comparing this frequency spectrum with that of the open-loop system (Figure 36) shows that the mode at 28Hz was successfully attenuated. In the figure, it is evident that all disturbances above a certain threshold, say  $0.01\text{rev}^2/\text{s}^2$ , are harmonics of the reference output velocity,  $2\text{rev/s}$ . While this makes the system a good candidate for RLC, the relatively large magnitude of the higher frequencies is expected to pose an attenuation problem.

## Internal Model RLC

### Single Controller

Since the frequency response of the system in Figure 44 suggests that all disturbances are harmonics of 2Hz, a single repetitive controller is designed for this frequency. By the previously stated learning cycle formula,  $NL = \frac{1}{T_c \cdot f_0}$ , a 5msec sampling rate and 2Hz fundamental result in a learning cycle  $NL = 100$  samples. Therefore, the unfiltered transfer function  $R^*(z)$  of a single repetitive controller applied to the experimental test fixture is

$$R^*(z) = \frac{z^g}{z^{100} - 1}$$

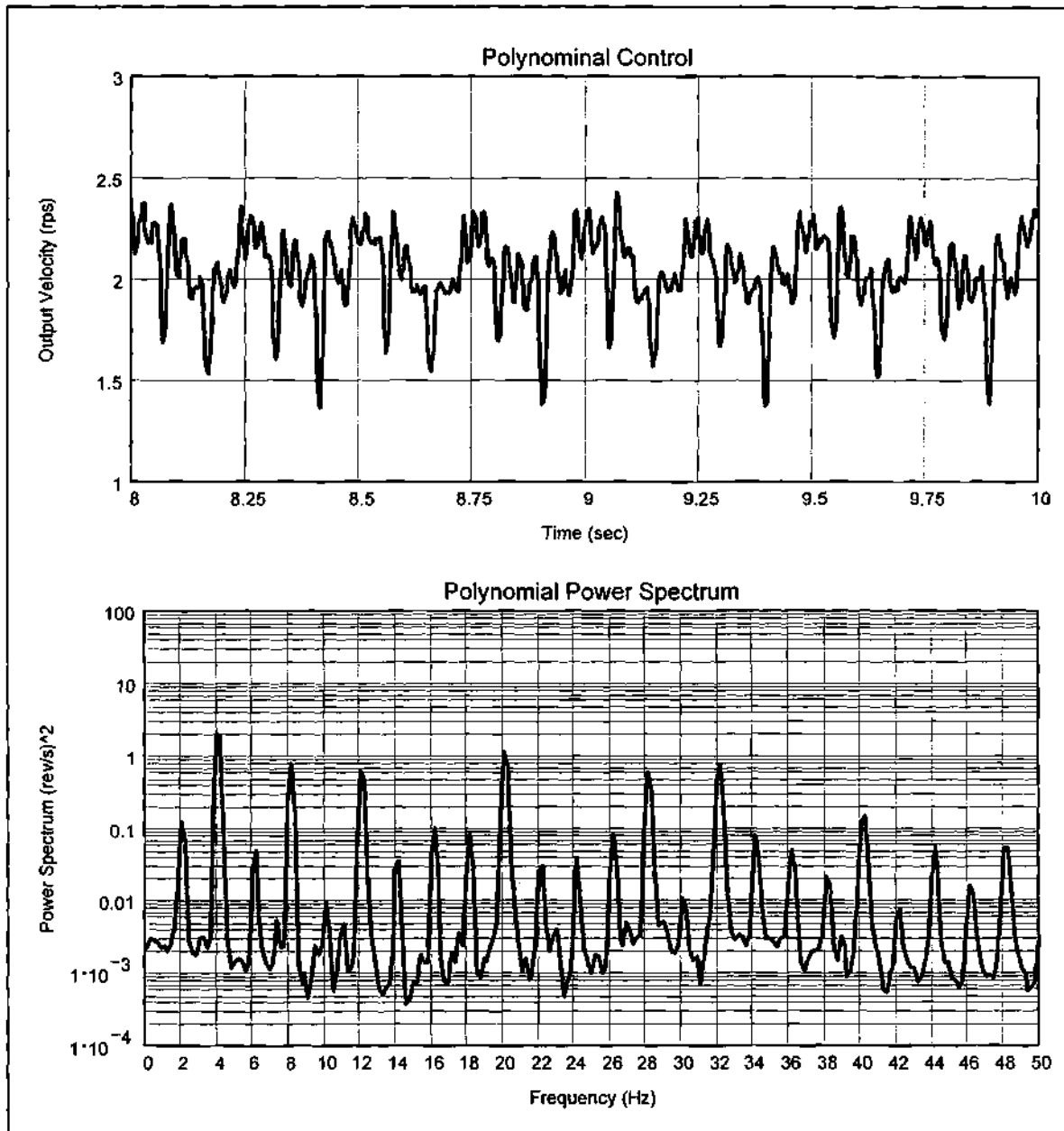


Figure 44 - Steady state time history and power spectral density for the system under closed-loop polynomial control.

### Dual Controller

As the data in the results chapter show, when a single learning controller was applied to the system, the 0.73Hz belt mode became evident, even though it did not appear in the frequency plots of either the open-loop system or the closed loop system. The increase in this disturbance is probably due to the action of the repetitive controller. Even though the magnitude of this perturbation remained small, relative to the other disturbances in the system, its existence provided a good opportunity to implement dual repetitive controllers. Note that this scenario was illustrated in the section on parallel controllers in Chapter 3.

Since the largest common fundamental frequency between the belt mode and the shaft's first mode (0.73Hz and 2Hz, respectively) was 0.182, the corresponding learning cycle length would be 1099 samples. This prohibitively high value would result in slow convergence and would require large amounts of memory storage. If instead, an additional controller is designed with 0.73Hz as its fundamental, then the learning cycle of this learning controller would only be 274, and the controller would have the following transfer function

$$R_2^*(z) = \frac{z^8}{z^{274} - 1}$$

The learning gain used was 0.25. See Chapter 3 for a schematic illustration and stability proof of this arrangement.

## External Model RLC

### Single Controller

The chapter on RLC formulation showed that internal and external model based repetitive controllers are functionally identical if all of the harmonics of the fundamental (from 1 up to  $NL/2$ ) are included in the external model. However, because of computational considerations, only a subset of these harmonics are implemented. Based on the closed-loop frequency spectra, the modes chosen for attenuation by the external model were 2, 4, 8, 12, 18, 20, 32, and 40 Hertz. For  $NL=100$ , these modes were the 1<sup>st</sup>, 2<sup>nd</sup>, 4<sup>th</sup>, 6<sup>th</sup>, 9<sup>th</sup>, 10<sup>th</sup>, 16<sup>th</sup>, and 20<sup>th</sup> harmonics, respectively. While there were a few candidates that should have been included in this set (e.g., 6Hz), processing limitations required that the number of “active” modes be kept as small as practical.

### Dual Controller

In a manner similar to internal model controller design above, a second external model repetitive controller was also added to attenuate the belt mode at 0.73Hz. With  $NL2=274$ , only the 1<sup>st</sup> and 2<sup>nd</sup> harmonics (i.e., 0.73Hz and 1.46Hz) were used.

## Hybrid RLC

Both the internal and external model repetitive controllers attenuate the errors of periodic disturbances, but they each differ in the type of perturbation they attenuate best. Internal model controllers inherently assume (see Chapter 3) that

the disturbance frequencies are strict functions of time and do not vary. [Adaptive] external model repetitive controllers on the other hand, assume that the disturbance is directly related to the instantaneous state of some component (preferably the one being measured). Hence, the performance achieved by a particular system under RLC is highly dependent on the mechanism behind the significant disturbances present.

Preliminary tests on the test fixture revealed that some of the disturbances were both functions of time and shaft position. This relationship seemed particularly complex for some of the higher frequencies. For example, a phenomenon that we will call "harmonic splitting" was observed during real-time FFT measurements. This occurred during steady-state operation when the [internal model] repetitive controller was activated. Initially, all of the spikes in frequency spectrum - which were the disturbance harmonics - decreased in magnitude; however, in a few seconds, some stopped decreasing and literally split into two spikes (one slightly higher and one slightly lower in frequency than the parent harmonic). These new spikes then increased somewhat in magnitude. Apparently, the repetitive controller, in an attempt to attenuate these particular harmonics, actually caused some of them to split into two new disturbance frequencies.

Since the disturbances consisted of more than one mechanism, a hybrid repetitive controller was formulated using one internal and two adaptive external model controllers. This setup is illustrated in Figure 45. The hybrid controller is contained within the dashed block. The advantage to having both an internal and an external model controller tuned to some of the same frequencies is as follows: the

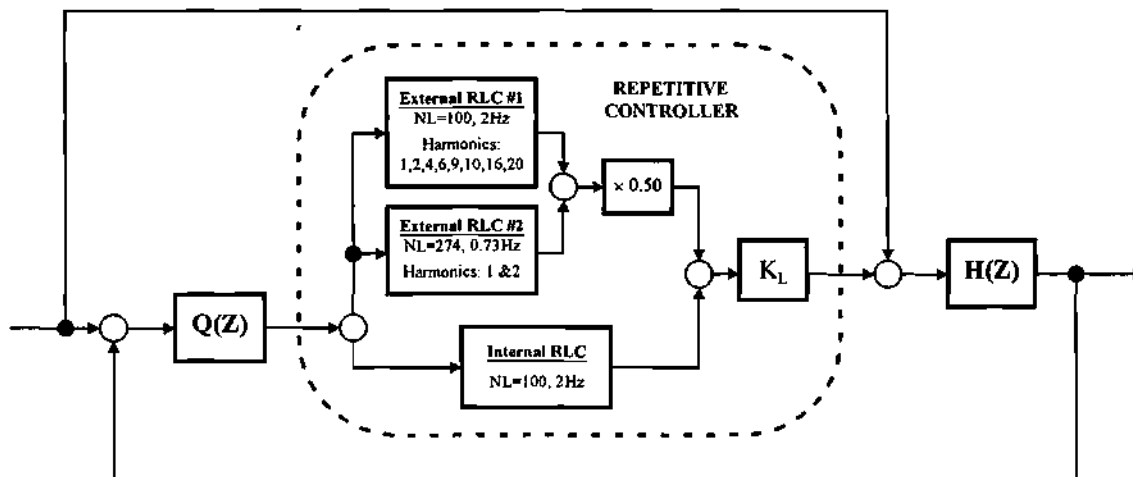


Figure 45 - Hybrid repetitive learning controller composed of one (1) internal model controller and two (2) adaptive external model controllers

internal model places high gains in the forward loop at fixed frequencies corresponding to the modes of the controller. Simultaneously, the adaptive external model controller places moving modes at key common harmonics. In this way, those frequencies that drift slightly from their expected value (due to output speed fluctuations and perturbations) are tracked and returned to this value.

## CHAPTER VII

### RESULTS

The results obtained during this effort for both the simulation studies and the empirical tests are now presented. Comments are included at the end of each section and as figure labels. The organization of the data is as follows:

#### I. Simulation Results

##### A. Polynomial Closed-Loop Compensation

1. Repetitive Control with Time Dependent Disturbances
2. Repetitive Control with Position Dependent Disturbances
  - a) Low Amplitude Disturbances
  - b) High (Realistic) Amplitude Disturbances

##### B. Polynomial Control, Integral Action (PCIA)

1. Repetitive Control with Time Dependent Disturbances
2. Repetitive Control with Position Dependent Disturbances
  - a) Low Amplitude Disturbances
  - b) High (Realistic) Amplitude Disturbances

Comments

#### II. Empirical Results

##### A. Steady-State Response

1. Open-Loop Plant: Time Trace and Frequency Spectrum

2. Closed-Loop Polynomial Control: Time Trace and Frequency Spectrum
  3. Frequency Spectrum Comparisons
    - a) Open-Loop vs. Polynomial
    - b) Polynomial vs. Internal Model RLC
    - c) Repetitive Control: Internal, External, & Hybrid
  4. Steady-State Output: Open-loop, Closed-Loop, & Hybrid RLC
- B. Transient Response: Hybrid Repetitive Control

Comments

### Simulation Results

The plant and controller models developed in Chapter VI were simulated with periodic output disturbances entering as shown in Figure 46. Two different disturbance models were used: a strictly time depend set and an angular position dependent set. Block diagrams for these disturbance generators are provided in Figure 47. Both models form the total disturbance by summing a series of sine functions, each representing a harmonic of the fundamental perturbation. For the

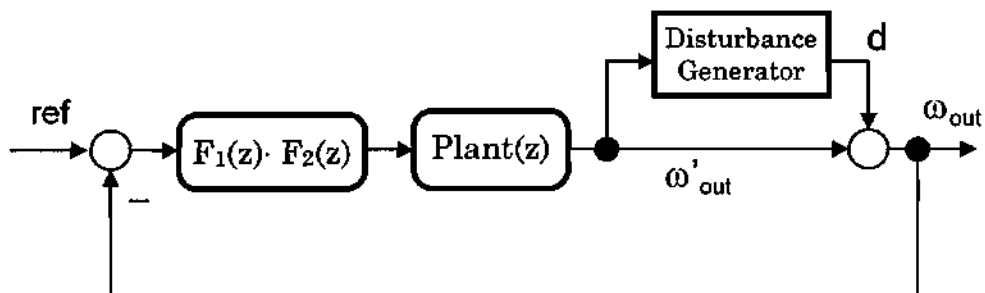


Figure 46 - Schematic illustration of the output disturbance generator and the injection point of the resulting perturbations.

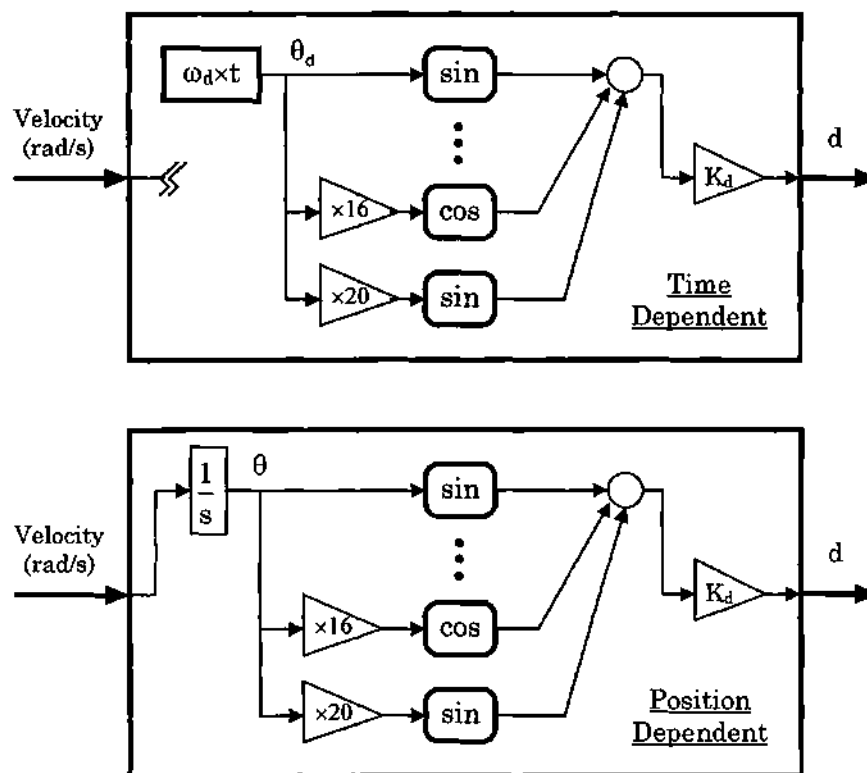


Figure 47 - The two disturbance generator models: (a) strictly time dependent and (b) angular position dependent. Seven individual harmonics of the fundamental were assumed: 1x, 2x, 4x, 6x, 10x, 16x, & 20x. Values for the combined disturbance gain  $K_d$  ranged from zero (no disturbances) to  $0.3/7=0.04$  rev/s.

purposes of simulation, seven (7) harmonics, between 1x and 20x, were assumed. The summation of these was scaled by a gain  $K_d$  before being added to the unperturbed velocity output. Values for  $K_d$  ranged from zero (no disturbance) to 0.04rev/s. A gain of approximately 0.04rev/s produced open-loop output velocity fluctuations that were closest in magnitude to the actual test fixture. Hence, the combined disturbance resulting from this gain is assumed to be a close approximation of the actual perturbations in the test fixture.

### A. Polynomial Closed-Loop Compensation

#### STEP RESPONSE

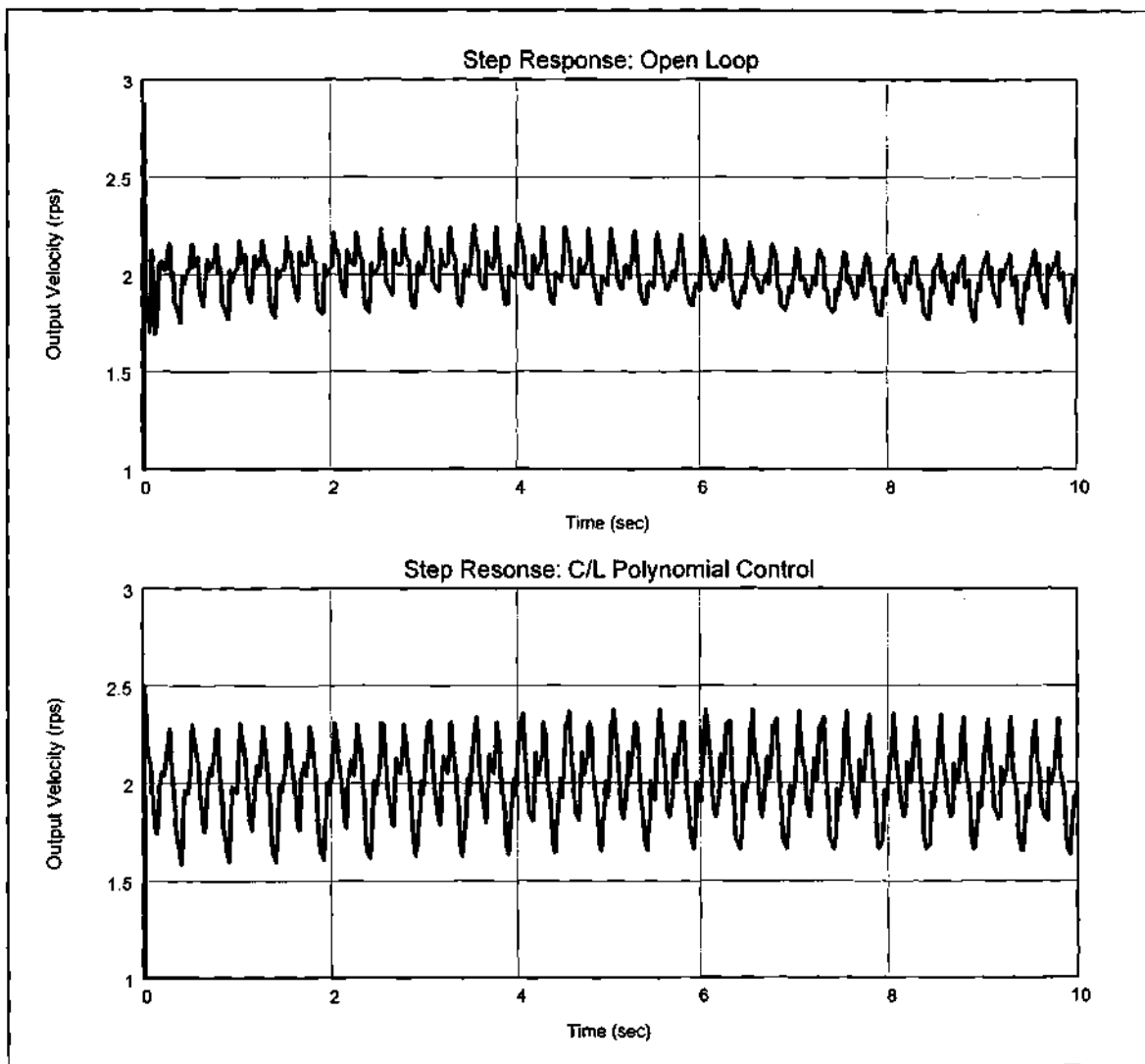


Figure 48 - Step response curves: open-loop and closed-loop polynomial control. Note that the polynomial appears to amplify the amplitudes of the high-frequency perturbations, while attenuating the low frequency. There appears to be a low frequency oscillatory drift in both cases. Integral action eliminated this.

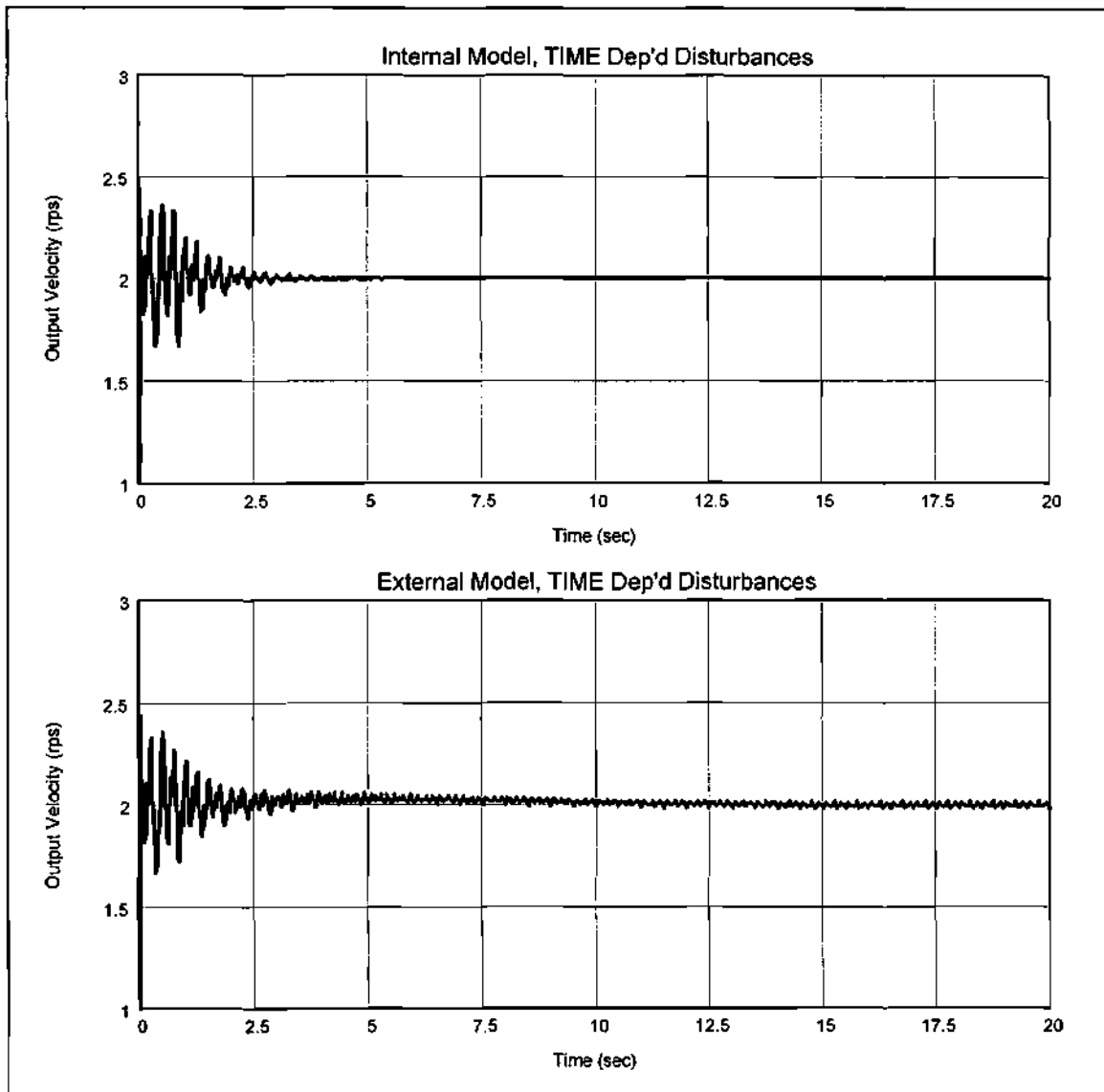
A-1. RLC: Time Dependent Disturbances

Figure 49 - Transient response, polynomial compensation: Internal and external model RLC assuming periodic disturbances that are strictly functions of time. The high (realistic) disturbance amplitudes were used. Both repetitive controllers worked well. Since the internal model assumes that the disturbances are functions of time, it converges somewhat faster than the external model controller.

## A-2. RLC: Position Dependent Disturbances

### a) Low-Amplitude Disturbances

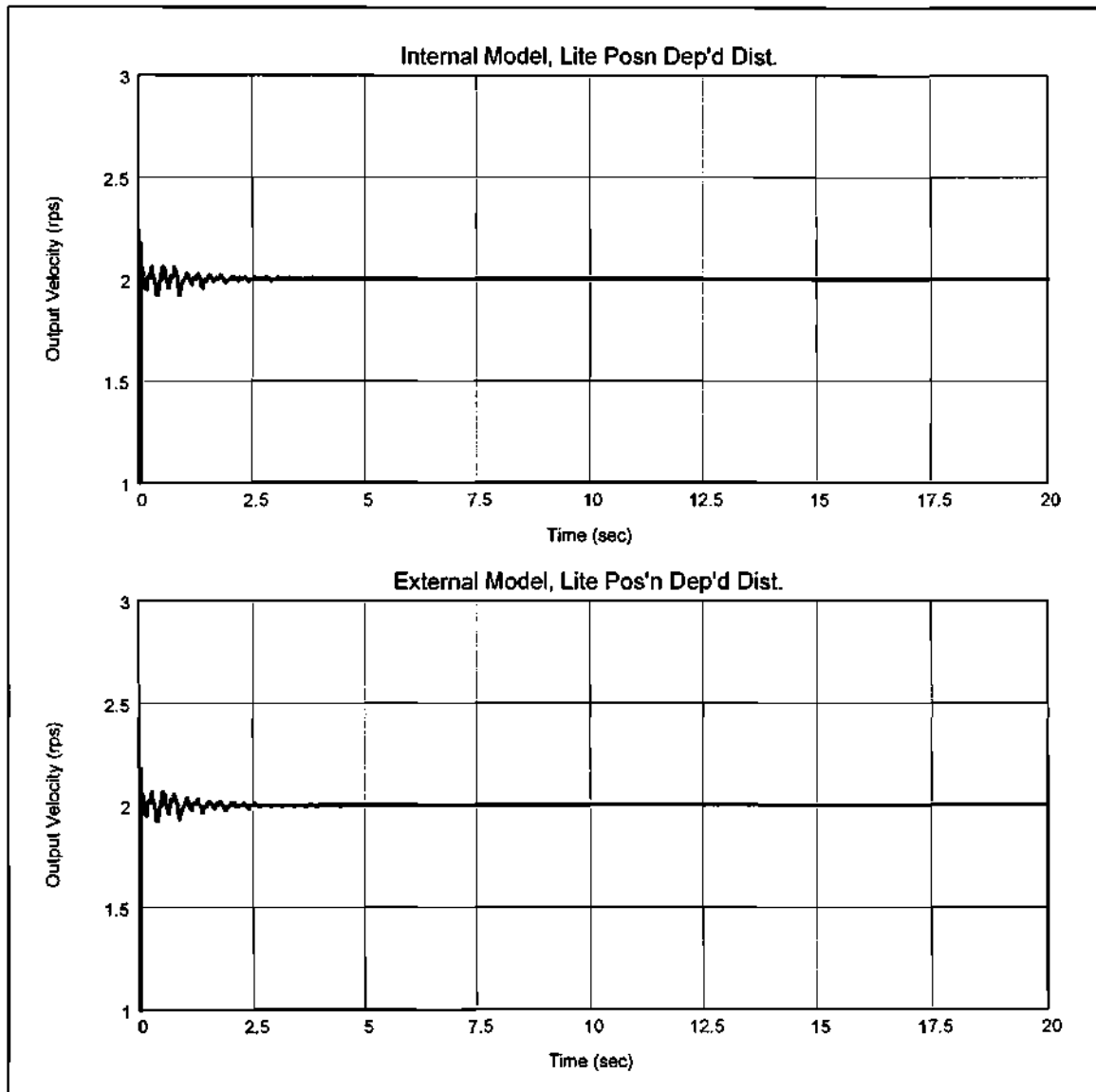


Figure 50 - Transient response, polynomial compensation, unrealistically low disturbance amplitudes (20% of realistic values): Internal and external model RLC assuming periodic disturbances that are functions of angular position. This test serves to verify the presence of a disturbance threshold below which repetitive control is guaranteed to work well. For these low amplitude, state-dependent disturbances, both controller forms converged quickly and completely. However, this did not remain true when the disturbance gain was increased to a more realistic value, as evident in the next diagram.

## b) Realistic (High-Amplitude) Disturbances

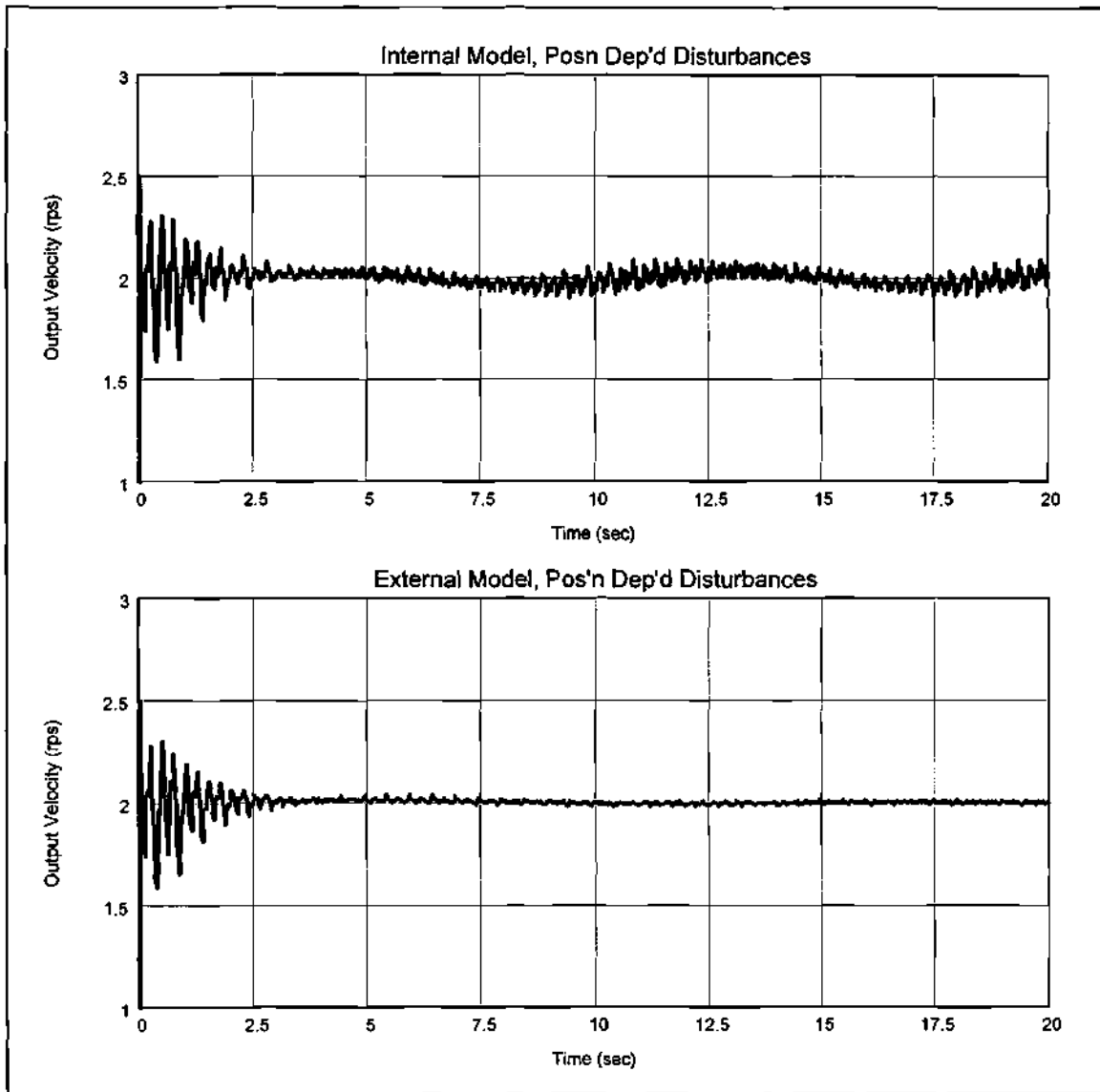


Figure 51 - Transient response, polynomial compensation, realistic disturbance amplitudes: Internal and external model RLC assuming periodic disturbances that are functions of angular position. Clearly, the threshold for asymptotic stability has been crossed in the case of the internal model controller. There is both a low-frequency oscillation and a pulsation in output velocity. The external model controller, however, is more robust and effectively attenuates the errors.

### B. Polynomial Compensation with Integral Action (PCIA)

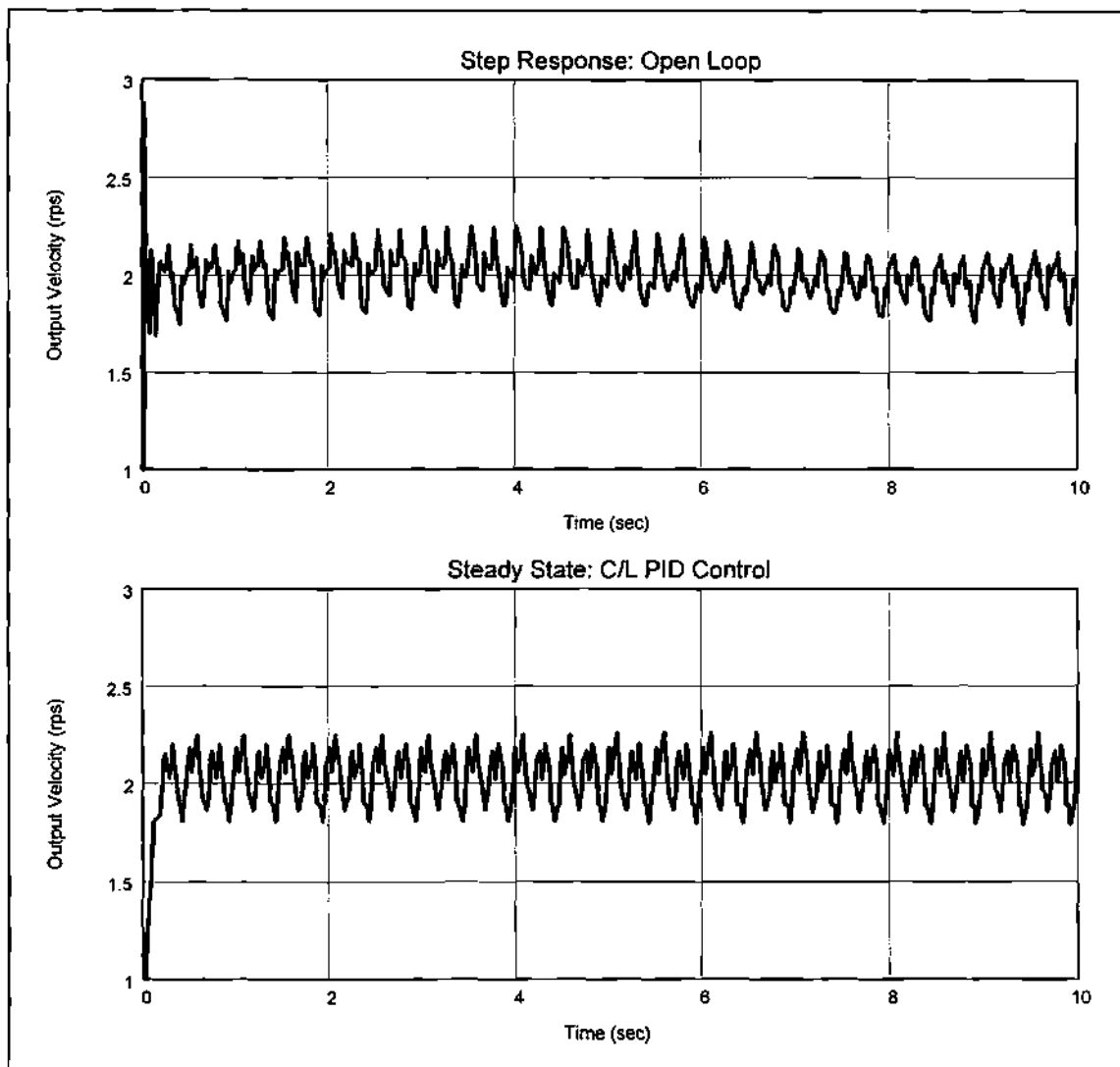


Figure 52 - Step response curves: open-loop and closed-loop polynomial w/ PID. The integral action is apparent by the improved steady-state tracking. There is also an improvement in the AC error amplitude over polynomial control alone.

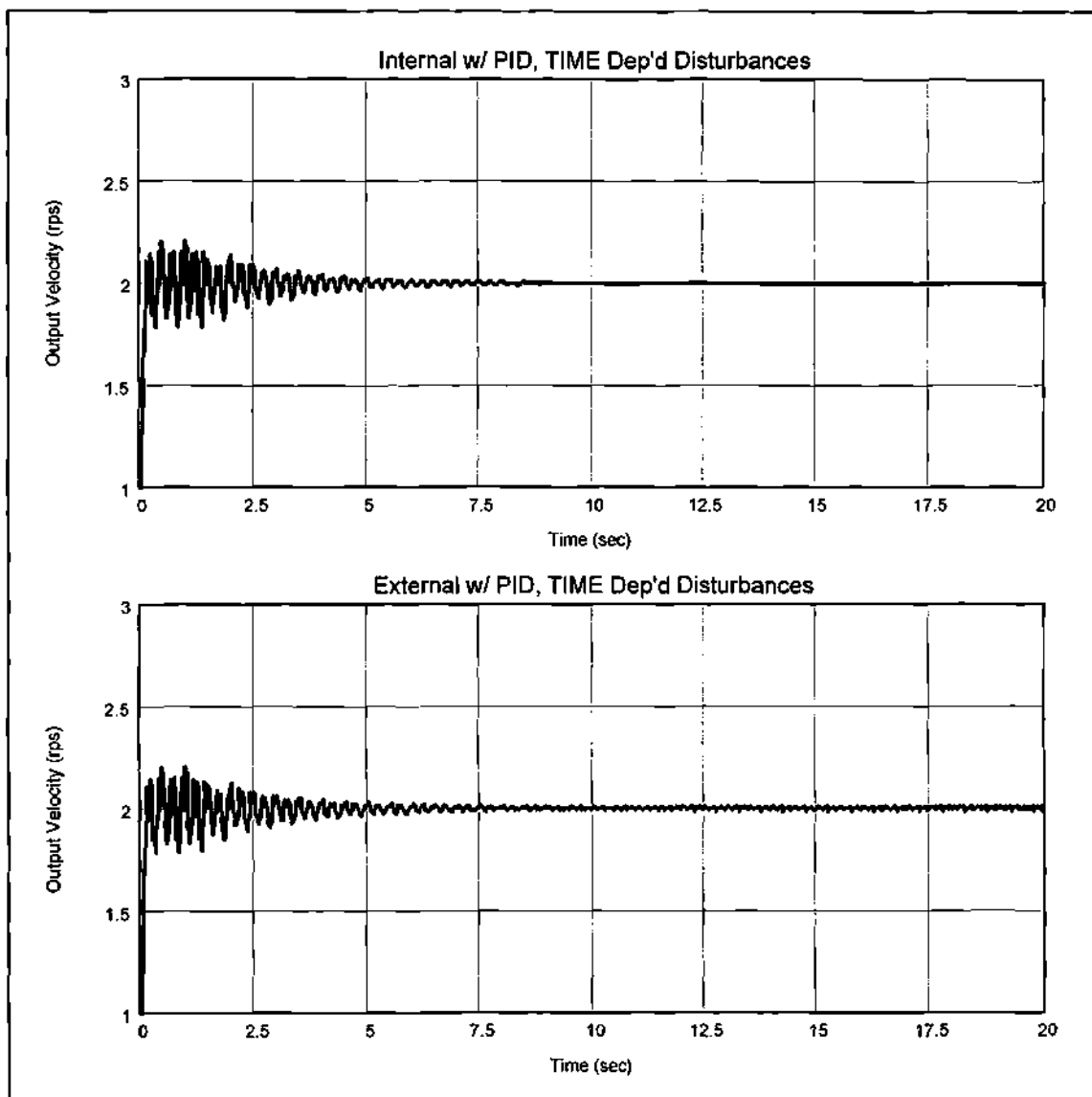
**B-1. RLC: Time Dependent Disturbances**

Figure 53 - Transient response, realistic disturbance amplitudes: Internal and external model RLC assuming periodic disturbances that are strictly functions of time. As in the case of polynomial control alone, both controller forms do a good job of attenuating the errors.

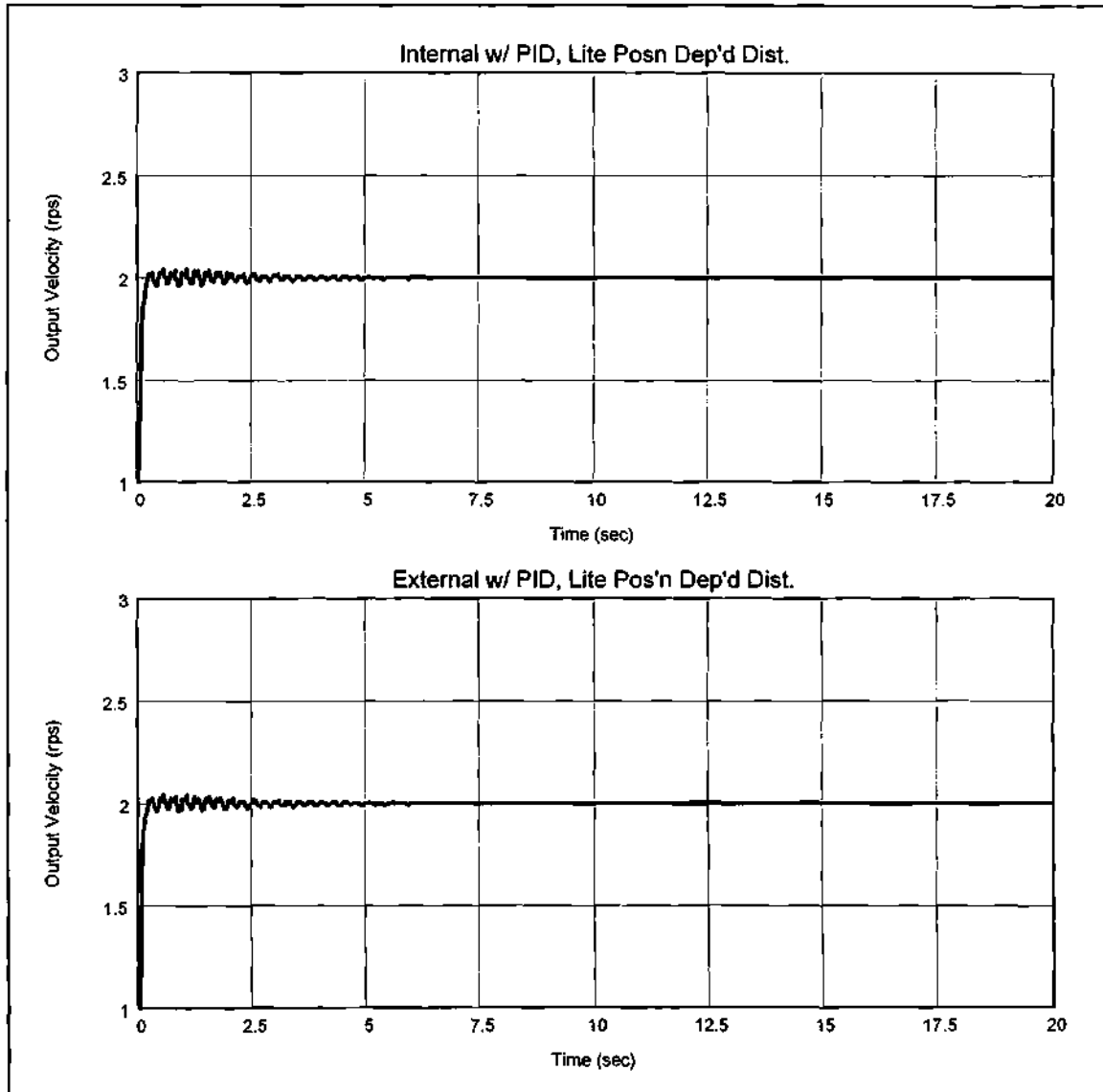
**B-2. RLC: Position Dependent Disturbances****a) Low-Amplitude Disturbances**

Figure 54 - Transient response, PCIA compensation, unrealistically low disturbance amplitudes (20% of realistic values): Internal and external model RLC assuming periodic disturbances that are functions of angular position.

## b) Realistic (High-Amplitude) Disturbances

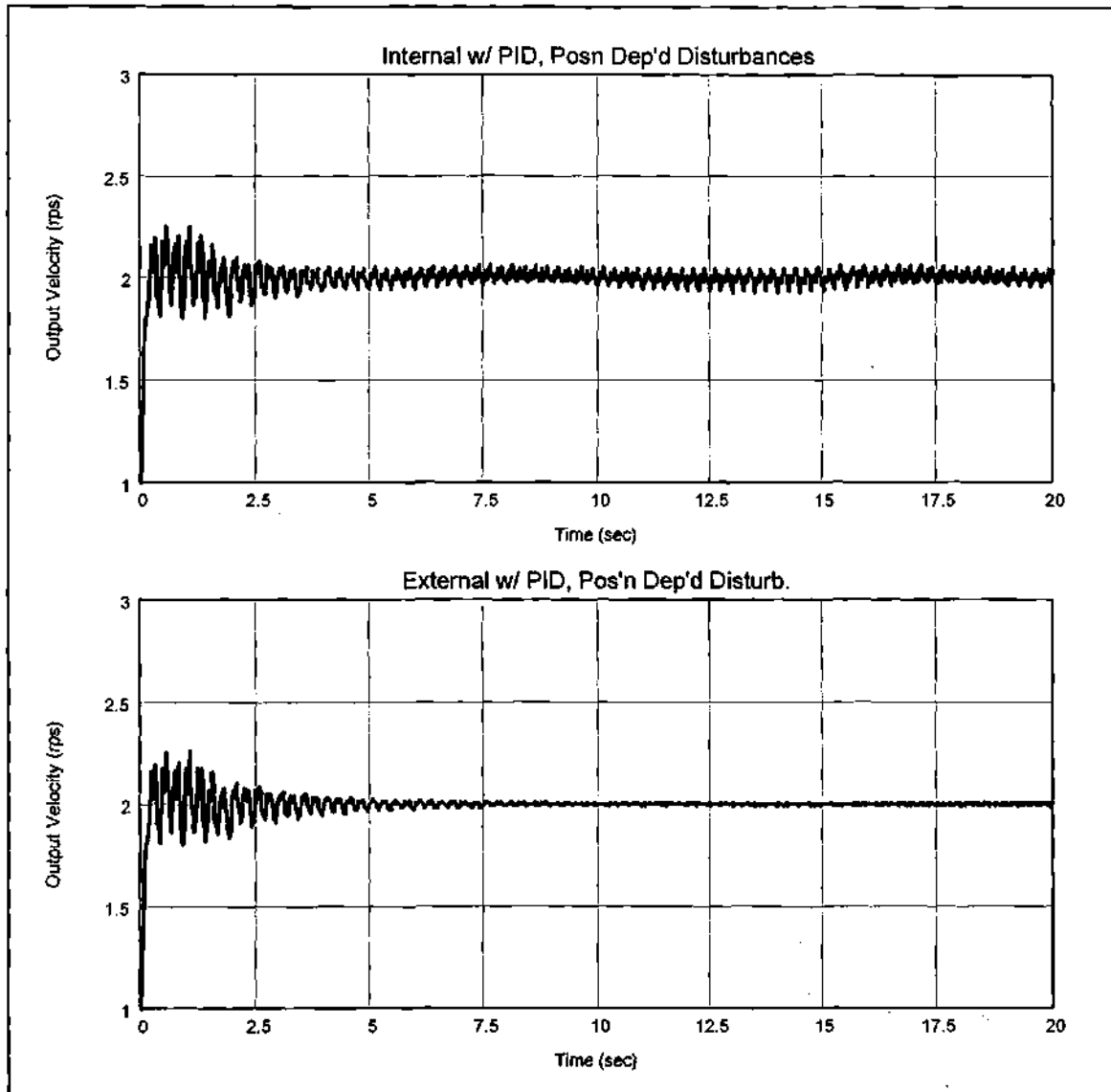


Figure 55 - Transient response, PCIA compensation, realistic disturbance amplitudes: Internal and external model RLC assuming periodic disturbances that are functions of angular position. The internal model controller fails to converge, as in the case of polynomial control without integral action. However, integrator does reduce the low frequency oscillations.

### Comments

For tests of the closed-loop plant without RLC, the simulation data indicate that the polynomial compensation with integral action (PCIA) provides a reduction in the error band over the compensation without integral action. This is expected since the integrator strengthens the controller's effectiveness in the DC and low frequency range (see Figure 40). The PCIA controller, however, has relatively high gains and is much less robust than the polynomial compensator. Such high gains would likely make the test fixture unstable if they were implemented empirically. Hence, the use of PCIA was confined to simulations.

Both the internal and external repetitive controllers provided good error attenuation in the presence of time-dependent disturbances. When the disturbances were state-dependent, the internal model controller only converged when the perturbation amplitudes were low (20% of realistic values). This clearly illustrates the existence of a disturbance amplitude threshold, above which convergence and stability are not guaranteed. The external controller performs more robustly and attenuates the errors for all test cases studied.

## Empirical Results

### A. Steady-State Response

#### A-1. Open-Loop Plant

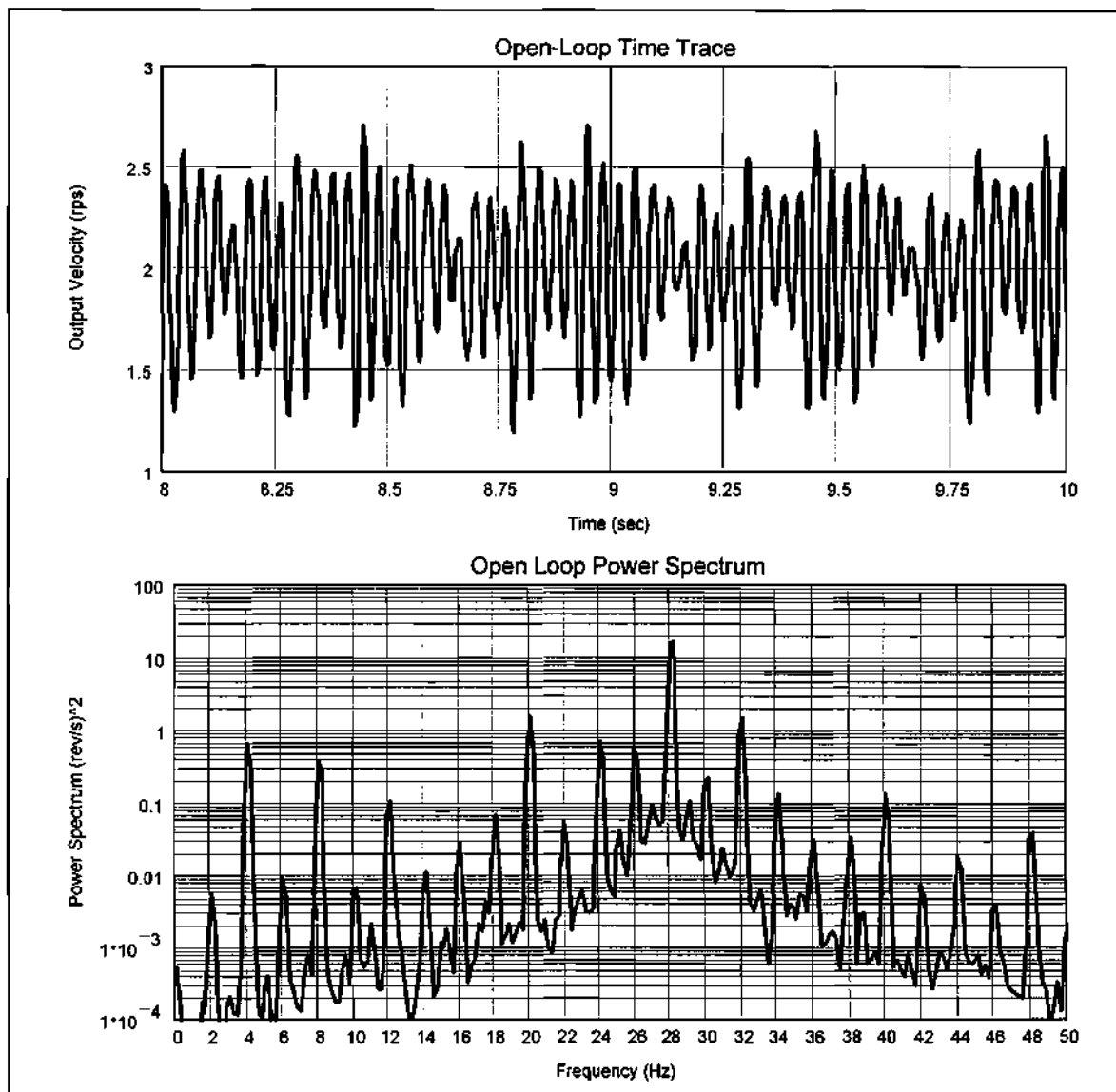


Figure 56 - Steady state time history and power spectral density for the open-loop system. Ten averages and a Hanning window were used in computing the FFT. Ref=2rps. The 0.5sec overall period is visually apparent in the time trace.

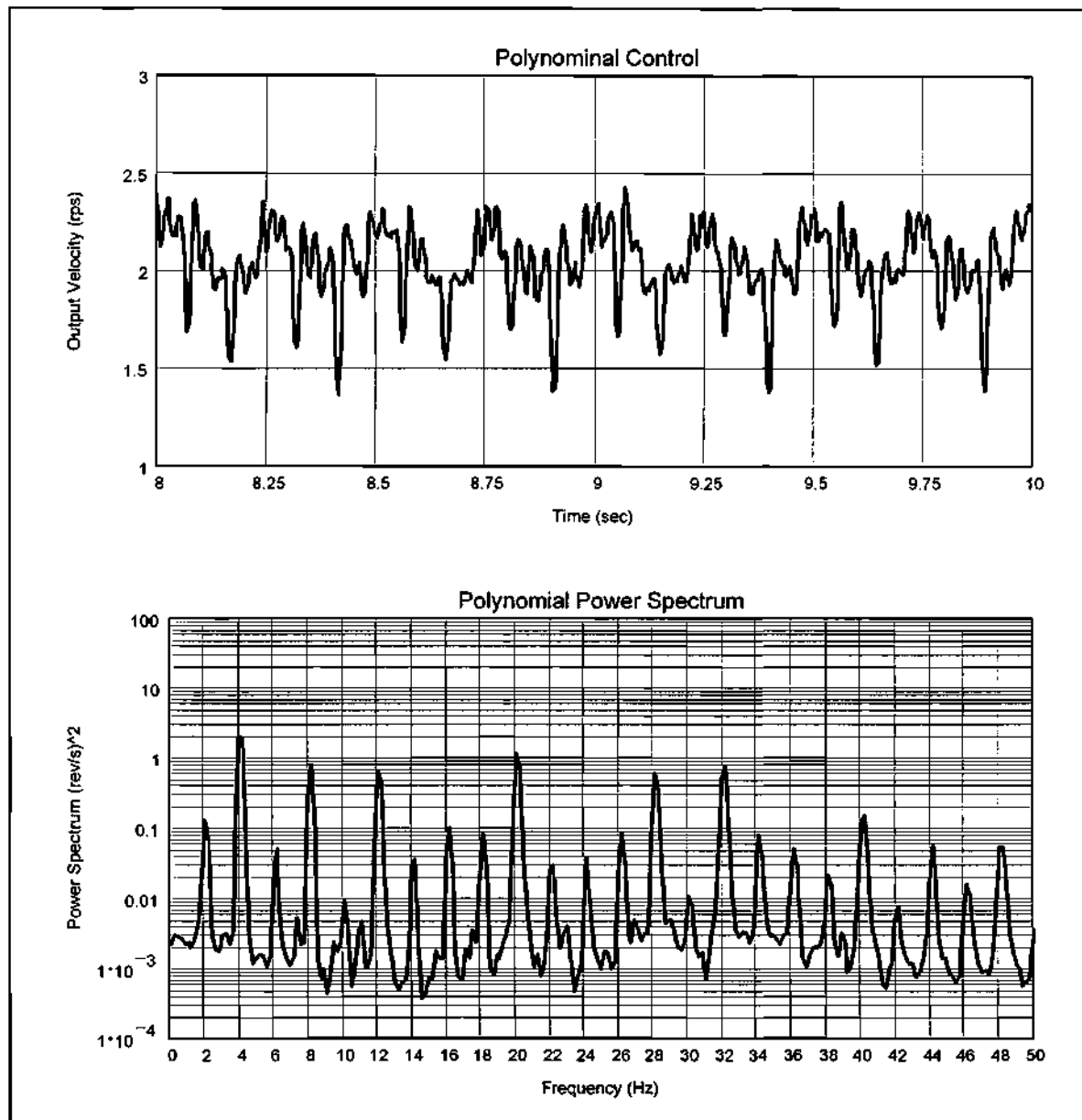
A-2. Closed-Loop Polynomial Control

Figure 57 - Steady state time history and power spectral density for the system under closed-loop polynomial control. There is a noticeable reduction in the amount of perturbation compared to the open-loop case.

### A-3. Frequency Spectrum Comparison

#### a) Open-Loop versus Polynomial Control

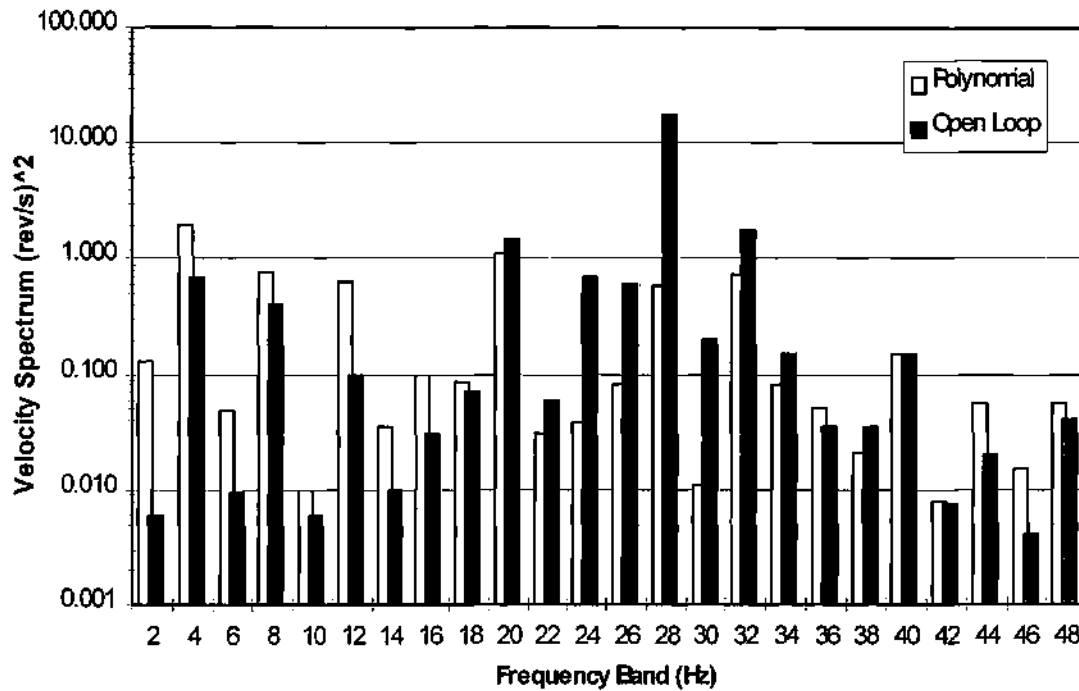


Figure 58 - Banded spectral density comparison: Polynomial Control versus Open Loop. Note that polynomial control provides (by design) a significant amount of attenuation in the region surrounding the open-loop's 28 Hz resonance, while adding a relatively small amount of amplification at the lower frequencies. The performance of the polynomial controller would be greatly improved (especially in the lower frequencies) if integral action were present. However, as mentioned previously, integral action was only implemented in simulation.

## b) Polynomial Control versus Internal Model RLC

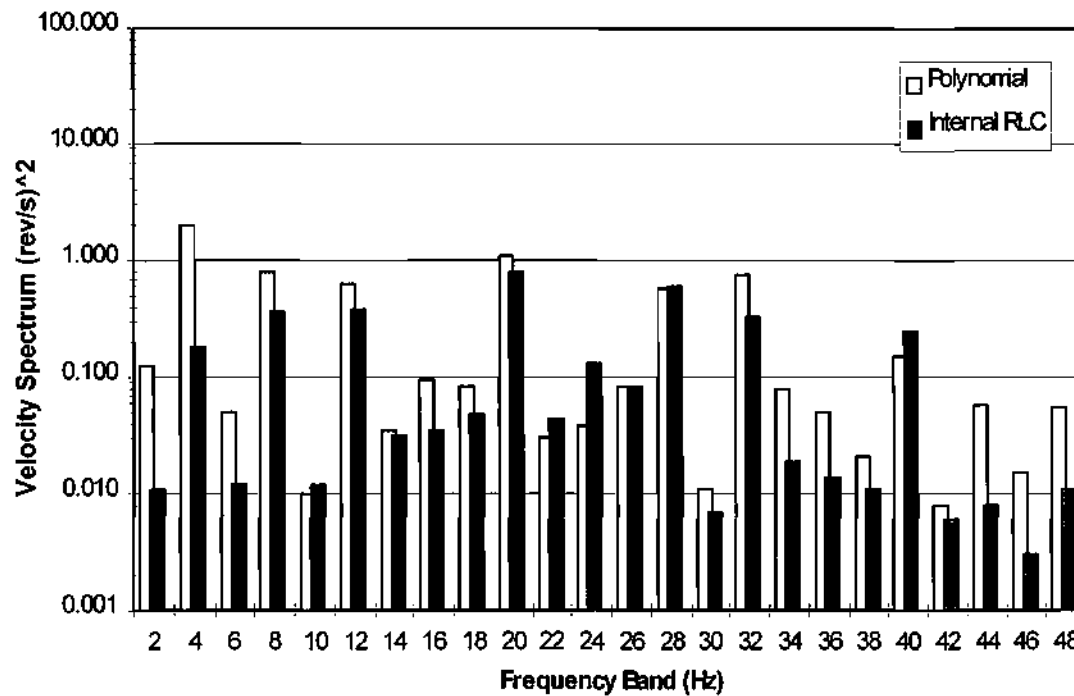


Figure 59 - Banded spectral density comparison: Polynomial Control versus Internal Model RLC. The repetitive controller provides superior attenuation at virtually all harmonic frequencies, with notable exceptions at 24 and 40 Hz. In fact, the attenuation improvement at the first and second harmonics (i.e., 2 and 4 Hz) is better than a factor of ten. This is due to both the repetitive control action and the mild integral action inherent in RLC.

## c) Internal, External, and Hybrid RLC

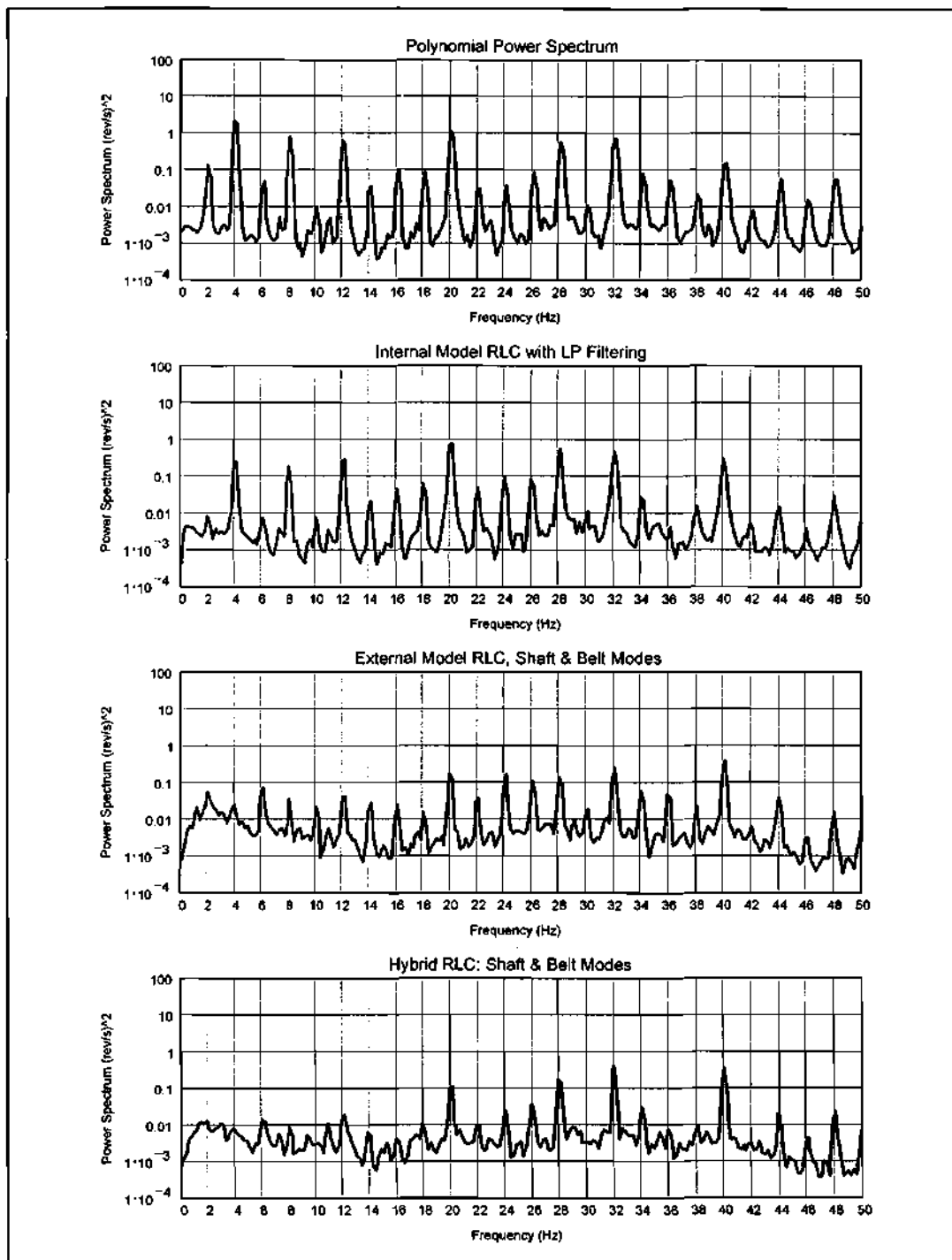


Figure 60 - Repetitive controller frequency spectrum comparison.

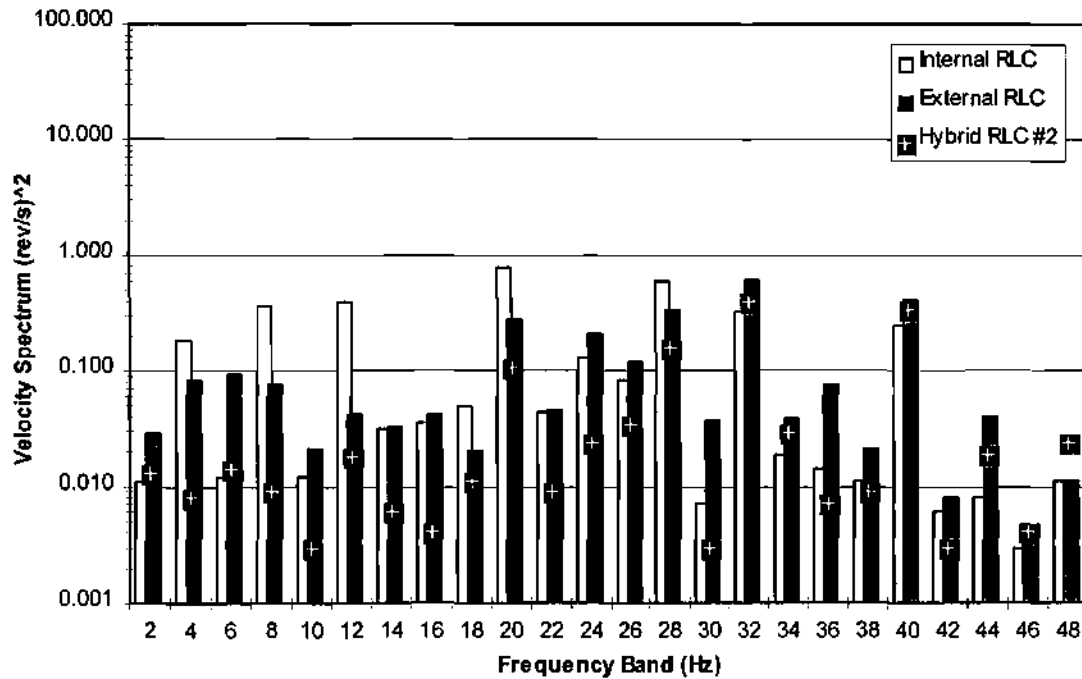


Figure 61 - Banded spectral density comparison: Internal and External Model RLC versus Hybrid RLC. The hybrid repetitive controller provides superior overall disturbance attenuation compared to both the internal and external model controllers. At some shaft harmonics (e.g., 4 & 20 Hz), the improvement in attenuation is on the order of 90%. The external model controllers were set to attenuate modes at 2, 4, 8, 12, 18, 20, 32, & 40 Hz.

#### A-4. Steady-State Output Comparison: Velocity vs. Time

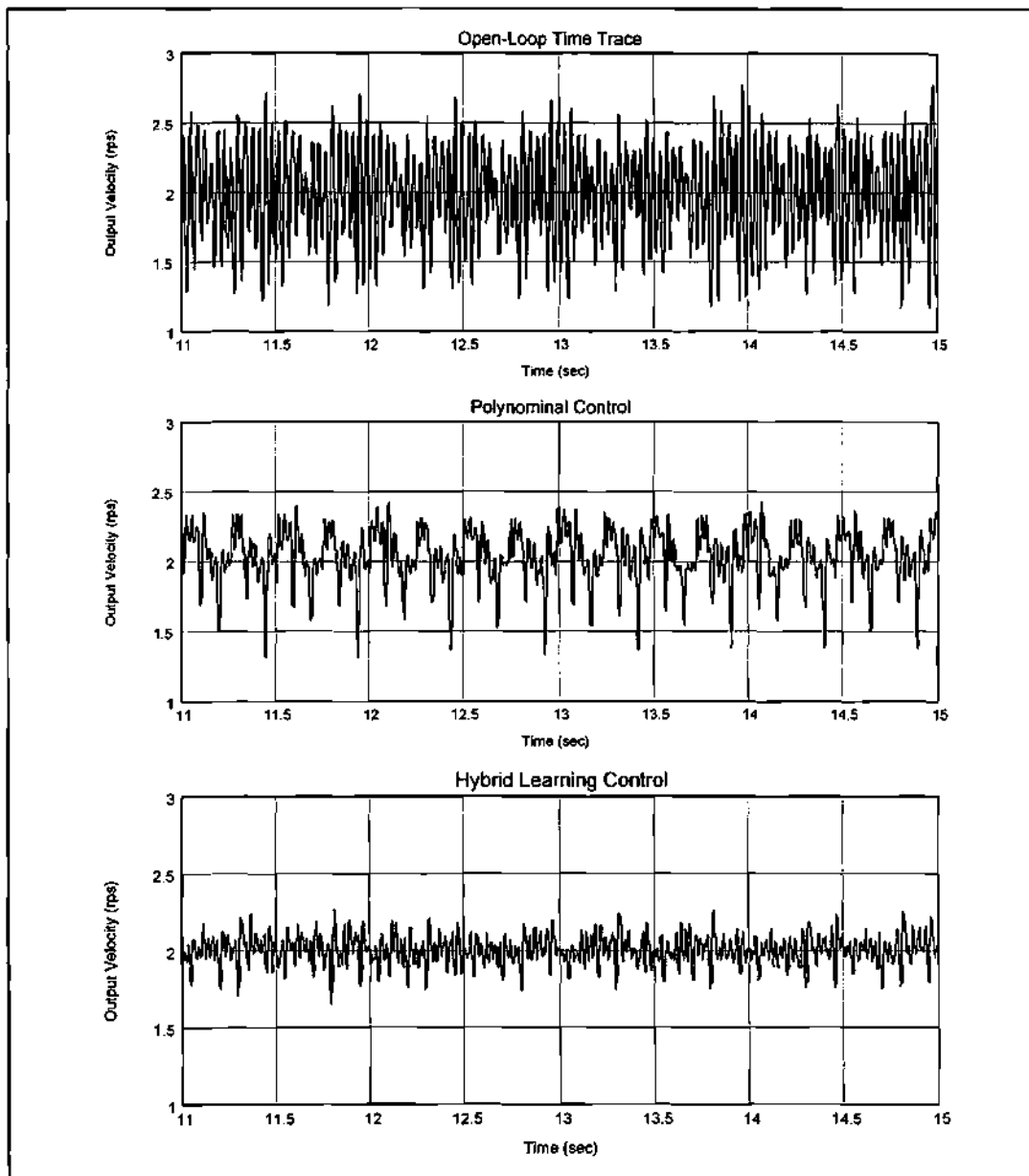


Figure 62 - 4-second steady-state response of the open loop system, the closed loop system with polynomial feedback, and the closed loop system with hybrid (i.e., internal and external model) repetitive learning control, respectively.

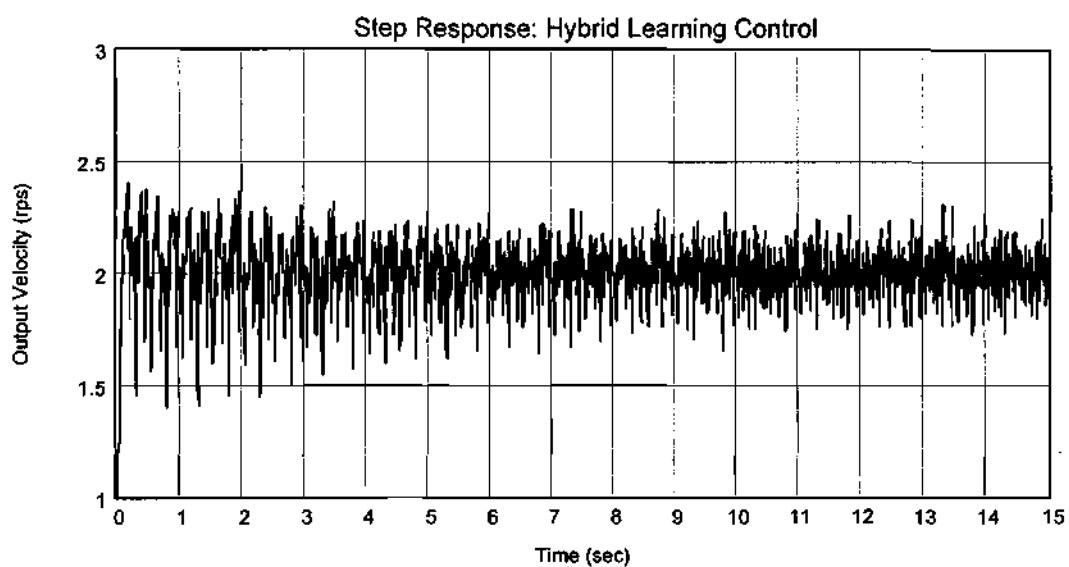
**B. Transient Response: Hybrid RLC****STEP RESPONSE**

Figure 63 - Step response of closed loop system with hybrid (i.e., internal and external model) repetitive learning control. Learning gain is 0.2. RLC was activated 0.5 seconds after startup.

### Comments

The empirical tests served to verify both the simulation results and the theoretical predictions. The design of the system (see Chapter V) made it difficult to achieve stellar error attenuation. By having only one input and one output separated by numerous reductions, compliances, and noise sources, the ability of any controller to attenuate all of the errors is significantly challenged. For example, in the case of the adaptive external model controller, the disturbances - which in reality are functions of the output position of various shafts - are assumed to be functions of the measured shaft position. This would be valid if the system were rigid since the gear ratios between the various shafts are known. However, because of the significant compliance present, it is difficult to accurately infer the instantaneous position of one shaft by measuring the position of another. Nonetheless, compared to open loop or polynomial control alone, the repetitive controllers provided a significant improvement in steady-state performance of the system. In particular, the hybrid controller provided superior error attenuation over the single internal and external model repetitive control configurations (see Figure 60).

## CHAPTER VIII

### CONCLUSIONS AND RECOMMENDATIONS

Based on the preceding analyses and results, the following conclusions are made regarding repetitive learning control and its application to systems with periodic tasks and/ or disturbances:

- The ability of repetitive control to attenuate tracking errors in a system with periodic disturbances is governed by numerous factors which include:
  - a) the type(s) of harmonic and non-harmonic disturbances present and the magnitude of these disturbances;
  - b) the sampling rate of both the plant and the repetitive controller;
  - c) the learning gain(s) applied to the feedback error signal;
  - d) the Q-filter used (if any) to cancel the phase lag of the plant;
  - e) how closely the implemented learning cycle (NL) matches the actual length cycle; and
  - f) the type of closed-loop compensation, if any, applied to the raw plant in addition to repetitive control.
- The two classes of repetitive controllers are internal model based and external model based
- Internal model controllers are computationally simple and work best when the task and disturbances are periodic and strict functions of time. Conversely, external model controllers are computationally intensive, but are able to track and

adapt to disturbances that vary slightly as a function of some system state. External model based controllers also allow frequency selectivity.

- The disturbances present in a plant can be a combination of time dependent and state dependent perturbations. The actual nature of these disturbances determines whether internal model based or external model based repetitive control is best suited to attenuate the errors.
- The component of an error signal corresponding to non-harmonic noise and/ or disturbances will be amplified in the presence of stable repetitive learning control. It has been shown that there is no region of the complex solution space in which stable repetitive control operation and non-harmonic error attenuation coexist. However the amplification may be minor and, assuming the amplitude of these errors is relatively small, the benefit of RLC will usually outweigh the disadvantage of slightly larger non-harmonic errors.
- Although RLC can be shown to theoretically drive periodic errors to zero regardless of their amplitude, practical limitations exist. Besides any bandwidth limitations associated with the hardware and actuators, it has been proven that the allowable amplitude of those periodic system disturbances that are not strict functions of time is bounded. The guarantee of exponential stability will no longer apply if the disturbances exceed this bound.
- The repetitive controller's robustness to noise and unmodeled dynamics can be improved with the addition of a low-pass zero-phase filter. Naturally, the ability of the controller to attenuate harmonic errors above the filter's cutoff frequency will be reduced as well. However, since the significant disturbance content for many systems is at relatively low frequencies, this loss of attenuation ability is usually tolerable.
- For systems with disparate disturbance frequencies, the learning cycle length (NL) of a single repetitive controller may be inhibitive large. Combining two

or more stable repetitive controllers in parallel and adjusting their gains to maintain stability is a viable solution to this problem.

- When the periodic disturbances present in a system are a mixture of time dependent and state-dependent perturbations, the concept of parallel controllers can be extended to include both an external model and an internal model repetitive controller, thus forming a hybrid repetitive controller.
- Hybrid repetitive control was shown to give the best disturbance rejection of all controllers implemented on the experimental test fixture. This is probably due to the presence of both time and state-dependent disturbances in this system.
- The stability criteria developed for a single-rate system with repetitive control can be extended to a dual / multi-rate system by transforming the fast sampling plant to a slow-rate equivalent subject to up-sampling and / or down-sampling input and output interfaces. The transformed plant then forms a single-rate system with the repetitive controller and the single-rate stability criteria can be applied.
- Disturbance rejection by repetitive learning control would be improved by:
  - Increasing the number of output sensors. Then, a more aggressive closed-loop controller could be designed and implemented; this would reduce the burden on the repetitive controller. In particular, if stable integral action is implemented (as assumed in the state-dependent disturbance stability assessment - see Chapter II), then the stability and performance of a repetitive controller will be assured for disturbances with amplitudes below some threshold.
  - Designing or modifying the plant so that the amplitudes of the disturbances were lower. In this manner, the aforementioned disturbance magnitude threshold could be avoided.

APPENDIX A  
TEST FIXTURE COMPONENTS

Table 3 - Summary of test fixture components

Item	Comments
Drive Motor	Leeson, 1/15 hp, permanent magnet, brush commutated DC motor. Subsystem #1; Max voltage: 90V, max torque: 230 in-oz, max current: 11.6A.
Timing Belts	Nylon corded neoprene; 1/5"pitch; 3/8" wide.
Pulleys	Nylon, glass filled; 1/5" pitch; three sizes used: 10, 20, and 30 tooth.
Steel Shafts	Subsystems #2 & #4; 1/4" OD tool steel.
Flex-Shaft	Delrin; 1/4" OD, 8" length between bearings.
Shaft Couplings	Subsystem #4; Bellows between brake and cam shaft, Renbrandt between brake and encoder.
Primary Material	3/8" Aluminum
Brake	Subsystem #4; Magtrol HB-32-2 hysteresis brake;
Encoder	1000 pulse/rev Dynapar optical encoder.
Frequency to Voltage Convertor	Analog Devices F-V
Power Amplifier	Kepco ATE 100-1M
Data Acquisition Card	National Instruments (NI) AT-MIO-16-X multi-function board; 2 analog outputs, 8 analog inputs, 8 digital I/O channels, counter timer chip.
Computer Platform	Dell 133MHz Pentium, 32MB RAM.
Interface Software	NI LabWindows/ CVI C-code programming environment.
Analysis Software	Matlab 5, Simulink, MathCAD 6.
Computer Aided Design	Cadkey 7 Mechanical Design Software

**APPENDIX B****PERIODIC SIGNAL GENERATION LEMMA**

Periodic Signal Generation Lemma

Consider the minimal state-space realization  $(A,B,C,D)$ . Let the periodic signal  $d(k)$  be such that the poles of its  $z$ -transform  $Z[d(k)]$  are a subset of the eigenvalues of matrix  $A$ . Then there exists an initial state vector  $x_0 \in \mathfrak{R}^n$  such that

$$\begin{aligned} x(k+1) &= A \cdot x(k) \\ d(k) &= C \cdot x(k) \end{aligned} \quad (95)$$

That is, the signal  $d(k)$  is generated (or evolved) from  $(A,B,C,D)$  with zero input and initial condition  $x = x_0$  for  $k \geq 1$ .

Proof

Since  $d(k)$  is a subset of the full system, we have  $|z \cdot I - A| \equiv D(z) \cdot E(z)$ . Let the  $z$ -transform of  $d$  be given by  $Z[d(k)] = \frac{N(z)}{D(z)}$ . Then

$$Z[d(k)] = \frac{N(z) \cdot E(z)}{D(z) \cdot E(z)} \Rightarrow G(z) \quad (96)$$

Let  $(\hat{A}, \hat{B}, \hat{C}, \hat{D})$  be the observable state-space representation of  $G(z)$ ; that is:

$$\hat{A} \equiv \begin{bmatrix} -a_1 & 1 & 0 & 0 \\ -a_2 & 0 & \ddots & 0 \\ \vdots & \vdots & \ddots & 1 \\ -a_n & 0 & \cdots & 0 \end{bmatrix}, \quad \hat{B} \equiv \begin{bmatrix} * \\ * \\ * \\ * \end{bmatrix}, \quad \hat{C} \equiv [1 \quad 0 \quad \cdots \quad 0]$$

Then

$$d(k) = \begin{cases} d(0), & \text{if } k = 0 \\ \hat{C} \cdot \hat{A}^{k-1} \cdot \hat{B}, & \text{otherwise} \end{cases} \quad (97)$$

If  $T$  is the transformation matrix that maps  $(A, C)$  to  $(\hat{A}, \hat{C})$ , then

$$\hat{x} = T \cdot x, \quad \hat{C} = C \cdot T^{-1}, \quad \hat{A} = T \cdot A \cdot T^{-1}, \quad \hat{A}^{k-1} = T \cdot A^{k-1} \cdot T^{-1}$$

Using these relationships, the value of  $d(k)$  for  $k > 0$  in equation (97) becomes

$$d(k) = \hat{C} \cdot \hat{A}^{k-1} \cdot \hat{B} \Rightarrow C \cdot A^{k-1} \cdot (T^{-1} \cdot \hat{B}) \quad (98)$$

Defining the initial state / condition assumed in (95) as  $x_0 \equiv T^{-1} \cdot \hat{B}$ , then signal  $d(k)$  in equation (97) becomes

$$d(k) = \begin{cases} d(0), & \text{if } k = 0 \\ C \cdot A^{k-1} \cdot x_0, & \text{otherwise} \end{cases} \quad (99)$$

Therefore,  $d(k)$  is the output of system  $(A, B, C, D)$  with zero input and initial state  $x = x_0 \equiv T^{-1} \cdot \hat{B}$ .

## REFERENCES

- [1] Alter, D.M., et. al., *Two-dimensional exact model matching with application to repetitive control*, ASME J. Dynamic Syst. Meas. Contr, vol.116 #1, pp. 2-9, 1994
- [2] Broberg, H., et. al., *A new approach to phase cancellation in repetitive control*, IEEE Proceedings, 1994
- [3] Chew, K., et. al., *Steady-state stochastic performance of a modified discrete-time prototype repetitive controller*, ASME J. Dynamic Syst., Meas., & Control, vol. 112, pp.35-41, March, 1990
- [4] Cosner, C., et. al., *Plug-in repetitive control for industrial robotic manipulators*, IEEE Int. Conf. on Robotics & Auto., 1990
- [5] Curtelin, G., et. al., *Repetitive control of continuous systems: comparative study and application*, IEEE SMC 93, vol.5, October, 1993
- [6] Curtelin, G., et. al., *Analysis of repetitive control system robustness*, IEEE Proceedings, 1994
- [7] Dotsch, H., et. al., *Adaptive repetitive control of a compact disc mechanism*, IEEE Proceedings, 1995
- [8] Hillerstrom, G., et. al., *Repetitive control using low order models*, Proc. Amer. Contr. Confr, pp.1873, June, 1994
- [9] Hillerstrom, G., et. al., *Rejection of periodic disturbances with unknown period - a frequency domain approach*, Proc. Amer. Contr. Confr., pp.1626, June, 1994
- [10] Hillerstrom, G., *Adaptive suppression of vibrations - A repetitive control approach*, IEEE Proceedings, 1996
- [11] Hu, J., et. al., *Adaptive asymptotic tracking of repetitive signals*, Proc. Amer. Contr. Conf, vol.3, 1991
- [12] Inoue, T., *Practical repetitive control system design*, Proc: 29th IEEE Conf on Decision & Contr., pp.1673-1678, vol.3, 1990
- [13] Jiang, Y.A., et. al., *Adaptive repetitive control of nonlinear systems*, IEEE Proceedings, Dec., 1995
- [14] Jolly, T., et. al., *Rejection of unknown periodic load disturbances in continuous steel casting process using learning repetitive control approach*, IEEE Proceedings, 1993
- [16] Kobayashi, F., et. al., *Reduction of motor speed fluctuation using repetitive control*, Proc: 29th IEEE Conf Dec & Contr, 1990

- [17] Ledwich, G.F., et. al., *Repetitive and periodic controller design*, IEE Proc -E, vol.140 #1, 1993
- [18] Liu, K-Z, et. al., *On robust steady-state performance of feedback control systems*, IEEE Proceedings, 1992
- [19] Medvedev, A., et. al., *On perfect disturbance rejection*, Proc. 32nd Conf. Decision Contr, pp.1324, Dec., 1993
- [20] Messner, W., et. al., *A new adaptive learning rule*, IEEE Trans. Automatic Contr, vol.36, pp.188, 1991
- [21] Sadegh, N., *Synthesis and stability analysis of repetitive control systems*, Proceedings of the Amer. Contr.Conf, pp.2634-2639, 1991
- [22] Sadegh, N., *Synthesis of a stable discrete-time repetitive controller for MIMO systems*, ASME Journ. of Dyn Sys, Meas. & Control, vol.117, 1993
- [23] Sadegh, N., et. al., *Design and Implementation of Adaptive and Repetitive Controllers for Mechanical Manipulators*, IEEE Transactions, vol.8 # 3, 1992
- [24] Sadegh, N., et. al., *A unified approach to the design of adaptive repetitive controllers for robotic manipulators*, ASME Jour of Dyn Sys Meas. & Contr, vol.112, pp.618, 1990
- [25] Shaw, F.R., et. al., *Analysis and design of repetitive control systems using the regeneration spectrum*, Transactions of ASME, vol.133, June, 1991
- [26] Tomizuka, M., et. al., *Zero-phase error tracking algorithm for digital control*, ASME Journ. of Dyn Sys, Meas. & Control, vol.109, Mar., 1987
- [27] Tomizuka, M., et. al., *Disturbance rejection through an external model*, ASME J. Dynamic Syst., Meas., & Control, vol.112, pp.559-564, Dec., 1990
- [28] Tsao, T.C., et. al., *Asymptotic rejection of periodic disturbances with uncertain period*, Proc. Amer. Contr. Conf., pp.1736, 1992
- [29] Tsao, T.C., et. al., *An adaptive repetitive control scheme for tracking periodic signals with unknown period*, Proc. Amer. Contr. Conf, pp.1736-1740, 1993